COMPUTATIONAL ANALYSIS OF CYCLOOXYGENASE INHIBITION: ENERGETICS AND DYNAMICS

By

Christopher Williams Moth

Dissertation

Submitted to the Faculty of the

Graduate School of Vanderbilt University

in partial fulfillment of the requirements

for the degree of

DOCTOR OF PHILOSOPHY

in

Chemistry

May, 2008

Nashville, Tennessee

Approved:

Professor Terry P. Lybrand

Professor Lawrence J. Marnett

Professor Michael R. Waterman

Professor Ned A. Porter

Professor Alan R. Brash

DEDICATION

To my father, Brian, who wished he could have been a chemist.

To my wife, Valerie, for encouraging me to pursue my dreams.

ACKNOWLEDGEMENTS

There are no adequate words to convey my sincerest thanks to Dr. Terry Lybrand for inviting me into in his lab, and to Dr. Larry Marnett for allowing me to attend his experimental lab meetings. I deeply appreciate the guidance and patience of my committee, as I navigated the murky waters of biomolecular simulation.

The interdisciplinary atmosphere at Vanderbilt has provided a wonderful backdrop for all of my studies. Thanks to Al Beth and the Chemical and Physical Biology (CPB) program for funding a flexible starting point for my Ph.D. Studies. I have enjoyed financial support from the National Institute of Health through Chemistry Biology Interface training grant T32 GM65086-02 and N.I.H. Research grants NS33290 (Lybrand) and CA89450 (Marnett). And, thanks to the Vanderbilt Dept. of Chemistry for allowing me to T.A. and grade courses in order to fund the most recent years of my graduate studies.

We are incredibly fortunate at the Structural Biology Center to have excellent computing resources, and support infrastructure. Special thanks to Jarrod Smith, Brandon Valentine, Roy Hoffman, Sabuj Pattanayek, and Holland Griffis for all their help keeping our software current, and our hardware working well. Thanks also to Joel Harp for his tireless assistance with my X-ray crystallography questions.

For the work in chapter IV, I thank Professor Mihaly Mezei of Mount Sinai School of Medicine for providing his Grand Canonical Monte Carlo code. This work was also made possible, in part, with resources from the Advanced Computing Center for Research and Education at Vanderbilt University.

Very little of this dissertation would have been completed without the ground-breaking cyclooxygenase simulation work performed by Kristina Furse. Kristina developed the fundamental protocols for simulating the full Cyclooxygenase dimer in a solvated truncated octahedron, the channel_finder utility employed in chapters III and IV, and the steric shielding analysis scripts of chapter IV.

TABLE OF CONTENTS

LIST OF FIGURES

LIST OF SCHEMES

LIST OF TABLES

CHAPTER I

INTRODUCTION

Cyclooxygenase

The 70 kDa cyclooxygenase (COX) enzyme provides a fascinating and industrially relevant point of focus for the computational studies described in this dissertation. Described most simply, COX functions as a membrane-associated homodimer, catalyzing the committed step in the conversion of arachidonic acid (AA) to prostaglandin H_2 (PGH_2), following AA's release from membrane phospholipds. An overview of this reaction is depicted in scheme I-1 below:

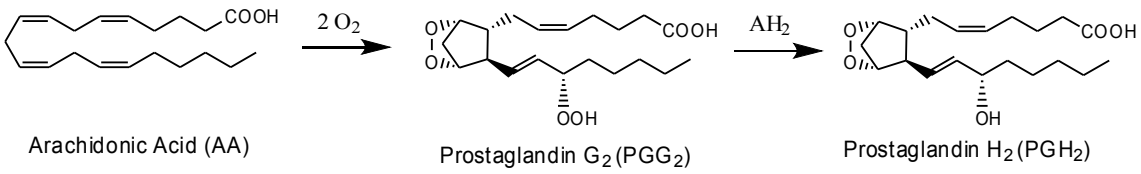

Scheme I-1. COX synthesizes prostaglandin G_2 (PGG_2) from arachidonic acid at the cyclooxygenase active site. PGH_2 is reduced to prostaglandin H_2 (PGH_2) at the enzyme's peroxidase site.

COX is a binfunctional enzyme with two active sites. At the cyclooxygenase active site, COX exquisitely controls the regio and stereo-selective *bis*-dioxygenation and cyclization of AA to form PGG_2. The reaction concludes at the entirely distinct peroxidase site, where intermediate PGG_2's C15 hydroperoxide is reduced to an alcohol to form PGH_2. The genome codes two 60% sequence-identical isoforms of COX. Both COX-1 and COX-2 catalyze the same reaction, and the discussion which follows applies

to both. COX-2 will be introduced in much greater detail later. Figure I-1 below introduces the three-dimensional structure of COX.

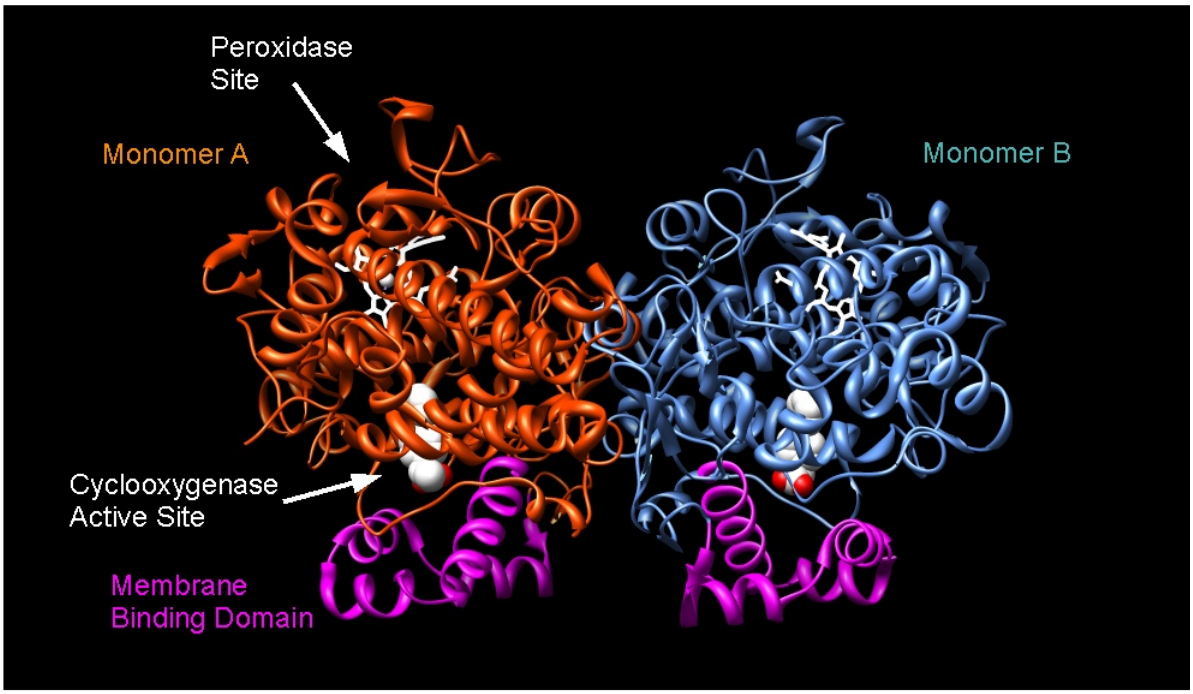

Figure I-1. The three-dimensional structure of the COX homodimer assembly (1Q4G.pdb) The COX globular domains are shown as brown and blue ribbons. The four membrane-binding helices are shown in Magenta. The competitive inhibitor α-methyl-4-biphenyl acetic acid is bound in the cyclooxygenase active site, and rendered in CPK. Heme prosthetic groups at the peroxidase sites are shown in white sticks.

The COX reaction product PGH_2 is unstable (Hamberg and Samuelsson 1973; Andersen and Hartzell 1984) and its bioactivity is imparted downstream by tissue-specific synthases which swiftly convert PGH_2 to other bioactive prostaglandins, as shown in Figure I-2 below. These prostaglandins, in turn, bind to G-protein-coupled receptors and effect diverse biological responses (Funk 2001).

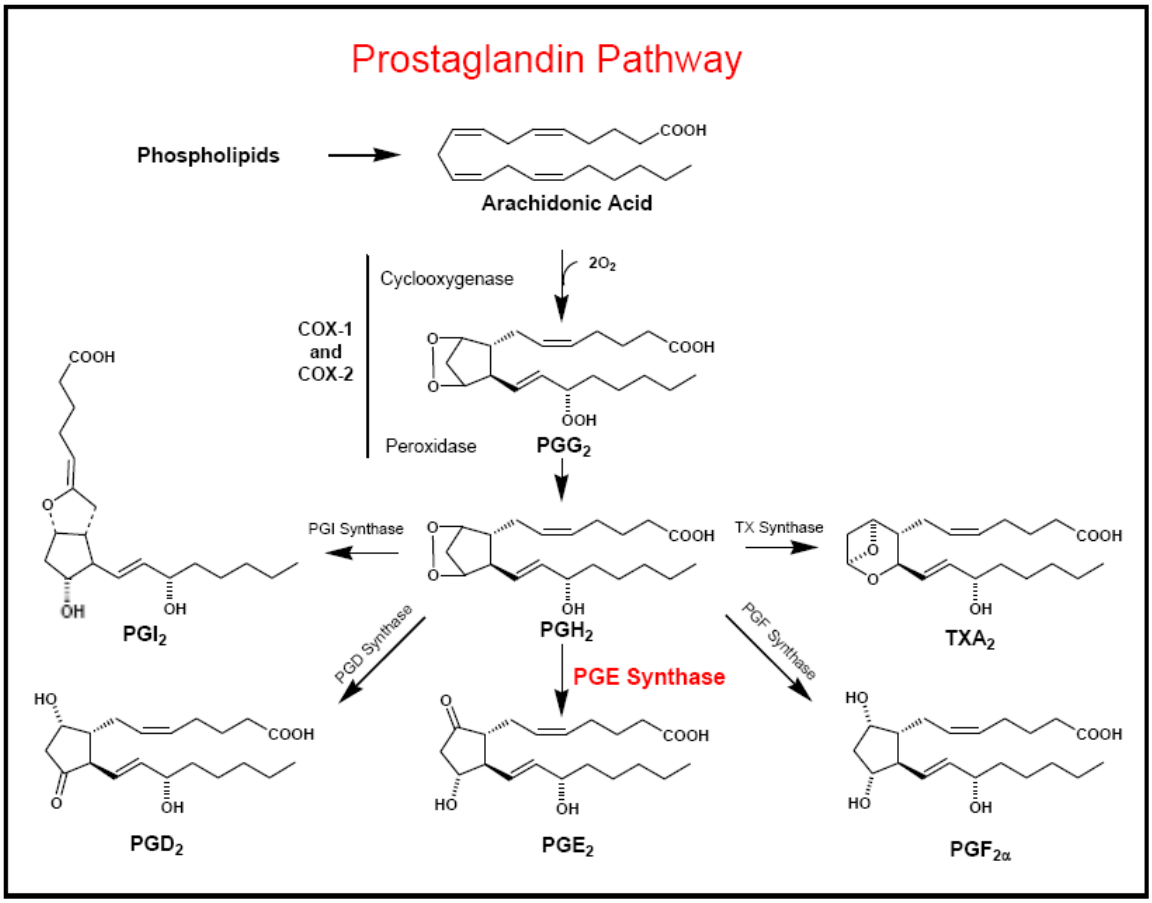

Figure I-2. Major prostaglandins produced from PGH_2
Figure used with permission of Hélène Juteau, Merck Frosst, Kirkland Quebec.

COX inhibitors (Aspirin being most famous) are therapeutically useful as anti-inflammatory, analgesic, anti-pyretic, and anti-coagulant agents. As a group, these inhibitors are commonly known as non-steroidal anti-inflammatory drugs (NSAIDs). The physiological impacts of NSAIDs result from the drop in downstream prostaglandin concentrations which follows COX inhibition. To understand how COX inhibitors bind to the enzyme active site, it is helpful to review both the reactions catalyzed by cyclooxygenase, and the features that nature has evolved in the cyclooxygenase active site to bind arachidonic acid and tightly control its conversion to PGG_2.

Mechanism

Arachidonic acid (5,8,11,14-eicosatetranenoic acid or AA) has three *bis*-allylic methlyene carbons (C7, C10, and C13 are located between the *cis* double bonds). These carbons are readily oxidized non-enzymatically, as abstraction of a hydrogen atom at any of these positions yields a planar pentadienyl radical. In solution, O_2 molecules can add to either face of this radical, at the first, third, or fifth carbon which bear the unpaired electron spin density. Moreover, oxygen additions at the first or fifth carbon result in a final conjugated product which can be configured Z,E or E,E (Porter et al. 1980; Porter 1986). Thus, for each of the three *bis*-allylic methlyene carbons in arachidonic acid, an initial oxygenation can yield any one of 10 possible hydroperoxide products. Oxygenation is only one possible fate for pentadienyl radicals, which can also propagate through intramolecular abstraction of other labile hydrogens, forming rings. Alternately, pentadienyl radicals can be quenched upon reaction with non-oxygen radical traps (Rouzer and Marnett 2003).

In contrast to these combinatorially diverse AA radical reaction products in solution, the enzymatic *bis*-dioxygenation and cyclization of AA at the cyclooxygenase active site is strikingly specific, yielding (nearly) exclusively PGG_2. Impressively, key details of the cyclooxygenase reaction were unveiled by Samuelsson's radio-labeling experiments in the 1960s – long before the enzyme's isolation from tissue homogenates (Samuelsson 1965). In part because of this work, he shared the 1982 Nobel Prize in Medicine. Our current understanding of the mechanism is shown in Scheme I-2 below. In the following section, the mechanism will be discussed in greater detail, in the context of COX active site structural features.

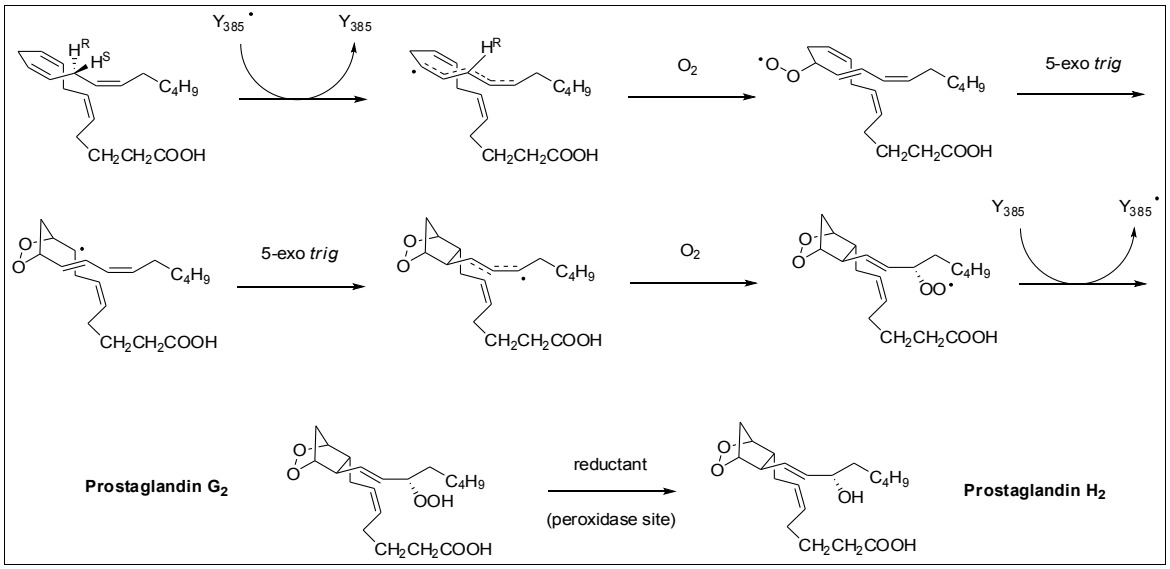

Scheme I-2. PGG_2 is synthesized at the cyclooxygenase site through a free radical mechanism, in which two molecules of oxygen are added to arachidonic acid. The final product, PGH_2 is the result of a reduction at the distinct peroxidase site.

Active Site

A tour of the enzyme active site aids a rationalization of the COX reaction mechanism. As suggested by scheme I-2, the first requirement for catalysis is a long, hydrophobic cavity to bind and anchor arachidonic acid in a bent conformation (Marnett and Maddipati 1991). This cavity is provided by the globular domain of COX and it is shown as a translucent surface in Figure I-3.

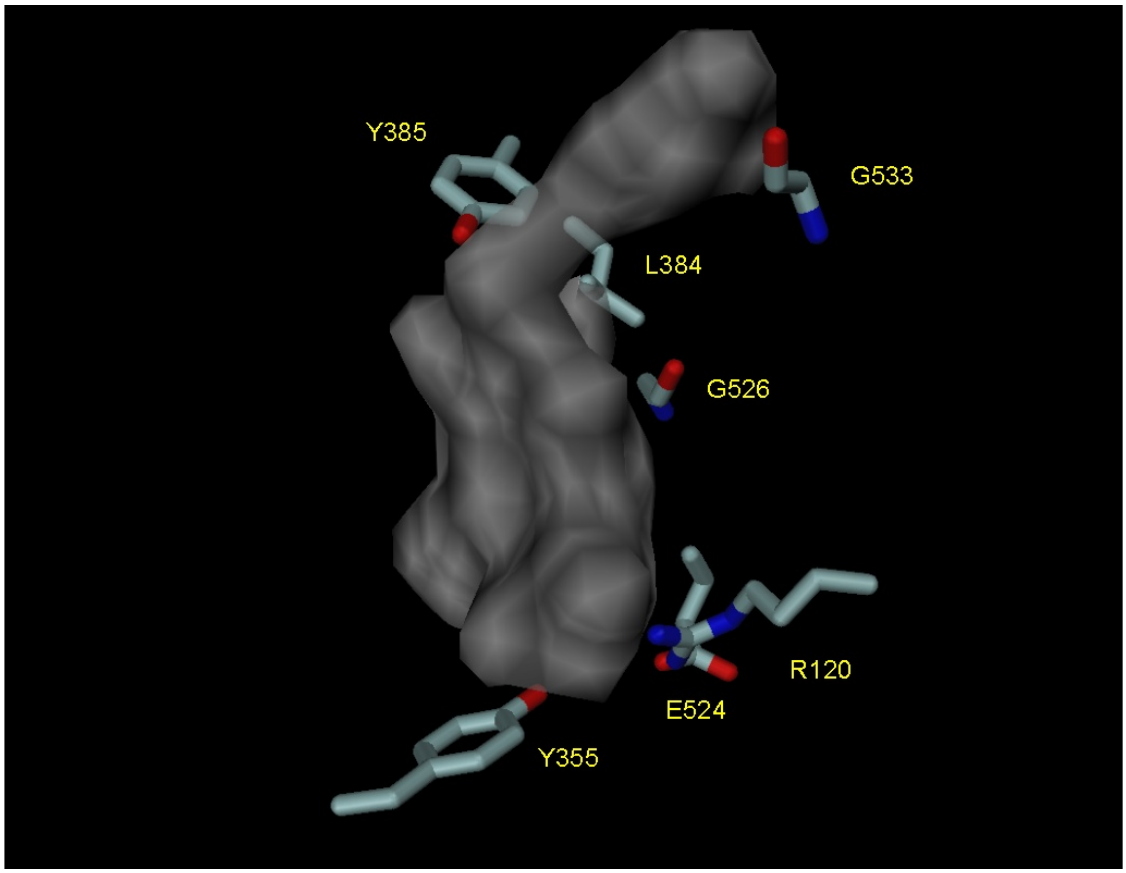

Figure I-3. The grey surface shows the arachidonic acid binding site in COX-1. Key amino acid side chains are highlighted, and described in the text below.

Gly-533 frames the "top" of the cavity. Mutations to bulkier residues at position 533 render COX inactive against arachidonate, though mutant COX will still oxygenate shorter fatty acid molecules (Rowlinson et al. 1999). At the the "bottom" of the AA binding cavity is the constriction site - a hydrogen bonding network consisting of Arg-120, Tyr-355, and Glu-524. Structural and functional studies suggest that Arg-120 forms a bidentate, charge-reinforced hydrogen bond with the AA carboxyl group, anchoring it for catalysis (Malkowski et al. 2000). To accomplish specific radical-mediated cyclization, the enzyme binds arachidonate in a bent "L shaped" conformation

that favors cyclization as an intermediate radical propagation step. In radical form, Tyr-385 specifically abstracts the the *pro*-S hydrogen atom from C13 to begin the cyclooxygenase reaction. Tyr-385 is ideally positioned for this, near the kink in the bound arachidonate (Rowlinson et al. 1999). The cyclization step is accomplished in a region of the binding site that includes a number of hydrophobic residues. Most notably, mutation of Leu-384 (or Gly-526) in this region of the binding site impedes the ability of COX to complete cyclization (Schneider et al. 2004).

Binding AA in a catalytically competent orientation is necessary, but insufficient to explain the reaction mechanism. Tyrosine must be oxidized to a free radical before catalysis can begin. Depicted in Scheme I-3, the initiation of the tyrosyl radical begins at the heme group bound near the COX peroxidase site. There, cleavage of hydroperoxides activates COX via a two electron oxidation of the resting Fe^{3+} heme. The resulting cationic, radical porphyrin binds Fe^{4+} coordinated to the freed atom of oxygen. This radical system has significant oxidizing potential and removes one electron from Tyr-385 to yield a tyrosyl radical.

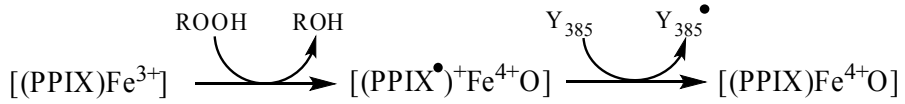

Scheme I-3. Cleavage of hydroperoxides at the peroxidase site results in a two-electron oxidation of the heme prosthetic group. A subsequent one-electron oxidation of Tyr-385 creates the tyrosyl radical which initiates the cyclooxygenase reaction (scheme I-2).

Abstraction of the AA 13-*pro*-S hydrogen by Tyr-385 results in a pentadienyl radical, centered on C11, C13, and C15. Next, oxygen adds to the *pro*-R face of C11. Prior computational studies by our group suggest that oxygen's preference for the *pro*-R

face of C11 is not only attributable to steric crowding of the other five possible reaction sites – but that it is also conferred by the specific channeling of oxygen to this reaction site. Once a dioxygen radical has added to C11, its subsequent attack of the C8-C9 double bond is kinetically favorable (Furse, Pratt, Schneider, et al. 2006). C8 then attacks C12, closing the endoperoxide ring and forming an allylic radical centered on C13, C14, and C15. The second oxygen is added at C15 with *S* stereochemistry. The phenolic Tyr-385 hydrogen is abstracted by the oxygen radical, completing the synthesis of PGG_2, and regenerating the Tyr-385 radical for another cycle of catalysis (Rouzer and Marnett 2003).

Mutagenesis implicates Ser-530 and Val-349 in the stereochemistry of the second oxygenation, as certain mutations at these positions strongly shift the COX product profile from 15S to 15R PGG_2 (Schneider et al. 2002). A model derived from a crystal structure suggests that Tyr-348, Phe-381, Tyr-385, and Ser-530 all work to sterically block oxygen addition to the opposite face of the allyl radical (Kiefer et al. 2000). In ongoing research, we hope to shed additional light on the dynamics of the microenvironment around C15, and identify enzyme channels that may participate in PGG_2 release.

Inhibition

In order to out-compete binding of arachidonic acid, COX inhibitors must bind well to the cyclooxygenase active site. This requires reasonable complementarity to the active site geometry and the pairing of ligand hydrogen bond donor/acceptors with active site residues (Miyamoto and Kollman 1993). In light of the above tour of the COX active

site, and the reaction mechanism that it supports, the key structural components of common NSAIDs are not surprising. Many inhibitors feature carboxylate moieties – and crystal structures have often, but not always, revealed these carboxylates to interact with Arg-120, as arachidonate does. All COX inhibitors feature hydrophobic moieties which can favorably desolvate into the hydrophobic channel of the cyclooxygenase active site. Structures of a few representative NSAIDS are shown in Figure I-4

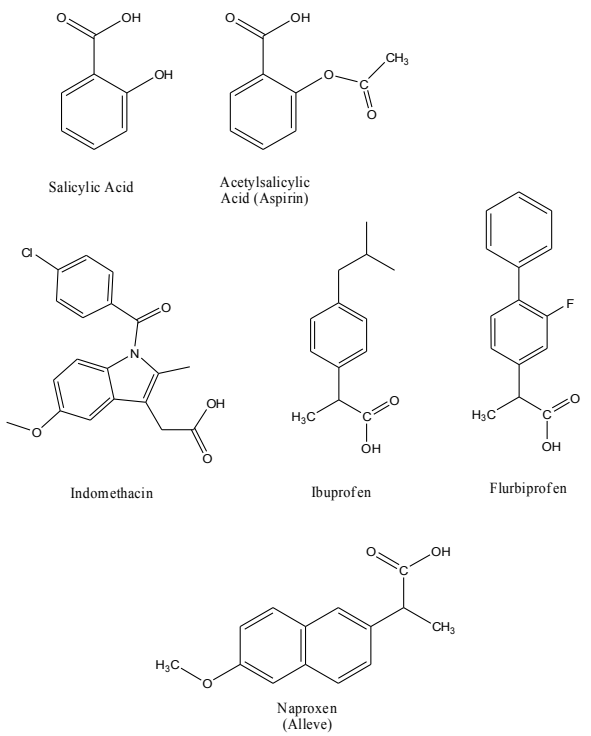

Figure I-4. Examples of COX inhibitors (NSAIDs)

Salicylic acid extracted from willow bark is a weak COX inhibitor – and was used as a pain reliever since antiquity. Hoffman acetylated salicylic acid in the late 19th century to form the much more potent compound acetylsalicylic acid (aspirin), arguably

the most successful pharmaceutical in history. The 1982 Nobel Prize in Medicine was shared by John Vane for his revelation that aspirin reduces prostaglandin levels, by inhibiting COX (Vane 1971). Structurally, the acetyl moiety of aspirin acetylates Ser-530 and projects the acetyl group bulk into the COX active site, essentially inhibiting the enzyme irreversibly. Other COX NSAIDs bind reversibly, through non-covalent interactions.

A diverse array of small molecule NSAIDs have been discovered. Derivatives of the NSAID indomethacin are important to much of the research in this dissertation. The crystal structure of indomethacin bound to COX-2 was solved to 3.0 Å. (Kurumbail et al. 1996) and key interactions of the bound inhibitor are shown in Figure I-5 below.

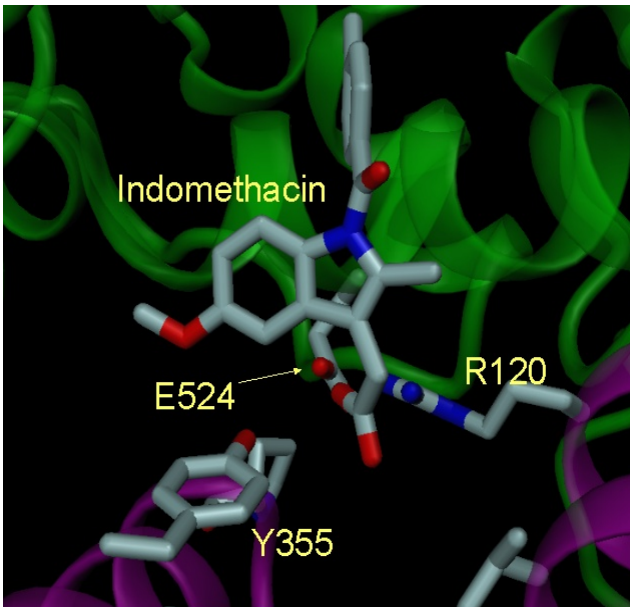

Figure I-5. Indomethacin bound to COX-2 (4COX.pdb).

On binding to the cyclooxygenase active site, indomethacin's carboxylate forms a charge-reinforced hydrogen bond to Arg-120. The N-*para*-chlorobenzoyl moiety projects

"up" into the hydrophobic active site, and fills the same cavity where the cyclization of oxidized arachidonic acid occurs.

All traditional COX inhibitors cause an unfortunate side-effect in many patients. Prostaglandin PGE_2 (red in Figure I-2) plays a vital role in maintenance of gastric mucosa, and the prolonged ingestion of COX inhibitors is highly ulcerogenic. Thus, for patients prone to ulcers, COX inhibition is an unsuitable strategy for long-term management of chronic inflammation which accompanies diseases like rheumatoid arthritis.

COX-2

In the 1980s, Needleman showed that cytokines and growth factors resulted in heightened COX expression (and activity) in fibroblasts (Whiteley and Needleman 1984; Raz et al. 1988). In 1991, a Harvard team cloned a cDNA of this intriguing up-regulated COX enzyme, and revealed it to be 60% sequence identical to mammalian COX (Xie et al. 1991). The following year, a UCLA team expressed this inducible enzyme in COS cells and showed it to have cyclooxygenase activity (Fletcher et al. 1992). Two COXs (now named COX-1 and COX-2) with differing expression profiles were firmly identified (Feng et al. 1993) and it was subsequently reported that a COX-2 selective inhibitor reduced inflammation without reducing prostaglandin production in the stomach (Seibert et al.1994). These data, in conjunction with a large number of other supporting studies, established and validated the COX-2 inhibitory hypothesis. Namely, whereas COX-1 is constitutively expressed ubiquitously and most strongly associated with prostaglandin production in gastric mucosa and thromboxane production in platelets,

COX-2 is expressed primarily in the CNS and at sites of inflammation. Thus, the development of COX-2 selective inhibitors should afford a therapeutic strategy for chronic inflammation treatment, without the gastric toxicity observed by non-selective inhibitors (Smith et al. 1996; Smith et al. 2000).

Val-523: The Billion Dollar Residue

Prior to reports of the first COX-2 crystal structures (Luong et al 1996), sequence analysis revealed that COX-2 was 60% identical to COX-1. Visual inspection of an early COX-1 crystal structure (Picot et al. 1994) revealed a handful of COX-1/2 divergent residues which might impact the geometry of the enzyme active site. Of several mutants constructed, the hCOX-2 V523I mutant was the most resistant to inhibition by the three COX-2 selective inhibitors assayed (Gierse et al. 1996). The emerging opinion that the size of the 523 side chain was the critical determining factor in COX-2 inhibition was further supported by the V523A mutation, which retained sensitivity to COX-2 selective inhibitors (Guo et al. 1996).

The structural basis for these functional results was confirmed with COX-2 crystal structures (Luong et al. 1996) that showed the I523V substitution affords COX-2 a larger solvent accessible cavity in which selective inhibitors might bind (depicted in Figure I-6 below).

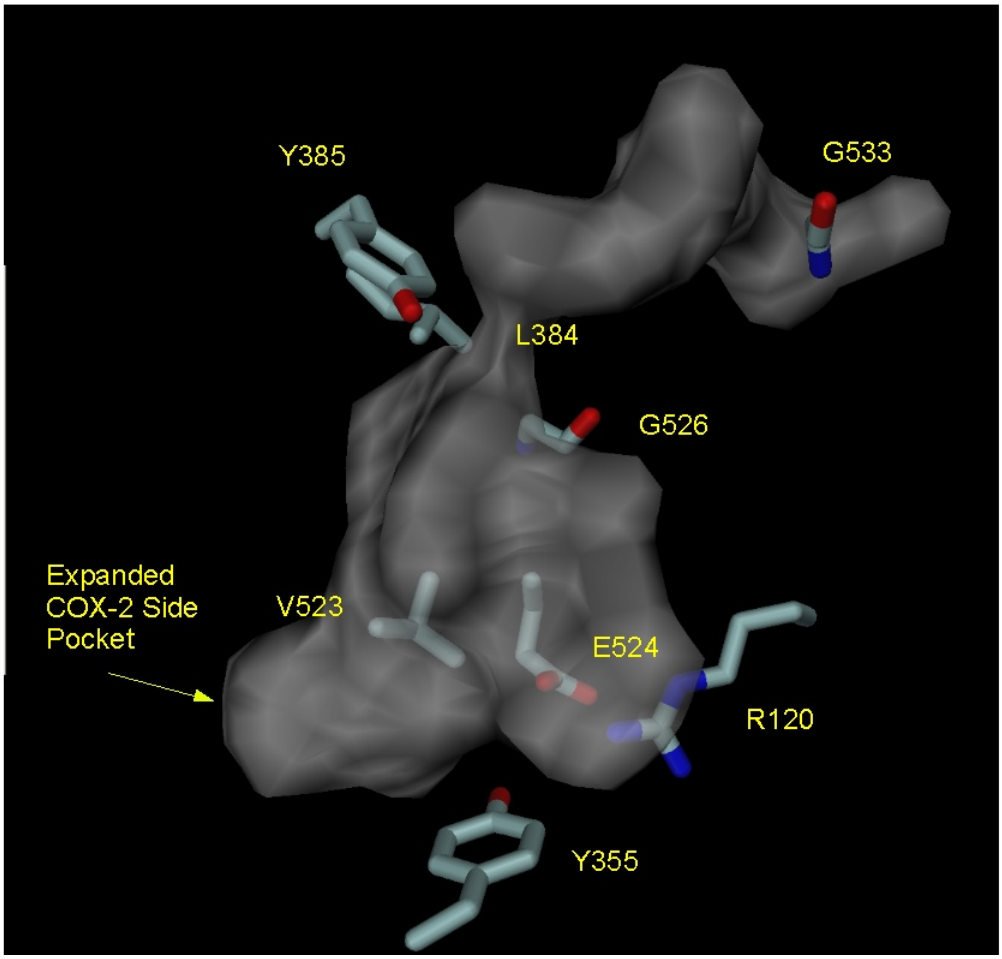

Figure I-6. The solvent accessible surface of the COX-2 active site (compare to the COX-1 surface shown in Figure I-3). Residue 523 is valine in COX-2 and isoleucine in COX-1. This affords bound ligands access to an expanded "side-pocket" in the COX-2 enzyme.

While V523I reduced the potency of the compounds vs. wildtype COX-2, potency against the mutant was not eliminated entirely. And, the remaining inhibition was no longer time-dependent. A reverse mutant of COX-1 (I523V) showed partially restored sensitivity to the COX-2 selective inhibitors, and the double mutation H513R/I523V completely restored sensitivity to time-dependent inhibition (Wong et al. 1997). Shown in Figure I-7 below, the X-ray crystal structure of COX-2 selective inhibitor SC-558 bound to COX-2 (Kurumbail et al. 1996) confirmed the hypothesis that a COX-2

selective inhibitor could occupy the side-pocket space afforded by the "missing" methylene group of COX-2 Val-523.

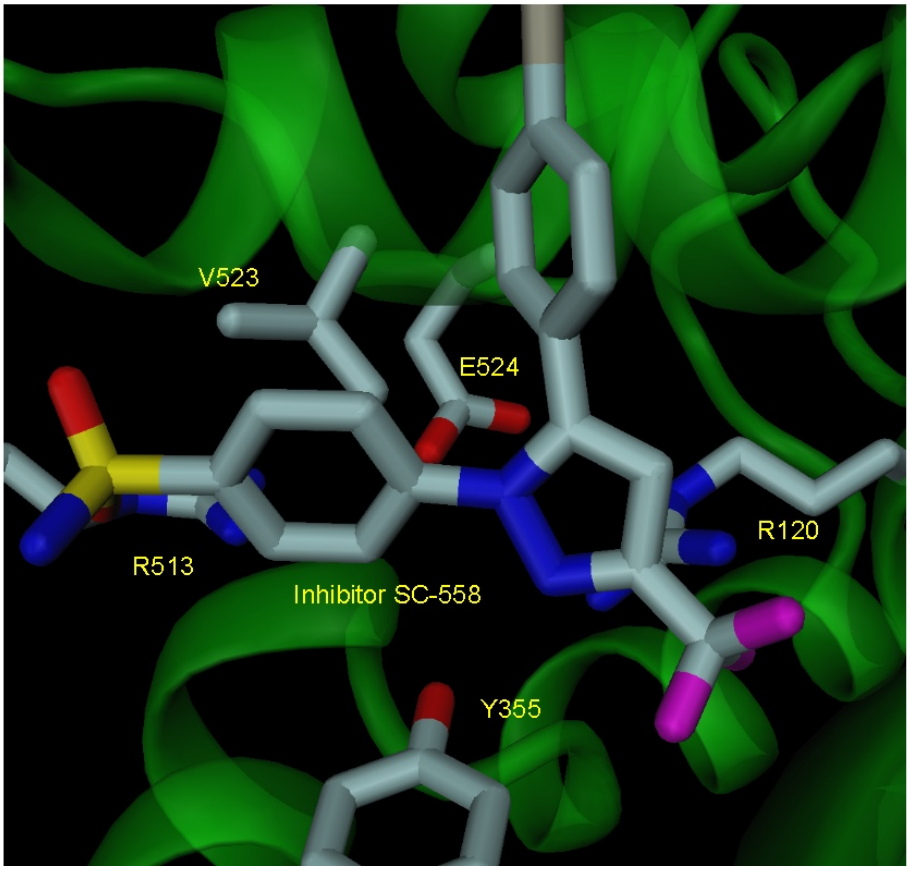

Figure I-7. COX-2 selective inhibitor SC-558 bound to the COX-2 active site (6COX.pdb). SC-558 selectively inhibits COX-2 by occupying the additional space afforded by Val-523 (Ile in Cox-1) Additionally, the sulfonyl moiety hydrogen bonds to the Arg-513 guanidinium group (513 is His in COX-1). Unlike most non-selective inhibitors, this ligand does not contain a carboxylate, and makes no charged interactions with Arg-120. Celecoxib has a methyl group where SC-558 has a bromine atom.

Two structures of the bound selective inhibitor SC-558 were deposited as the density did not allow for unambiguous orientation of the sulfonamide moiety of the ligand. An excellent example of the role computation can play was demonstrated in a detailed free energy perturbation calculation which identified the SC-558 conformer in

6COX.pdb as having a more favorable set of ligand-protein interactions than the conformer in 1CX2.pdb. Furthermore, assuming a rigid protein backbone around the active site, these calculations elucidated that Ile at position 523 forces SC-558 to adopt a less favorable torsion angle between its heterocyclic and phenyl-sulfonamide rings. Val-523 allows the two rings to relax an addition 12° away from co-planarity, to a lower energy conformation on average. This small change is sufficient to impart a 1 kcal/mol enthalpic penalty in the binding free energy (Plount Price and Jorgensen 2000) and these energetics are likely a key component in the selectivity of all the commercial diarylheterocycle COX-2 selective inhibitors (shown below in Figure I-8).

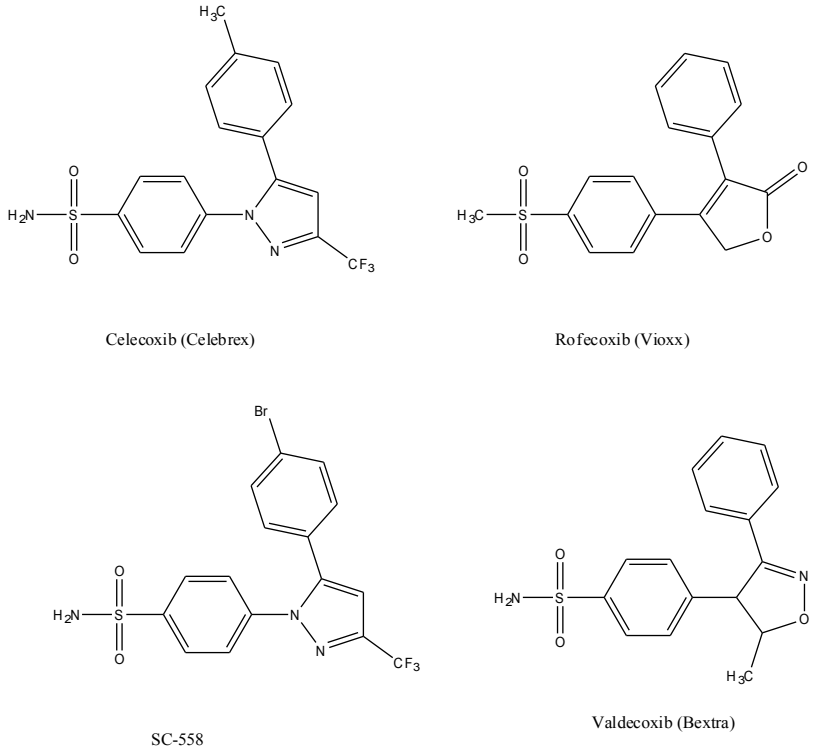

Figure I-8. COX-2 selective, diarylheterocycle, inhibitors.

The initial promise of COX-2 selective inhibitors was enthusiastically greeted by the marketplace. The diarylheterocycles celecoxib (Celebrex) and rofecoxib (Vioxx) each achieved annual sales approaching US$5 billion.

Unfortunately, cardiovascular risks started to emerge in early, longer term studies of these compounds (Mukherjee 2001). Rofecoxib (Vioxx) was removed from the market following cardiac events in a longer-term trial of the drug for the chemoprevention of benign sporadic colonic adenomas (Fitzgerald 2004) Within days of withdrawing rofecoxib, Merck lost some US$25 billion in market capitalization. Celecoxib (Celebrex) continues to be sold, albeit with FDA mandated "black box" warnings. Celebrex sales have fallen 70%.

Alternate COX-2 Inhibition Strategies

Cardiac risks aside, the diarylheterocycles validated the COX-2 hypothesis, that COX-2 selective inhibitors alleviate inflammation with greatly reduced ulcerogenicity vs. traditional NSAIDS. Enzyme specificity is a known concern with the diarylheterocycles, as the sulfonamide-containing inhibitors celecoxib and valdecoxib can also inhibit carbonic anhydrase II (Weber et al. 2004). Thus, it might be possible that undiscovered COX-2 inhibitors, based on novel scaffolds, or exploiting previously uncharacterized differences in the isozymes, may yield safe and more effective therapeutics. These possibilities have, in part, motivated our ongoing computational research into COX, and we have endeavored to shed light on previously uncharacterized COX isozyme differences. We should note that the current body of mechanistic evidence points to downstream reduction of PGI_2 levels as the root cause of the coronary risk from extended

NSAID use – and thus cardiac risk is present even with non-selective NSAIDs (Fitzgerald 2007). Nonetheless, COX remains an important pharmacological target, with many promising clinical trials underway as of this writing. As one possible example of their therapeutic utility, COX-2 selective inhibitors may someday serve as cancer chemopreventatives (Gupta and Dubois 2001), and thus the risk of their administration may well be justified in some patient populations. Furthermore, the insights we gain into the study of COX may advance our understanding of other complex, membrane-associated enzyme systems.

One alternate molecular scaffold for the synthesis of COX-2 selective inhibitors has been traditional carboxylate-containing NSAIDs. Derivatives of these long-administered compounds might provide new inhibitors with proven safety and ADME profiles. In light of early emerging evidence for a larger COX-2 active site, synthetic chemists at Merck reasoned that bulkier derivatives of indomethacin might be COX-2 selective inhibitors, and they discovered several. Among them, indomethacin modified by the addition of chlorine atoms at the 1 and 5 positions of the *para*-chloro benzoyl ring (Figure I-9 below) is highly COX-2 selective (Black et al. 1996).

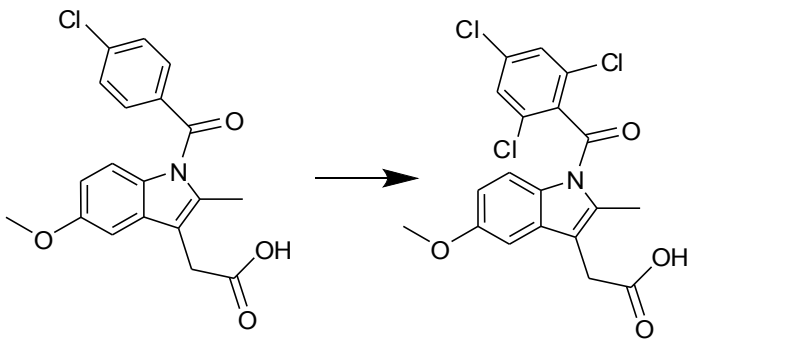

Indomethacin COX-2 Selective Inhibitor

Figure I-9. The addition of steric bulk converts indomethacin to a COX-2 selective inhibitor.

In addition to active site volume differences, an intriguing difference between the COX isozymes is the role of Arg-120. While the canonical NSAID binding motif features a bidentate charge-reinforced hydrogen bond between ligand carboxylates and Arg-120, the diarylheterocycles have no carboxylate moiety. Through mutagenesis studies, Arg-120 is known to be required for inhibition of COX-1 by traditional NSAIDS – but it is *not* required for inhibition of COX-2 by the same compounds. And, the methyl ester of indomethacin was reported to be a more potent inhibitor of COX-2 than COX-1 (Greig et al. 1997). Interestingly, while the R120Q mutant in COX-1 increases the apparent K_m for arachidonic acid by 1000-fold (Bhattacharyya et al. 1996), the same mutation in COX-2 has no impact on the K_m for AA, and actually *increases* the potency of COX-2 selective diarylheterocycles (Rieke et al.1999).

Indomethacin Amides

Related to these observations, the Marnett group found that neutralizing indomethacin with bulky amides (or esters) frequently yields a COX-2 selective inhibitor (Kalgutkar, Crews et al. 2000), as shown in scheme I-4 below:

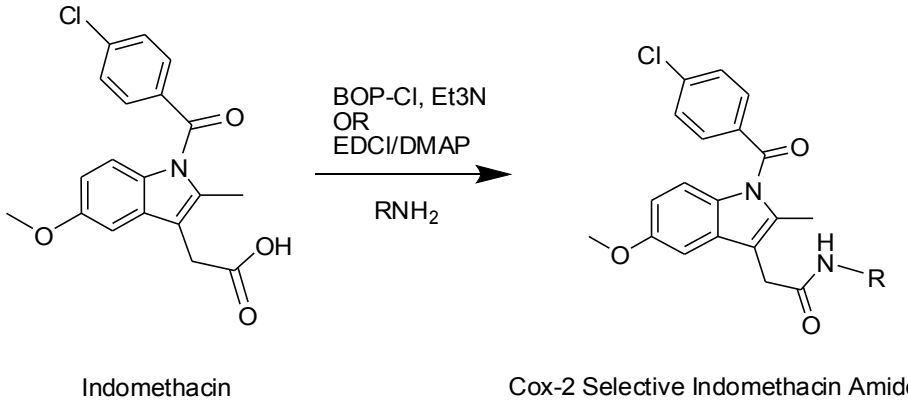

Scheme I-4. Coupling the free indomethacin acid to a bulky amine creates COX-2 selective inhibitors.

The mCOX-2 V523I mutation was found to not impact the selectivity of these compounds. With no obvious structural mechanism for the selectivity of these compounds, we employed computational methods to shed light on their structural and kinetic impacts.

Dissertation Overview

Chapter II will introduce the "lobby" region of COX, the area enclosed by the four orthogonal helices in COX's membrane binding domain (magenta in Figure I-1). In order for arachidonate (or inhibitors) to enter the active site, the compounds must exit the membrane, and transit through the constriction site to the cyclooxygenase active site. While most indomethacin-amides are COX-2 selective, the *S* enantiomers of α-substituted ethanolamide derivatives also inhibit COX-1. COX-1 selective inhibitors also may have therapeutic value, as it was shown that COX-1 is over-expressed in some ovarian cancer cells, where it stimulates angiogenesis (Gupta et al. 2003). Thus, a more detailed understanding of COX isoform differences could aid in the design of more selective, and potent, inhibitors of both COX isoforms. The research reported in this chapter explores this intriguing stereoselectivity, and explains the observed IC_{50}'s of the inhibitors in terms of binding energetics.

Chapter III explores the role of position 472 in COX-2 selective inhibition. Residue 472 (Leu in COX-2, Met in COX-1) is a "second shell" residue in all COX crystal structure. As such it cannot make direct contact with bound indomethacin amides in the COX-2 active site. However, Mary Konkle in the Marnett group identified this mCOX-2 residue, from many mutations she assayed, as slowing the on-rate of the indomethacin amides by up to 100x. Our calculations have revealed a compelling explanation for her kinetic observations.

Chapter IV introduces ongoing research into the dynamics of the Cyclooxygenase channel network. A great mystery in COX (as in many other enzymes with deeply buried active sites) is how the reaction product exits the enzyme. This mystery is particularly

profound as experimental evidence suggests that PGG_2 is shuttled to the peroxidase site. Analysis of channel opening events in molecular dynamics trajectories for COX with bound PGG_2 and the precursor allyl radical yields some light on a potential product exit route. A side-goal of this trajectory analysis is to better understand the dynamic component of the second oxygen addition, which COX remarkably constrains to the *pro-S* face of C15.

CHAPTER II

ENANTIOSELECTIVE INHIBITION OF CYCLOOXYGENASE-1

Background

Previously, a wide range of ester and amide derivatives of the nonselective carboxylate-containing NSAID indomethacin were synthesized and found to selectively and potently inhibit COX-2 (Kalgutkar, Marnett, et al. 2000). If these inhibitors bind to COX-2 in a manner consistent with the published crystal structure for the COX-2/indomethacin complex (Kurumbail et al. 1996), the indole ring C3 position side chain projects through a constriction site formed by the Arg-120/Glu-524/Tyr-355 triad, and into a cavity bounded by the four membrane-binding helices. This cavity is commonly referred to as the "lobby" region in COX (Kalgutkar, Marnett et al. 2000) and is shown in figure II-1.

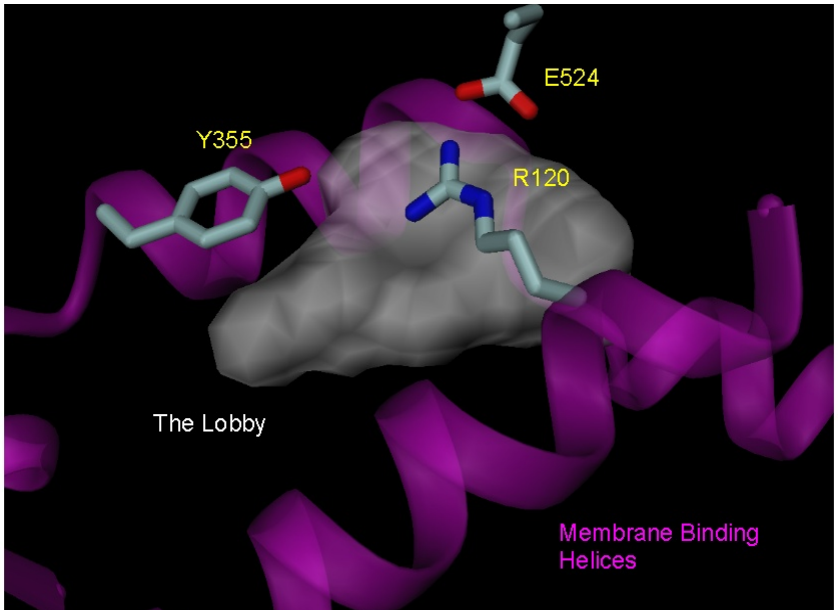

Figure II-1. The COX Lobby region (grey surface) is a cavity bounded by the four membrane-binding helices (purple). In order to enter the active site, ligands must travel from the membrane, through the lobby, and pass between the three constriction site residues shown.

Two crystal structures for COX-2 complexes with selective inhibitors (zomepirac derivatives) have been published (Luong et al. 1996). These crystal structures confirm that the zomepirac analogs do project into the lobby region, but specific interactions between these ligands and COX membrane-binding helix residues were not identified and the structures remain undeposited. In one of these crystal structures, the typically observed constriction site triad is rearranged substantially. The Glu-524 residue hydrogen bonds to Arg-513 rather than Arg-120, and the Arg-120 sidechain rotates away from the constriction site and hydrogen bonds to the backbone carbonyls of Glu-524 and Phe470. The second half of the fourth membrane-binding "D" helix, which includes Arg-120, unwinds partially. The Arg-120 Cα is displaced 2.3Å away from the active site, relative to other published COX crystal structures. This conformational rearrangement

generates a notably larger binding pocket in the COX-2 isoform. No COX-1/ligand complex crystal structures available to date exhibit a comparably enlarged binding site. Moreover, in COX-1, residue 513 is a histidine rather than an arginine, so it is possible that COX-1 cannot undergo comparable conformational changes. If only the COX-2 isoform is able to adopt an alternate, enlarged binding site conformation, this could explain the COX-2 selective inhibition observed for a wide variety of bulky indomethacin ester and amide derivatives (Kalgutkar, Marnett, et al. 2000).

An exception to COX-2 selective inhibition by indomethacin amide derivatives was discovered in the case of α-substituted indomethacin ethanolamides. While α-(*R*)-alkyl indomethacin ethanolamides are potent COX-2 selective inhibitors, α-(*S*)-alkyl and α-dimethyl substituted indomethacin ethanolamides inhibit both COX isoforms well (Kozak et al. 2002), as shown in Table II-1.

Table II-1. Inhibition of wild-type cyclooxygenases by α-substituted indomethacin ethanolamides (Kozak et al. 2002). The binding free energy for each ligand with COX-1 is computed directly from the IC_{50} values.

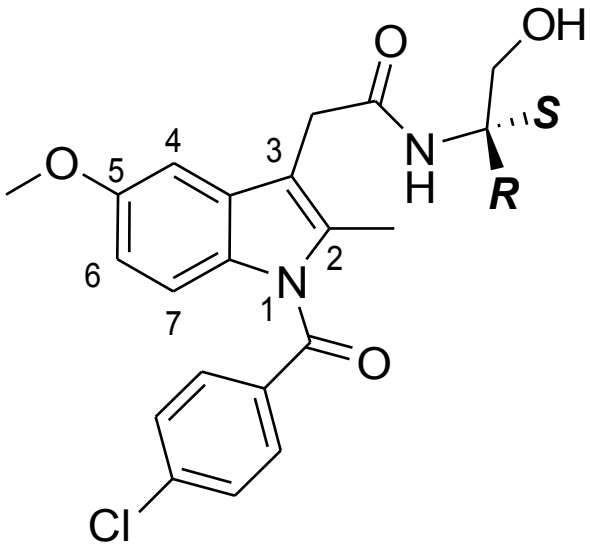

α-substituent	***R***	***S***	Ovine COX-1 inhibition IC_{50} (μM)	Human COX-2 Inhibition IC_{50} (μM)	Estimated ΔG_{bind} to Ovine COX-1 (kCal/Mol)
R-methyl	CH_3	H	33	0.17	-6.4
S-methyl	H	CH_3	0.59	0.27	-8.8
R-isopropyl	$CH(CH_3)_2$	H	>63	0.11	> -4.6
S-isopropyl	H	$CH(CH_3)_2$	0.40	0.37	-7.7
R-phenyl	C_6H_5	H	47	0.44	-4.7
S-phenyl	H	C_6H_5	<1.3	0.085	< -6.9
dimethyl	CH_3	CH_3	0.80	0.19	-7.2

Here, we focus our attention on the COX-1 isoform, hypothesizing that COX-1 does not undergo major constriction site reorganization or binding site expansion upon binding of indomethacin ethanolamides. Our modeling studies suggest that the α-substituted indomethacin ethanolamide derivative side chains interact with COX-1 through a network of hydrogen bonds to Glu-524, Arg-120, and Tyr-355 and through hydrophobic interactions which involve primarily Pro-86, Ile-89, Leu-93, and Val-116 in

the lobby region. Our studies further suggest that while both α-(*R*) and α-(*S*) stereoisomers can be accommodated well in the binding site, the α-(*R*) isomers must adopt an energetically strained conformation to form a comparable set of hydrogen bonding and van der Waals interactions with the enzyme relative to the α-(*S*) isomers.

Methods

Three-dimensional models for all indomethacin ethanolamide analogs listed in Table 1 were generated using crystal structure coordinates for indomethacin (Kurumbail et al. 1996) as a template. A systematic search procedure was used to sample ethanolamide side chain conformations for each molecule, and all conformers were then energy minimized. A clustering algorithm was used to eliminate redundant conformers (I.e., conformers with RMSD < 0.3 Å), and all remaining conformers within 8 kcal/mol of the global minimum energy conformation were retained for subsequent ligand docking studies.

Crystal structures for flurbiprofen methyl ester bound to ovine COX-1 (1HT5) and indomethacin bound to COX-2 (4COX) were used as reference structures to guide manual ligand docking exercises. Protein backbone atoms for the COX-1 complex were superimposed onto the COX-2 reference structure (backbone RMSD = 0.86Å) to project a plausible reference position for indomethacin in the COX-1 binding site. Crystallographic waters, including active site waters, and detergent molecules observed in the 1HT5 structure were retained in all models. The indole ring of each ethanolamide derivative was then superimposed on the indomethacin indole ring in this reference template. Each ethanolamide derivative was shifted down in the binding pocket toward

the lobby region by ~1Å to improve ligand-protein contacts, as suggested by crystal structures for flurbiprofen and zomepirac derivatives with COX-2 (Luong et al. 1996). Binding site residue side chains were adjusted to reduce bad steric contacts with ligands, using a systematic conformational search procedure and a backbone-dependent side chain rotamer library (Dunbrack and Karplus 1993). All ligand conformers with serious binding site steric clashes were discarded, and the remaining complexes were refined with energy minimization and limited, low temperature molecular dynamics to relieve any residual bad protein-ligand interactions.

Each refined complex was solvated with SPC/E water (Berendsen et al. 1987) in a truncated octahedron periodic box, and two sodium cations were added for net charge neutrality. Water and cation positions were relaxed with 1000 steps of conjugate gradient energy minimization, while keeping all protein, ligand, and detergent atoms fixed. Next, all protein, ligand and detergent atoms were refined with 1000 steps of energy minimization, while water and counterions were held fixed. Finally, the entire system was relaxed with 1000 additional steps of energy minimization. The minimization procedure was followed by 20 ps of low-temperature molecular dynamics, allowing only water, ligand, detergent molecules and counterions to move freely. A thermalization procedure was then used to prepare the system for equilibrium molecular dynamics simulation. Initial velocities for each atom were assigned from a Boltzmann distribution at 310K, followed by a 0.2 ps MD simulation. This procedure was repeated ten times with a different Boltzmann velocity distribution in each cycle, and then equilibrium MD simulations were run for each complex. A weak harmonic restraint (20 kcal/mol/Å) was applied to tether the heme prosthetic group securely to its histidine ligand in each

monomer. Each complex was equilibrated for several hundred picoseconds until total energies and structural fluctuations stabilized. Various low energy configurations were selected from these initial MD trajectories, and used as starting points for subsequent, more extensive (1-1.5ns) equilibrium MD simulations, so that several trajectories were available for analysis for each complex. The final 800 ps of each trajectory was used for subsequent energetic and structural analysis.

Standard AMBER all-atom potential functions were used for these calculations. Atom types and all necessary potential function parameters for ethanolamide ligands were assigned by analogy with existing parameters. Optimized geometries for each ligand were obtained from Hartree-Fock calculations with a 3-21G* basis set. Partial charges for each ligand were derived from ab initio molecular electrostatic potential calculations using a 6-31G* basis set, followed by fitting of the electrostatic potential to an atom-centered point charge model. Charge fitting was constrained to insure that R and S stereoisomers had identical partial charge assignments. The resulting ligand parameters are documented in Appendix A. All energy minimization, molecular dynamics, energetic and structural analysis calculations were performed with the AMBER 7 suite of programs (Case et al. 2002). A 1 femtosecond integration time step was used in all MD simulations, with a 9 Å nonbonded cutoff and partical-mesh Ewald summation to correct for long-range electrostatic interactions. Relative ligand binding free energies were estimated using the MM-GBSA protocol in AMBER (Massova and Kollman 2000). Gaussian-98 was used for all ligand geometry optimization and molecular electrostatic potential calculations (Frisch et al. 1998), and partial charge fitting was performed using

the RESP program (Bayly et al. 1987). The MDDISPLAY program was used for visual analysis of MD trajectories (Callahan et al. 1996).

Results and Discussion

Based on prior extensive mutagenesis experiments (Kozak et al. 2002), it is hypothesized that indomethacin ethanolamide derivatives inhibit COX via binding at the active site, and not through some secondary (i.e., allosteric) interactions with the enzyme. Thus, we have attempted to generate COX-1/ligand complexes that are consistent with the mutagenesis data, and that also help explain the stereoselectivity profile.

It is well known that small changes to ligand structure can result in dramatically different binding orientations, and the crystal structure of the inhibitor diclofenac bound to COX-2 reveals that it binds with its carboxylate group interacting with Ser530 and Tyr385, rather than Arg-120 as seen for all other carboxylic acid ligand complexes with COX published to date (Rowlinson et al. 2003). Therefore, we chose to explore alternate active site orientations for each ligand. Attempts to place the ethanolamide ligands in a "flipped" binding site orientation, analogous to the COX-2/diclofenac structure, invariably led to severe protein-ligand steric overlap, and it appears that these compounds must bind in a more conventional orientation. Attempts were also made to rotate each ligand about the indole ring center of mass, but again these alternate ligand orientations produced serious steric clashes, and it appears that the ethanolamide derivatives' binding mode must be rather similar to that observed in the COX-2/indomethacin crystal structure.

In the initial model building process, the indole ring for each ethanolamide derivative was superimposed directly on the indole ring for the indomethacin template structure. While the indole ring core fits nicely in the active site in this position, there are unfavorable steric interactions between the ethanolamide side chain and Arg-120, regardless of which low energy ligand conformer is docked. Most of these unfavorable steric interactions were relieved by shifting the ligand indole ring ~1Å lower in the binding pocket towards the lobby region. This ligand displacement toward the lobby region is consistent with crystal structures that exhibit a comparable shift between a zomepirac amide derivative and flurbiprofen in the COX-2 active site (Luong et al. 1996).

Given a plausible placement and orientation for the indole ring core of each ligand, we explored potential interactions for the ethanolamide side chain in the lobby region. As can be seen in Table 1, COX-1 can accommodate *S*-isomer derivatives with relatively small aliphatic side chain substituents (E.g., methyl, isopropyl) and the achiral, dimethyl analog, but larger alkyl or aryl substituents are not tolerated as well. These data suggest that smaller aliphatic substituents likely interact with a small hydrophobic pocket somewhere in the lobby region. Manual docking of low energy conformers for each ligand reveals that compounds with isopropyl substituents form favorable van der Waals interactions with a hydrophic pocket formed by lobby residues Pro-86, Ile-89, Leu-93, Val116 and the aromatic ring of Tyr-355. The methyl and dimethyl derivatives also fit nicely, but compounds with larger substituents (E.g., phenyl) cannot be accommodated in this hydrophobic pocket without significant shifting of the ligand, and concomitant

disruption of favorable protein-ligand interactions. These models thus provide a simple explanation for the ligand binding preferences as a function of side chain size.

While these models explain the size constraints for ethanolamide side chain substituents, they do not provide a clear explanation for stereoselective binding of these compounds. Low energy conformers for both R and S isomers can fit well in the lobby region, forming a strong hydrogen bond between the side chain hydroxyl group and Glu-524. Since manual ligand docking and structural refinement did not suggest any clear explanation for stereoselectivity control, we generated several relatively long (1-1.5 ns) equilibrium MD trajectories for each complex to assess energetic contributions and stability of ligand-protein interactions.

We used the MM-GBSA protocol (Massova and Kollman 2000) to estimate ligand binding free energies from each equilibrium MD trajectory, and identified those trajectories yielding the most energetically favorable complexes for each ligand. We did not compute entropy contributions explicitly, since the large size of these complexes makes normal mode calculations impractical, and the trajectories are not sufficiently long to obtain reliable entropy estimates from quasi-harmonic analysis. However, we reason that the entropy contribution will be quite comparable for different trajectories of a particular ligand-enzyme complex, and probably for trajectories with different stereoisomers. The entropy contribution *might* be comparable for all the ligand-enzyme complexes, since the ligands are all quite similar. However, this is a rather tenuous assumption, and we therefore did not attempt to make any rigorous quantitative comparison of binding free energies for different ligands. Total energies for the enzyme,

ligand, and the enzyme-ligand complex from the MM-GBSA calculations are listed in Table II-2 below.

Table II-2. MM-GBSA energy components for enzyme-ligand complexes. Total energy values are listed for the enzyme, ligand, and enzyme-ligand complex (standard deviations are listed in parenthesis), and include the Generalized Born solvation contribution. The binding energy estimate listed in column 4 is calculated as the total complex energy minus the enzyme plus ligand energies, but does not include the entropy contributions, and thus may be best regarded as a binding enthalpy estimate. All values are reported in kcal/mol units.

	Enzyme only	**Ligand only**	**Complex**	**Δ*H***
R-methyl	-26605.3 (89.0)	23.5 (4.8)	-26640.5 (89.1)	-58.7
S-methyl	-26540.2 (86.7)	21.2 (5.5)	-26576.3 (87.1)	-57.3
R-isopropyl	-26622.2 (90.5)	26.2 (5.2)	-26658.4 (89.9)	-62.4
S-isopropyl	-26518.8 (93.2)	21.0 (4.8)	-26561.4 (93.5)	-63.6

Experimental ligand binding free energies for S-methyl versus R-methyl and S-isopropyl versus R-isopropyl derivatives are listed in Table 1, calculated from the experimental IC_{50} values for these compounds. It must be noted that a simple correlation between IC_{50} ratios and relative binding free energies is not strictly true for enzymes that exhibit complex binding kinetics, but we also note that excellent correlation for IC_{50} values and computed binding free energies for celecoxib analogs was observed assuming this relationship in a previous study (Plount-Price and Jorgensen 2000). As can be seen from the data in Table II-2, the energy component terms are quite large, and the statistical uncertainty for most terms is larger than the estimated binding free energy difference for R versus S stereoisomers. Therefore, even if we did assume that the entropy

contributions are comparable for *R*- and *S*-stereoisomer complexes, we still cannot make definitive predictions about ligand binding preferences using these data.

Final energetic and structural results are derived primarily from analysis of these "energetically most favorable" trajectories, although all independent trajectories were considered in the analyses. In each case, the MD trajectories exhibiting less energetically favorable complexes (i.e., less favorable ligand binding free energies based on MM-GBSA calculations) involved complexes with higher ligand conformational strain energy, and are a direct consequence of our decision to build initial complex models with several low energy conformers for each ligand. In many equilibrium trajectories, the strained ligand conformers relaxed to lower energy conformations, but in some trajectories the higher energy conformers appear to be effectively locked, because these higher energy ligand conformers facilitate optimal ligand-enzyme interactions. Thus, we observe that the net ligand binding free energies calculated from these trajectories are a relatively subtle balance between ligand-enzyme interactions and ligand conformational strain energy.

This balance of ligand-enzyme interaction energy with ligand conformational strain energy appears to successfully explain the stereoselective binding preferences for the ethanolamide analog series. As can be seen in Table II-2, the ligand energies are consistently lower for *S*-methyl and *S*-isopropyl ligands than for the corresponding *R*-stereoisomers. The solvation energy terms are essentially identical for ligand stereoisomers, so the ligand energy difference must reflect differences in conformational strain energies for *R*- versus *S*- stereoisomers in these complexes. To investigate this possibility more thoroughly, we performed detailed energy decomposition and structural analyses for 800 configurations from trajectories of each enzyme-ligand complex. The energetic analysis reveals that the R-methyl and R-isopropyl isomers do indeed have higher conformational strain energies on average than the S-methyl and S-isopropyl isomers as shown in Table II-3:

Table II-3. Total intramolecular strain energy for bound ligands. The total intramolecular energy for each ligand is computed as the average over the final 800 ps of equilibrium molecular dynamics trajectories for each complex. The intramolecular energy is a sum of bond stretch, angle bending, dihedral, and intramolecular van der Waals and electrostatics energy components (standard deviations are listed in parenthesis). [b] The relative conformational strain energy for *R* versus *S* isomers is listed in column 3. In each case, the *S* stereoisomer displays a more favorable conformational energy in the bound complexes. All energies are reported in kcal/mol units.

	R-isomer	*S*-isomer	ΔE^{b} (*R* vs. *S*)
α-methyl ligands	58.4 (4.8)	56.3 (5.0)	2.1
α-isopropyl ligands	66.3 (5.2)	61.5 (5.1)	4.8

While the energy fluctuations are reasonably large, as shown by the standard deviations in Table II-3, the trends observed over these trajectories are quite significant, and the *S*-isomers consistently adopt lower energy conformations, as can be seen from the plots in Figures II-2 and II-3 , which follow.

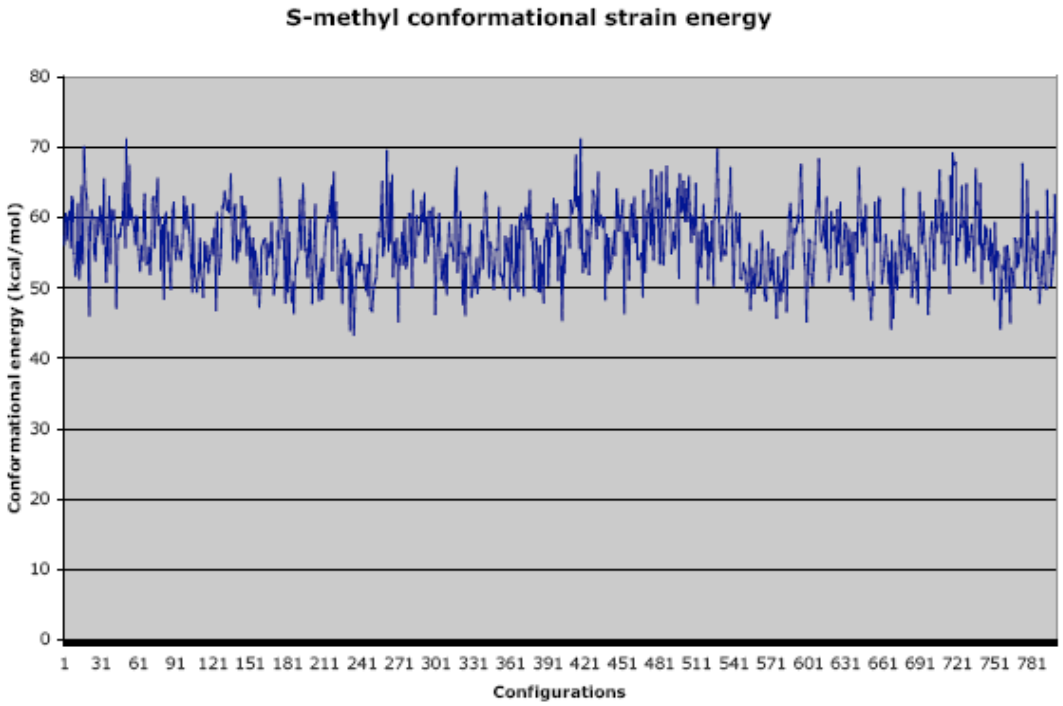

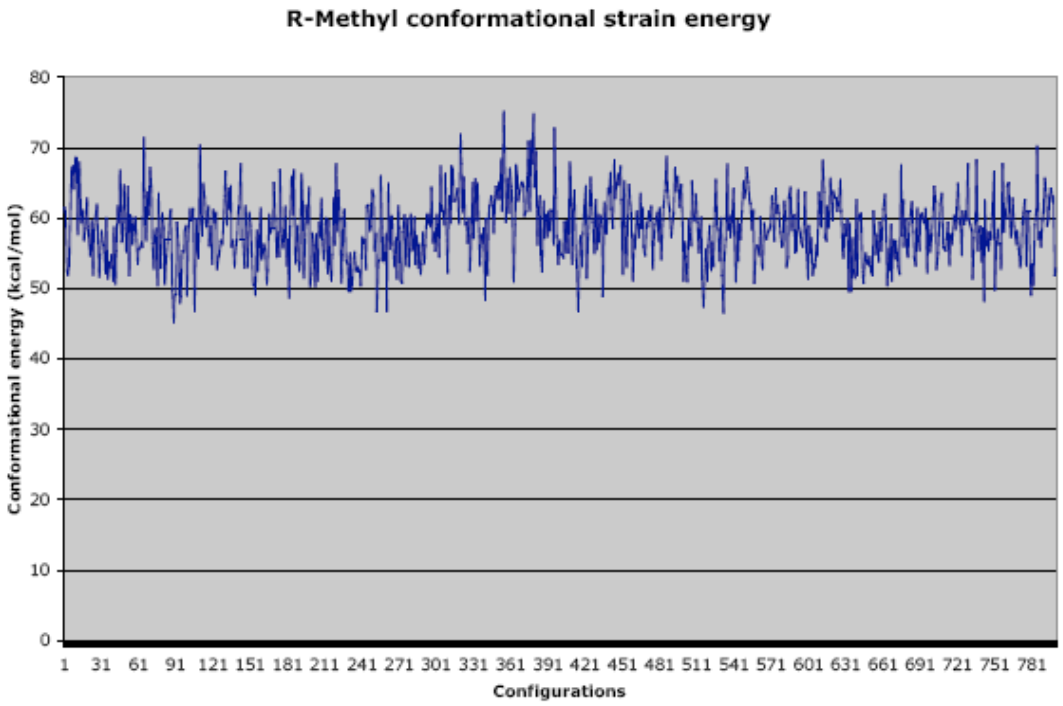

Figure II-2. Conformational strain energy for *S*-methyl and R-methyl compounds during the last 800 ps of equilibrium MD trajectories. The *S*-Methyl isomer consistently adopts a lower energy conformation. The conformational energies were calculated every picosecond and displayed as configurations 1-800.

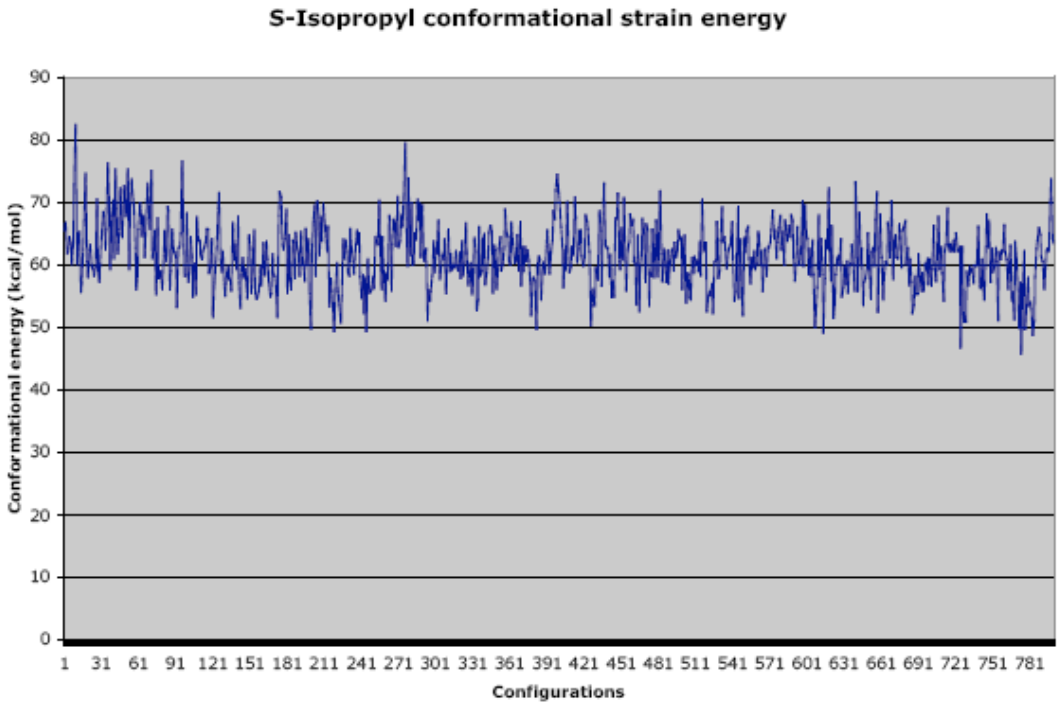

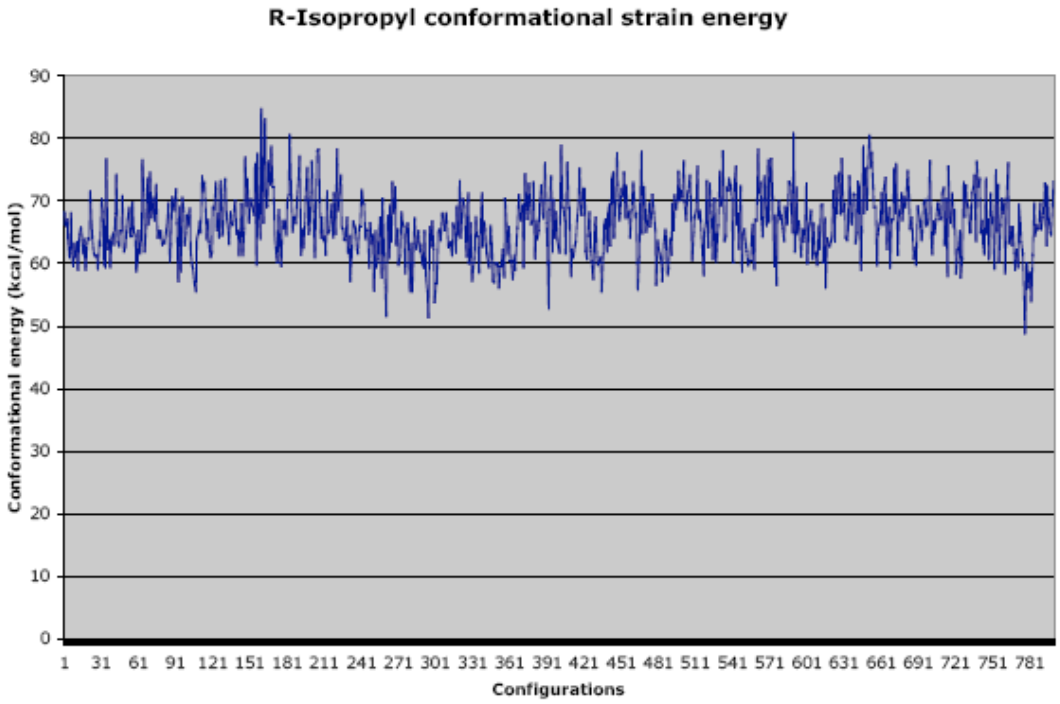

Figure II-3. Conformational strain energy for *S*-isopropyl and R-isopropyl compounds during the last 800 ps of equilibrium MD trajectories. The *S*-Isopropyl isomer consistently adopts a lower energy conformation. The conformational energies were calculated every picosecond and displayed as configurations 1-800.

The energy decomposition analysis further reveals that the ligand-enzyme interaction energies are statistically indistinguishable for corresponding *R*- and *S*-isomers, as shown in Table II-4.

Table II-4. Enzyme-ligand interaction energies. The enzyme-ligand interaction energies are computed as the average over the final 800 ps of equilibrium molecular dynamics trajectories for each complex (standard deviations are reported in parenthesis). All energies are reported in kcal/mol units.

	R-isomer	*S*-isomer
α-methyl ligands	-96.5 (3.2)	-94.1 (4.1)
α-isopropyl ligands	-99.4 (4.6)	-101.6 (4.7)

These results are consistent with the initial manual model building and structural refinement, which indicated that *R*- and *S*-stereoisomers formed equally good interactions with the enzyme. The structural analysis shows clearly that the *R*-isomers on average adopt a more strained conformation than the corresponding S-isomers, as seen in Figure II-4.

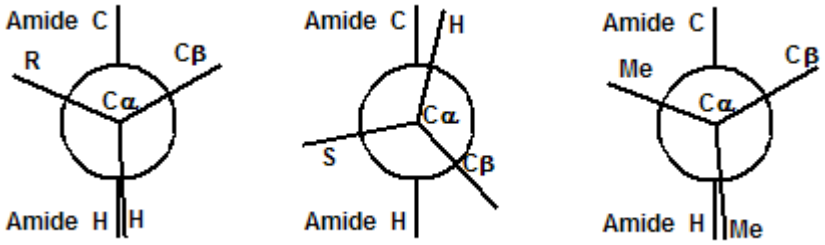

Figure II-4. Newman Projections of *R*, *S*, and dimethyl α-substituted indomethacin ethanolamides, placing the amide nitrogen behind the Cα atom. To bind to COX-1, *R* enantiomers must adopt a strained conformation in which the amide carbon is gauche to both the Cβ carbon and the alkyl substituent. The *S* enantiomers can bind without enduring this additional strain. The dimethyl compound adopts a gauche conformation similar to that of the *R* enantiomers, but this is the lowest energy conformation observed for the dimethyl analog.

Basically, these analyses indicate that the *R*-isomers generally adopt a conformation that places both the ligand Cβ carbon and the methyl or isopropyl substituent gauche to the amide carbonyl carbon, while the *S*-isomers position the Cβ carbon and alkyl substituent gauche to the amide hydrogen. In order to test whether these results might reflect bias in the original model construction and manual ligand docking, or simply inadequate configurational sampling in the MD simulations, we generated equilibrium MD trajectories starting with lower energy *R*-methyl and *R*-isopropyl conformers (i.e., conformations where the Cβ and alkyl side chains are positioned gauche to the amide hydrogen) docked in the binding site. For these trajectories, there was no significant difference in ligand conformational strain energy compared to the *S*-isomer complexes, but the ligand-enzyme interaction energies were 6-10 kcal/mol higher (i.e., less favorable) compared to the earlier *R*-methyl and *R*-isopropyl complex trajectories. Together, these results suggest that the *R*-methyl and *R*-isopropyl compounds can indeed optimize binding site interactions, and ultimately yield lower binding free energies, by adopting slightly strained conformations. The higher conformational strain energy for *R*- versus *S*-isomers correlates rather well with the experimental binding energies for *R*- versus *S*-isomers, and nicely explains the basis for stereoselective ligand binding in this ethanolamide analog series.

The equilibrium MD trajectories also provide additional structural information for the complexes. Several ligand-enzyme interactions are observed for all molecules in every trajectory, and probably represent the predominant, stabilizing interactions for the complexes. The ethanolamide side chain hydroxyl group forms a hydrogen bond with Glu-524, and the side chain amide carbonyl oxygen accepts a hydrogen bond from

Arg-120. These two hydrogen bonds are maintained consistently in all simulations. The ligand side chain amide NH forms a hydrogen bond with the Tyr-355 side chain, although this hydrogen bond does fluctuate and occasionally breaks in some of the trajectories, particularly for the dimethyl derivative. Lobby residues Pro-86, Ile-89, Leu-93, Val-116, and the aromatic ring of Tyr-355 make favorable van der Waals contacts with smaller alkyl substitutes in the ethanolamide side chain in all complexes, as shown below in Figures II-5 – II-7.

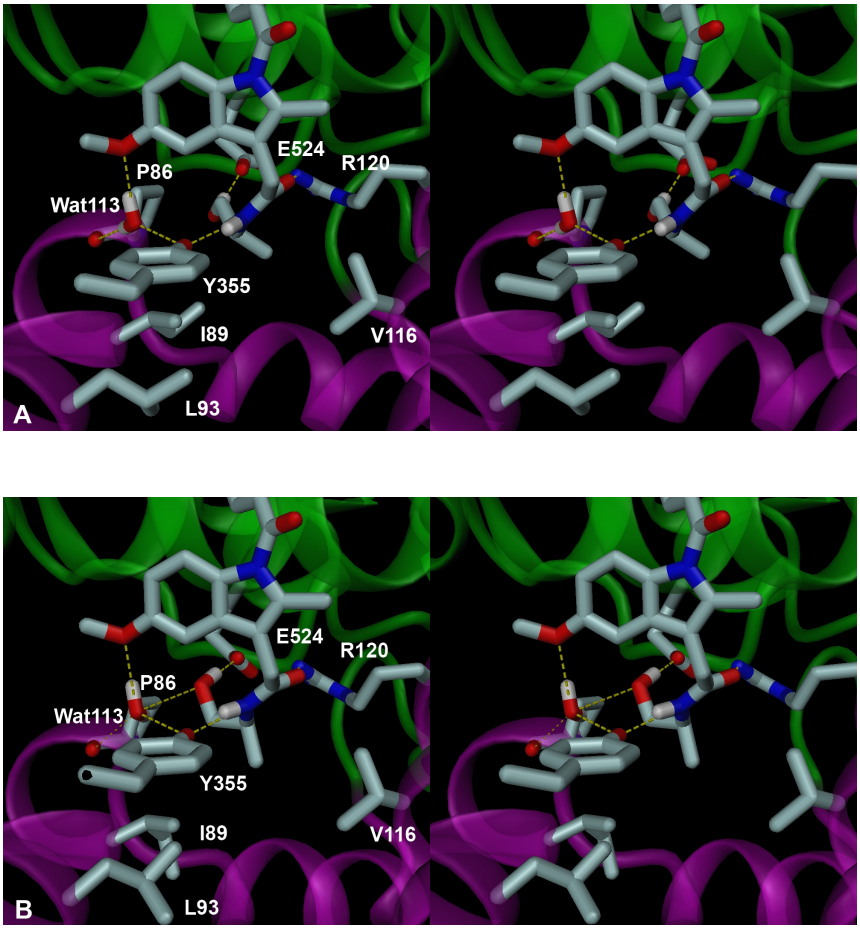

Figure II-5. Stereoview of (A) α-(*R*) and (B) α-(*S*) methyl indomethacin ethanolamide ligand bound to COX-1. Hydrogen bonds between ligand, protein, and crystallographic water are shown as dashed yellow lines. The ligand also makes van der Waals contacts with lobby residues P86, I89, L93, and V116. All figures were generated with the DINO program (Philippsen 2003).

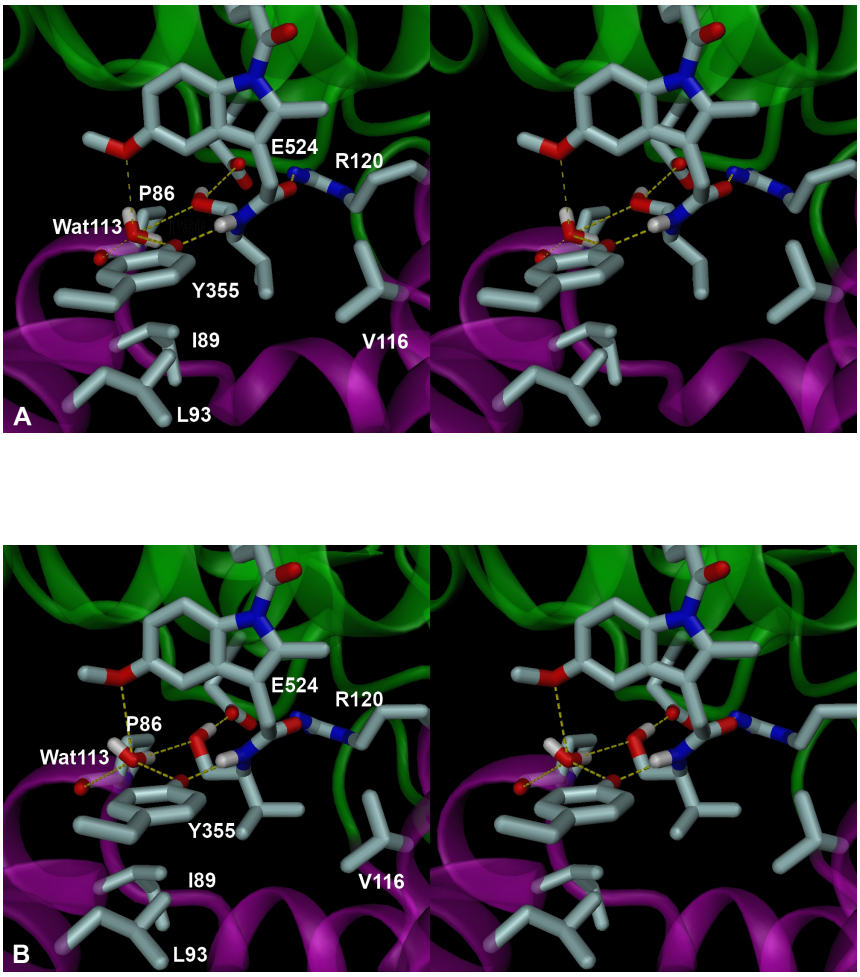

Figure II-6. Stereoview of (A) α-(*R*) and (B) α-(*S*) isopropyl indomethacin ethanolamide ligand bound to COX-1. Hydrogen bonds between ligand, protein, and crystallographic water are shown as dashed yellow lines. The ligand also makes van der Waals contacts with lobby residues P86, I89, L93, and V116.

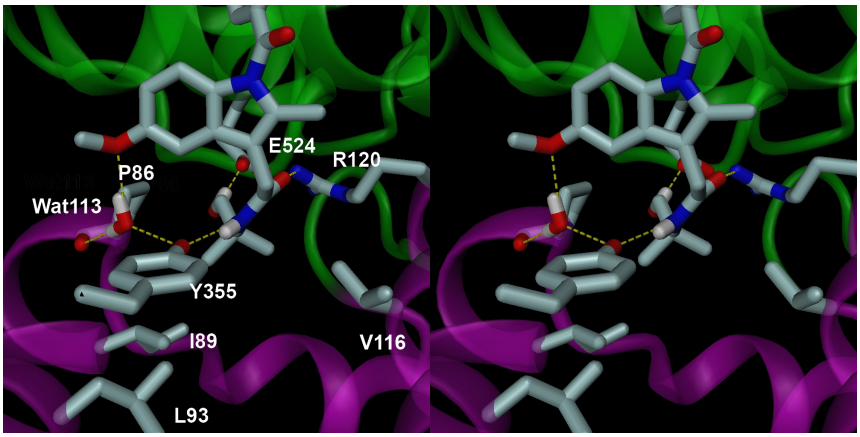

Figure II-7. Stereoview of α-dimethyl indomethacin enthanolamide ligand bound to COX-1. Hydrogen bonds between ligand, protein, and crystallographic water are shown as dashed yellow lines. The ligand also makes van der Waals contacts with lobby residues P86, I89, L93, and V116.

The simulations suggest that the pocket size does not fluctuate dramatically, so that larger side chain substituents like a phenyl group cannot be accommodated quite as well, as shown in Figure II-8.

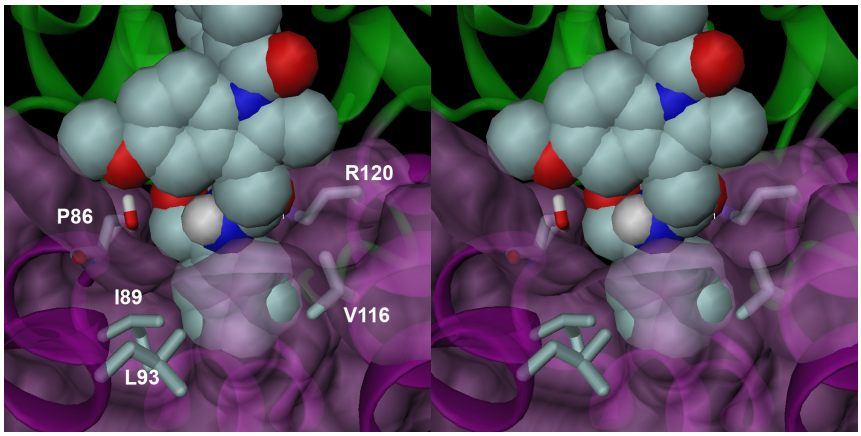

Figure II-8. Stereoview of α-(*S*) phenyl indomethacin enthanolamide ligand docked in COX-1. The ligand is rendered as a CPK structure, and the COX-1 lobby region is displayed with a translucent purple molecular surface. The intersection of the ligand CPK surface with the lobby region residues I89 and V116 highlights the unfavorable steric interactions observed for the phenyl derivative. The molecular surface was computed with the MSMS (Sanner 1996) program.

Water molecules also appear to play an important role in stabilization of the enzyme-ligand complexes. We retained crystallographic waters observed in the COX-1 reference structure used for all model building exercises, since it was easy to dock the ethanolamide derivatives in the binding site without removal of these waters. During the simulations, some of these waters did shift positions, and waters near the entrance of the lobby region can migrate freely and/or exchange with bulk solvent. Two water molecules are particularly well localized, however, and have important structural roles in the complexes. One water molecule forms a stable bridging hydrogen bond between the Glu-524 backbone carbonyl oxygen and the Arg-120 guanidinium side chain, anchoring these two residues strategically in the binding site, where both form key interactions with all ligands. This water molecule is present in the 1HT5 crystal structure, and although it exchanges occasionally with bulk water during our simulations, this particular water

molecule has a mean occupancy value of 1.0 in all trajectories and always forms this bridging hydrogen bond between Arg-120 and Glu-524, as observed in the crystal structure. A second key water molecule is buried more deeply in the binding site and forms a bridging hydrogen bond between Tyr-355, His-90, and Glu-524 side chains in the 1HT5 crystal structure. However, in all our simulations, His-90 rotates away from the ligand binding site to eliminate an unfavorable electrostatic interaction with the indole ring methoxy group, and this water molecule then forms bridging hydrogen bonds between the ligand side chain hydroxyl or indole ring methoxy substituents and nearby protein side chains (E.g., Tyr-355) or backbone carbonyl oxygens (E.g., Pro-84). While these hydrogen bonds fluctuate significantly during the simulations, this water molecule does remain well localized in the binding site (Figures II-5 - II-7). Bulk water molecules do occasionally enter the binding site and make direct contact with this buried water molecule, so that exchange with bulk water should be possible. However, we did not observe direct exchange with bulk water during the course of these simulations.

In summary, all ligands appear to form a consistent set of discrete interactions with enzyme binding site side chains. Both *R*- and *S*-stereoisomers form comparable interactions with the enzyme, but the *R*-isomers do so at the expense of modest conformational strain. The relative conformational stain energies for *R*- versus *S*-stereoisomers parallel the relative binding free energies for the stereoisomers extremely well. There appears to be little size fluctuation in the hydrophobic pocket of the lobby region, explaining why ethanolamide derivatives with larger aliphatic or aromatic substituents do not bind as well. Finally, it seems clear from these simulations that water molecules play a crucial role in stabilizing the ligand-enzyme complexes, either by

mediating ligand-enzyme hydrogen bonds or else by influencing enzyme side chain orientation in the binding site.

Other Proposals

The intriguing problem of selective inhibition of COX-1 by α-substituted ethanolamides has captured the attention of other research groups. Following the publication of our hypothesis (Moth et al. 2003) a computational group in Korea employed automated docking, followed by free-energy perturbation of COX-2 V523I, to develop an alternate hypothesis for enantioselectivity in the specific case of α-ethyl ethanolamides (Park and Lee 2005). A troubling facet of this paper is that enantioselectivity is explained in terms of the perturbation of Val-523 to Ile-523. Experimentally, this mutation has been shown to have no impact on the stereoselective inhibition of α-substituted ethanolamides (Kozak et al. 2002).

X-ray crystallography may have the greatest potential to explain the basis of enantioselectivity. In 2007, following a lengthy refinement process, crystal structures of *S*- and *R*- ethyl ethanolamides were published and deposited (Harman et al. 2007). In the case of the α-*(R)*-ethyl ligand, Harman's final adoption of a *trans* amide brought the inventory of ligand-protein hydrogen bonding contacts very close to our computational prediction. As predicted, the X-ray model depicts the amide nitrogen donating a hydrogen bond to Tyr-355, the ethanol moiety donating a hydrogen bond to Glu-524, and

the amide substituents oriented gauche to the amide carbonyl. On overlay of Harman's *R*-ethyl structure with our prediction is shown below in Figure II-9.

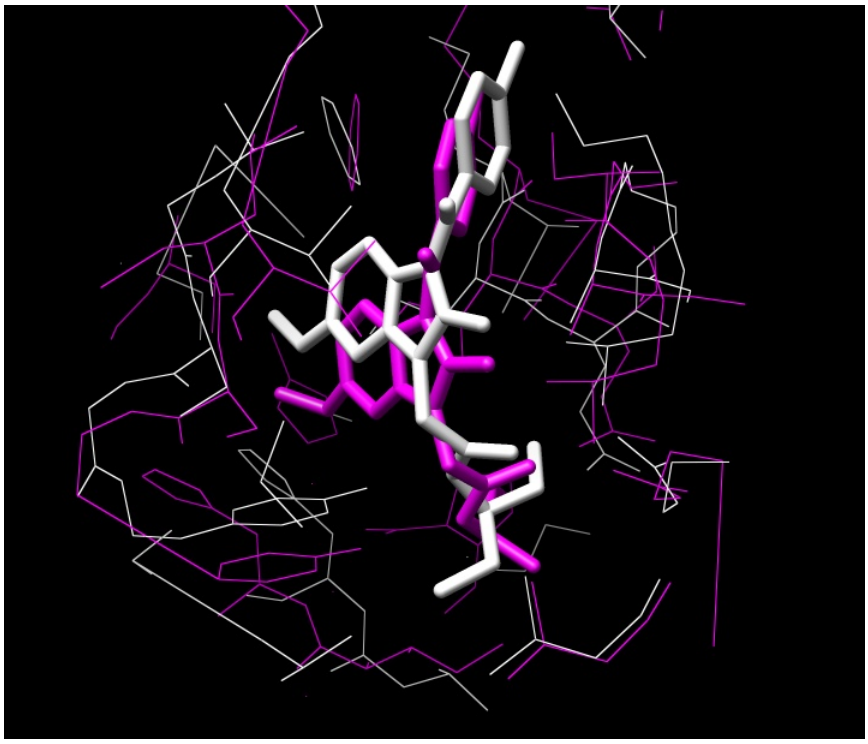

Figure II-9. RMS backbone fit of Harman's COX-1 X-ray structure of bound α-(*R*)-ethyl indomethacin (white) to our prediction for α-(*R*)-methyl indomethacin (magenta). Both models depict Tyr-355 accepting a hydrogen bond from the amide nitrogen, and Glu-524 accepting a hydrogen bond from the ethanol hydroxyl. Small differences in the register of the indole ring are consistent with the high temperature factors deposited for the ligand and Arg-120.

We also predicted that the amide carbonyl would receive a hydrogen bond from Arg-120. However, the register of the ligand atoms in the crystal structure does not depict any protein hydrogen bond to the amide carbonyl. Harman's paper describes Arg-120 is shifted away from the active site, relative to other COX structures. We had speculated that potent indomethacin-amide binding to COX-2 could well involve

displacement of Arg-120 away from the active site, as shown in the first, undeposited, COX-2 crystal structures (Luong et al. 1996) Thus, the small shift of Arg-120 in Harman's *R* crystal structure is not inconsistent with our analysis of previous COX-2 structures, or our initial manual docking which required a small shift of Arg-120. In fact, our Figure II-9 shows Arg-120 adopts a nearly identical conformation in both our average structure and the X-ray structure. Relative to our prediction, the X-ray structure depicts an upward shift in both the ligand indole ring, and Tyr-355 in the crystal structure. These small differences in our static structures may be best explained by the dynamics which are conveyed in the X-ray structure deposition itself. The 20YE.pdb structure diffracted to a resolution of 2.89 Å, and the temperature factors deposited for the key interaction points are quite high. Temperature factors of 81.76 were calculated for all ligand atoms, 78.09 for Arg-120 side-chain atoms, and 89.48 for Glu-524 side-chain atoms. Thus, our average computed structure and the deposited crystal structure are nicely consistent, given the structural fluctuations in the simulations and the large thermal fluctuations observed in the crystal structure.

In stark contrast to the similarity of our *R* enantiomer structures, the Harman's model pose of the *S* enantiomer structure (2OYU.pdb) is strikingly different from our prediction. The amide substituents chains project into the side-pocket of COX-1, an area previously thought to be only accessible in COX-2. The *para*-chlorobenzoyl moiety projects "down" into the lobby region, and the indole ring is rotated 90° so that the methoxy group projects "up" into the cyclization region of the active site.

Computation of a density map for the *R* isomer structure is straightforward, but we have been unable to compute a satisfactory density map from the *S* isomer structure

factors. Our calculations report an R-value of 0.359, which is much greater than the deposited R-value of 0.241. An R-value of 0.359 suggests fundamental problems with the model, but conversations with Harman have reassured us that this R-value is an artifact of the alternate refinement software used for the *S* structure, and it does not indicate a flaw in the deposition of the model at the protein data bank. With Harman's encouragement, we have proceeded to analyze the structure with our computed density.

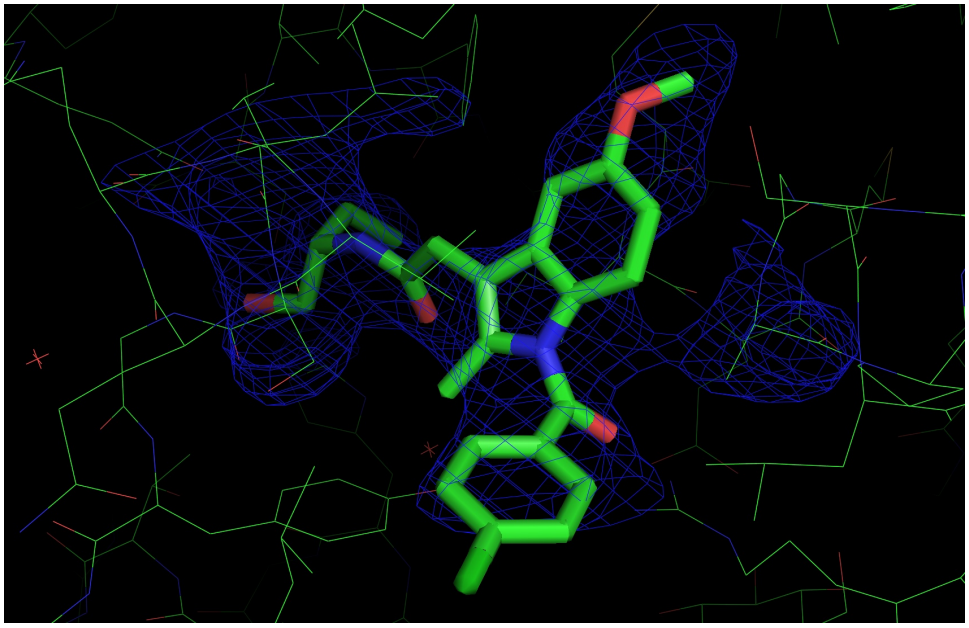

Figure II-10. Omit map difference density contoured at 3σ with a 3 A boundary around the ligand. Density computed using deposited structure factors and atomic coordinates. (2OYE.pdb). At this contour level, as in the Harman paper, there is no density around the chlorine atom, but density clearly extends into the side pocket. Figure courtesy Joel Harp.

As shown in Figure II-10 above (and Figure 2, panel A of Harman et al.), omit map difference density projects quite deeply into the "side pocket" of COX-1. Interestingly, no density is seen around the ligand chlorine atom. Considering ligand

energetics more closely, the *trans* orientation of the *para*-chlorobenzoyl moiety relative to the indole is, from our quantum mechanical calculations in vacuum, 1.0 kcal/mol strained vs the *cis* orientation.

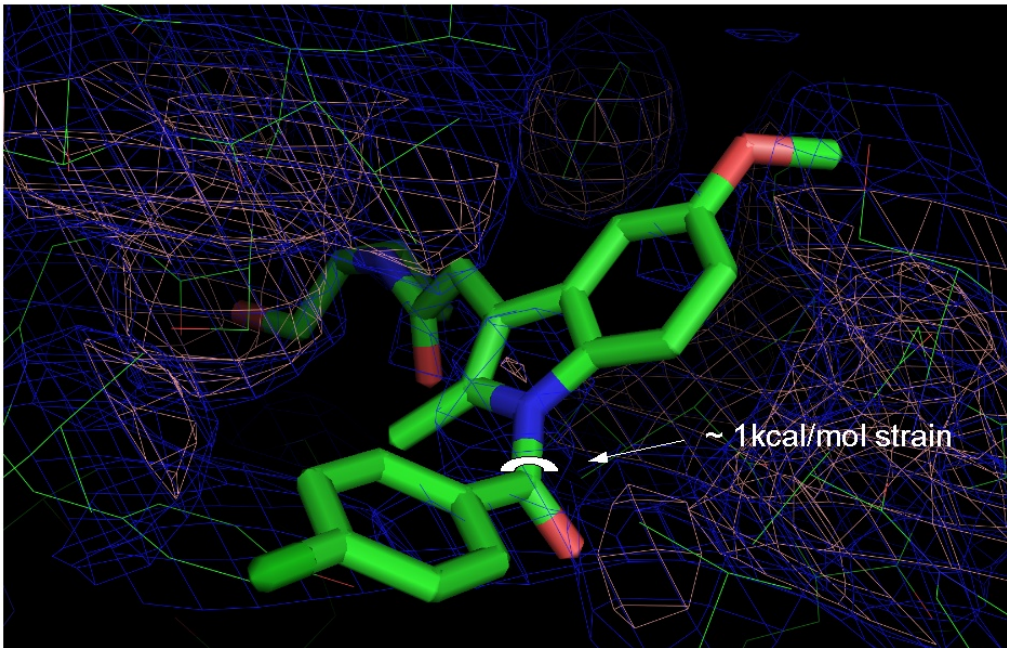

Figure II-11. Omit map difference density contoured at 1σ (blue) and 0.5σ (salmon). The ligand is docked with a the *para*-chlorobenzoyl moiety *trans* to the indole ring. Figure courtesy Joel Harp.

Also energetically surprising is the conformation of the amide substituents in the side pocket of COX-1. The Harman structure depicts a conformation gauche to the amide carbonyl, an orientation that we attributed to less potent binding in our studies.

Conclusions

We have used model building and equilibrium molecular dynamics simulations to propose three-dimensional models for ovine COX-1 with a series of indomethacin ethanolamide derivatives, and to investigate energetic and structural aspects of these complexes. Our modeling studies yield a detailed picture for the various inhibitor complexes that is consistent with available experimental data, and the calculations also provide a plausible explanation for the basis of stereoselective ligand binding for this set of molecules. These calculations confirm that it is possible for COX-1 to bind indomethacin enthanolamide analogs without a significant structural rearrangement or expansion of the binding site region. Results obtained in these modeling studies may be helpful in further defining some key features that govern COX-2 versus COX-1 isozyme inhibitor selectivity, and could be useful in future attempts to design inhibitors with increased isozyme selectivity.

At first glance, the X-ray structure appears to have both confirmed our predicted binding mode for the α-(*R*)-substituted ethanolamides, and fundamentally challenged our energetic arguments for enatioselective inhibition by COX-1 of the α-(*S*)-substituted ethanolamides. However, the X-ray structures do not reveal a clear energetic rationale for the alternate binding orientations. Harman suggests that the *R*-enantiomer cannot make the same ionic interactions with His-90 and Gln-192 without enduring a steric clash with the "roof" of the COX-1 side pocket. But, we note that if the *R* enantiomer were to bind in this pose, the strain of the substituents to the amide carbonyl would be eliminated, and thus, roof interactions aside, the *R* should be the more potent inhibitor. And, if the *R* enantiomer binds in the orientation that we both predicted, then surely the *S* enantiomer

must be able to adopt a similar orientation, with relieved ligand strain, if only as part of an ensemble of active ligand poses.

The X-ray structures do not explain the binding mode of the α-dimethyl indomethacin ethanolamides, which inhibit COX-1 almost as well as the *S*-ethyl enantiomers. Do they bind like *R*, like *S*, or something entirely different still? It is also not clear from the crystal structure how bulkier α-(*S*)-isopropyl and α-(*S*)-phenyl derivatives can fit into the COX-1 side pocket as α-(*S*)-ethyl does. The COX-2 V523I mutant had no impact on α-(*S*)-methyl binding, which is mysterious in light of the side-pocket interactions. Perhaps these ligands do indeed bind entirely differently to COX-2, as we suggested at the outset of our studies. Perhaps ambiguities in the observed density maps have obscured more definitive answers to the enantioselectivity question.

In modeling an (*R*)-ethyl conformer into the side pocket, Harman suggests that the dynamics of inhibitor binding may be a more important factor in stereoselectivity than the final binding conformation, and that protein dynamics involved in ligand entry may be a critical determinant of indomethacin amide binding to COX enzymes. This observation provides an excellent segue to our next chapter, which explores this conjecture in detail.

CHAPTER III

THE L472M MUTATION IN COX-2

Background

The Discovery of L472M

The ester and amide derivatives of indomethacin are potent and selective inhibitors of COX-2. This contrasts sharply with the parent indomethacin acid, which is a 15x more potent inhibitor of COX-1 than COX-2 (Kalgutkar, Marnett et al. 2000). When the Marnett laboratory first discovered that NSAID neutralization leads to COX-2 selectivity, they also reported that mutation of COX-2 active site and lobby residues which are divergent from COX-1 do not significantly alter the selectivity of these NSAID amides. Whereas the COX-2 V523I mutation dramatically reduces the potency of diarylheterocycles (Gierse et al. 1996), no such mutations of COX-2 conferred impotence on the inhibition of this series of compounds (Kalgutkar, Crews et al. 2000; Kalgutkar, Marnett et al. 2000). Interestingly, mutagenesis of constriction site residues Tyr-355 and Glu-524 abolished the inhibitory potency of the NSAID amides. However, these residues are conserved in both COX isoforms and thus while possibly giving clues about how the inhibitors might bind to COX, these mutations cannot account for the COX-2 selectivity of the series.

Nonetheless, the generality of COX-2-selective inhibition by INDO-amides suggests that some fundamental difference in COX-2 vs COX-1 may account for the

behavior of the compound series. To search for such determinants, the Marnett laboratory scanned divergent amino acids within 7 Å of the COX active site in a mCOX-2 background. All the constructed mutants (V89I, I112L, Y115L, S119V, D125P, A151I, S471M, and L472M are depicted in Figure III-1 below) metabolized substrate with similar efficiency to wild-type enzyme.

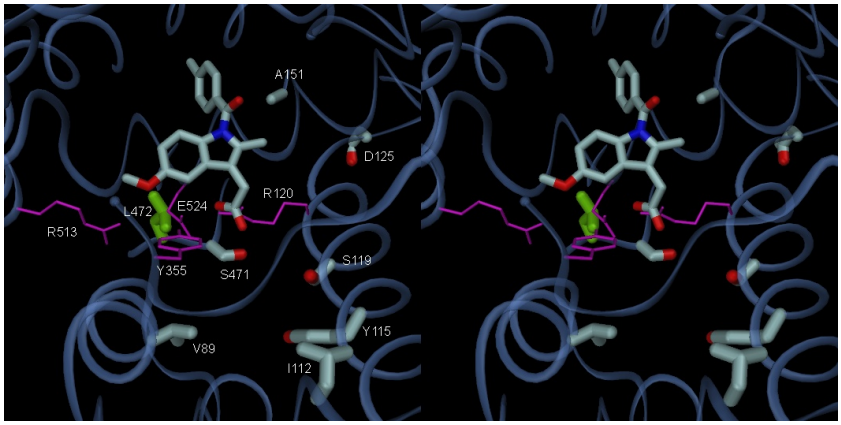

Figure III-1. Location of Mutated Second-Shell Residues Relative to the COX Active Site Model illustrating the location of mutated second shell residues (V89I, I112L, Y115L, S119V, D125P, A151I, S471M, and L472M) using the *4COX* crystal structure. L472 is highlighted in green. INDO and remaining second-shell residues are shown in stick, carbon;gray, oxygen;red, nitrogen;blue, chlorine;magenta. The constriction site residues (Arg-120, Glu-524, and Tyr-355) are shown with wire in magenta.

Surprisingly, the only mutant that showed a significantly attenuated binding was L472M. INDO amides amides were found to associate up to 48x slower to L472M than to mCOX-2. This slower association rate corresponded well with IC_{50} measurements made using the TLC inhibition assay (Table III-1 below).

Mutation of residue L472 in COX-2 alters the selectivity of INDO-amides in a kinetically unique way. In all cases, the neutral INDO derivatives were less potent against L472M. The extent of potency loss (IC_{50}(L472M) / IC_{50}(mCOX-2)) ranged from 3 to 92 (Table III-1).

Table III-1. Potency and selectivity of INDO-amides. (Courtesy Mary Konkle, Marnett lab)

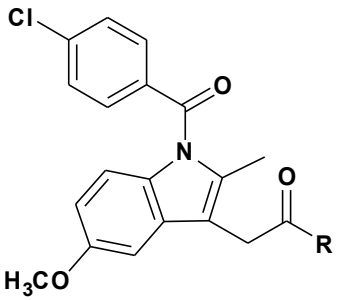

Compound	R	IC50*			IC50 (L472M) / IC50 (COX-2) †
		oCOX-1	mCOX-2	L472M	
1	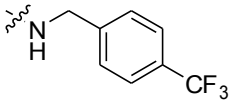	>4000	17	101	5
2	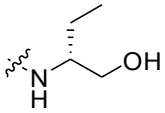	33,000	174	2400	14
3	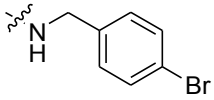	>4000	54	214	4
4	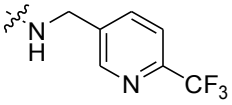	>4000	29	2600	92
5	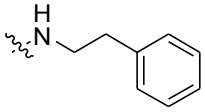	>66,000	60	4400	73
6	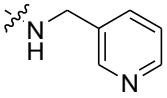	>4000	100	302	3
7	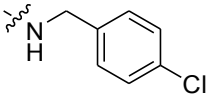	>4000	160	>1000	>6
8	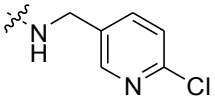	>4000	57	>10000	>175

*IC_{50} data are in nM. †Selectivity index computed as ratio of potencies.

M472L “Reverse” Mutation in COX-1

Though L472M metabolizes arachidonic acid as efficiently as mCOX-2, it could be argued that the mutant is simply deleterious to inhibitor potency, and is not a discriminating component of COX-2/COX-1 selective inhibition. To address this concern, Mary Konkle engineered the complementary mutation of M472L in a COX-1 background, yielding a “reverse mutant.” This COX-1 mutant was subsequently evaluated for its effect on INDO-amide inhibitor potency. Although most neutral NSAID derivatives do not inhibit COX-1, a series of INDO ethanolamides have been reported to exhibit moderate COX-1 inhibitory activity. Thus, (R)-2-(1-(4-chlorophenylcarbonyl)-5-methoxy-2-methyl-1H-indol-3-yl)-N-(1-hydroxybutan-2-yl)ethanamide (2) was chosen as a probe for the impact of the M472L mutation in a COX-1 background. This compound (2) displayed a 14-fold higher potency against the M472L reverse mutant than against hCOX-1 (Figure III-2), underscoring the obervation that residue 472 is a fundamentally important discriminant for COX-1 vs COX-2 inhibition

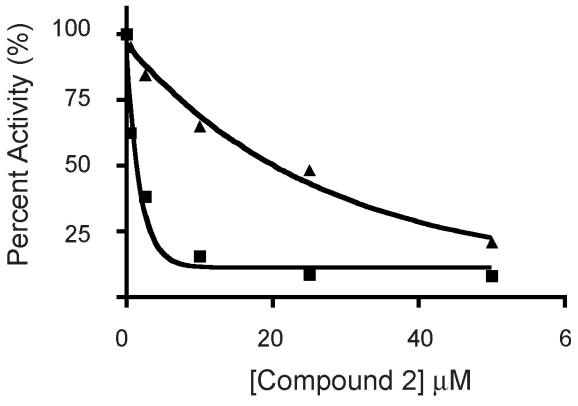

Figure III-2. Potency of Compound 2 against hCOX-1 (IC50 = 20.1μM) and M472L (IC50 = 1.5μM) expressed in HEK293T cells with hCOX-1 (triangles); M472L (squares). Experimental errors are s.e.m. Figure courtesy Mary Konkle, Marnett lab.

Methods

Since there are no suitable unliganded COX-2 crystal structures to generate an initial model, we used structural results from previous MD simulations of a COX-2/indomethacin complex (based on the murine COX-2/indomethacin X-ray structure PDB ID 4COX) (Kurumbail et al. 1996), as reference. We removed indomethacin from the enzyme active site, and also deleted the oligosaccharide residues, since the X-ray structural data for these residues is neither complete nor well characterized. Hydrogen atoms were added to protein residues using the AMBER LEAP module (Case et al. 2006). We then hydrated the empty enzyme active site and generated a solvation shell around the full protein homodimer using the Metropolis Monte Carlo program MMC (http://inka.mssm.edu/~mezei/mmc/) to place SPC/E (Berendsen et al. 1987) water molecules at energetically favorable locations via a cavity-biased (Mezei 1987 & 1989), Grand Canonical ensemble simulation (Marrone et al. 1998). The COX-2 dimer was centered in a rectangular cell 96 Å x 96 Å x 118.5 Å for the GCMC simulations, using the Amber94 potential function (Cornell et al. 1995) and a 7.75 Å solvent-solvent cutoff with minimal-image periodic boundary conditions. Bulk water density was held at 1.0 g/ml in the outer 10 Å shell of the simulation unit cell. Initially, we set the Adams B parameter (Adams 1975), which reflects the excess chemical potential of the simulation, to +1.5, allowing the simulation cell to flood with waters, and the B parameter was reduced subsequently to –1.70 over a series of MC runs. Final water placement was then performed with an equilibrium MC simulation (6×10^7 steps), using every $30{,}000^{th}$ configuration for water placement analysis. Waters outside the first solvation shell were then removed, and 3,000 generic bulk water positions were

calculated using the Mezei and Beveridge algorithm (Mezei and Beveridge 1984) and data from the 2,000 saved ensemble configurations.

The hydrated COX-2 homodimer system was then solvated in a larger truncated octahedral box using the AMBER Leap module, and 10 Na+ counterions were added to impose net neutrality in the periodic unit cell. A weak harmonic restraint (20 kcal/mol/Å) was used to tether the heme prosthetic group securely to the His388 axial ligand during MD simulations. Water and cation positions were relaxed with 1000 steps of conjugate gradient energy minimization, while keeping all protein and heme, atoms fixed. Next, protein and heme atoms were refined with 1000 steps of energy minimization, while water and counterions were held fixed. Finally, the entire system was relaxed with 1000 additional steps of energy minimization. The minimization procedure was followed by 20 ps of low-temperature (20K) constant-volume molecular dynamics, allowing only water, and counterions to move freely. Next, a series of 10 short (0.2 ps) constant-pressure MD simulations were run sequentially, assigning initial velocities for each separate simulation from a unique Boltzmann distribution at 310 K. Then each system was equilibrated for several nanoseconds with NPT ensemble MD simulations.

The mCOX-2 trajectory energies and structural fluctuations stabilized completely after 4.5 ns, and we extracted a configuration snapshot at 4.5 ns to generate the starting configuration for the L472M simulation. We substituted the Met sidechain for L472, based on the Met side chain confirmation observed in COX-1 X-ray structures. PDB IDs 1Q4G (Gupta et al 2004) and 2AYL (Gupta et al. 2006). Hydrogen atoms were added to the M472 side chain using the LEAP module, and the side chain geometry was relaxed using 1,000 cycles of conjugate gradient minimization, with all neighboring side chains

and solvent molecules held fixed. We then equilibrated the M472 mutant system as outlined above. We collected 20 ns of data from both the mutant and mCOX-2 trajectories for subsequent analysis.

We used the AMBER99 (Wang et al 2000) all-atom potential functions for all simulations, with a 1 fs integration time step, a 9 Å real-space nonbonded cutoff and particle-mesh Ewald summation to correct for long-range electrostatic interactions (Darden et al. 1993).

For quasiharmonic analysis of low-frequency dynamics (Levy et al. 1984; Amadei et al. 1993; Ota and Agard 2001; Ferrari et al. 2003), all waters and ions were removed. All side chain hydrogen atoms were stripped from the trajectory files, as high-frequency hydrogen motions were of no interest in these analyses. Quasiharmonic vibrational modes and energies were calculated by the PTRAJ module in AMBER 9 (Case et al. 2006).

Main channel radius analysis was performed with "channel_finder" a PERL script implementation of a protocol that has been described in detail previously (Furse, Pratt, Porter and Lybrand 2006). Basically, "channel_finder" uses a series of iterative MSMS (Sanner et al. 1996) molecular surface calculations to determine the largest probe sphere that can escape from a designated starting point (e.g., the active site cavity) to the surface of the protein. A collection of "blocker" spheres were first manually placed in the COX-2 active site to exclude surface imaging of all but the main channel pathway leading from the active site, past the constriction site network, and into the protein lobby region. For each trajectory snapshot, the initial probe sphere radius is set to 1.0 Å. From there, channel_finder's binary search algorithm will next attempt to surface with a 1.5 Å sphere

if a channel is found, or 0.5 Å otherwise. Subsequent attempts will add or subtract 0.25 Å, 0.12 Å, and finally 0.065 Å from the converging probe sphere radius. While we display frequency counts of all channel radii in our histogram (Figure III-4), we note that water molecules require a main channel radius of at least 0.7 Å to escape the active site. Moreover, with smaller probe spheres, the MSMS algorithm is less reliable and our blocker sphere set may not effectively constrain the probe escape route through the constriction site. Thus, for these narrow channel observations, we simply classify the main channel as closed. The initial MSMS probe spheres were always initially placed adjacent to Ala527 atom Hα in both monomers of both trajectories. Extensive visual inspection of MSMS surfaces from every 50th frame revealed that probe sphere start position was reasonably constrained by the nearby backbone geometry throughout the entire trajectory, so that the probe sphere was indeed surfacing the active site region of interest. While it is quite possible that our selection of start atom and blocking sphere set may have lead to occasional escape through alternate transient channels in the protein, our results are valid as a comparison tool as we precisely duplicate these channel finder parameters in the width calculations for each monomer of each trajectory, for all 19,000 snapshots.

Visualization of MD trajectories and quasiharmonic vibrational modes was performed using MDDISPLAY its companion program NMDISPLAY (Callahan 1996). Static structure visualization was performed with PSSHOW (Swanson 1995).

Structural Analysis of L472M

Inspection of Crystal Structures

Residue 472 is located in a turn that links two alpha helices comprised of residues 463-470 and 478-482. This turn is stabilized by a network of backbone hydrogen bonds that includes, in all COX crystal structures: 471N-468O, 472N-467O, and 470N-466O. Over the residue range 463-482, no pair of COX-2 X-ray structures exhibits a backbone RMSD greater than 0.4 Å and the 4COX structure we used for model construction has a backbone RMSD of 0.36 Å vs. the 2.0 Å COX-1 structures (2AYL and 1Q4G) (Gupta et al. 2004; Gupta et al. 2006). In all COX crystal structures, Leu-472 and Met-472 are packed similarly, with a χ_1 dihedral angle of -60 ± 15°, and χ_2 of 180 ± 25°. Residue 472 is adjacent to the constriction site residue, Glu-524. The invariant backbone and side chain geometry seen in this region of the enzyme allows easy superposition of all COX crystal structures. However, visual and numerical analysis of superimposed COX-1 and COX-2 crystal structures reveals no significant structural differences in the region around residue 472.

Molecular Dynamics Simulation

Since the COX crystal structures do not exhibit any meaningful structural differences near residue 472, we postulated that the L472M mutation in COX-2 might induce a change in the dynamics of the enzyme, and we performed 20 ns molecular dynamics simulations and quasi-harmonic analysis for both wild-type and L472M mutant proteins to explore this possibility. The RMSD for binding site residue backbone atoms

(vs. the 4COX reference crystal structure) is less than 1.3 Å for each monomer in both mCOX-2 and L472M simulations. Typical COX hydrogen-bonding interactions among constriction site residues and transient bridging waters are preserved as seen in the crystal structures. The backbone atom RMSD for residues 463-482, which includes the helices flanking residue 472, is less than 1.0 Å, relative to the 4COX crystal structure. Simple distance analysis shows that the hydrogen bonds that stabilize the turn (residues 471-477 discussed above) are present greater than 90% of the time during the simulations. Leu and Met side chains maintain the same $\chi 1$ and $\chi 2$ torsion angles as seen in crystal structures, varying only ± 30°. Side chain packing analysis shows that residue 472 is well-packed over the entire trajectories for both mCOX-2 and L472M mutant (Gregoret and Cohen 1990).

Quasi-harmonic Analysis

We performed quasi-harmonic analyses of both trajectories to examine more carefully possible changes in local dynamics conferred by the mutant. The lowest frequency quasi-harmonic modes show clearly that L472M strongly impacts local dynamics in the constriction site region, as can be seen in the two movie files deposited with the electronic version of this dissertation. In mutant enzyme, the lowest frequency modes manifest themselves as concerted motions of Glu-524 and Arg-120 side chains. In the mCOX-2 enzyme, these motions are, by comparison, much less strongly coupled. To explore the structural effect these differential motions might have, we used our Channel_Finder utility to conduct a frame-by-frame analysis of the width of the main channel that runs from the lobby region, through the constriction site, and into the active

site21. The results, shown in Figure III-3, demonstrate that the constriction site opens much more widely and frequently in mCOX-2 compared to the L472M protein.

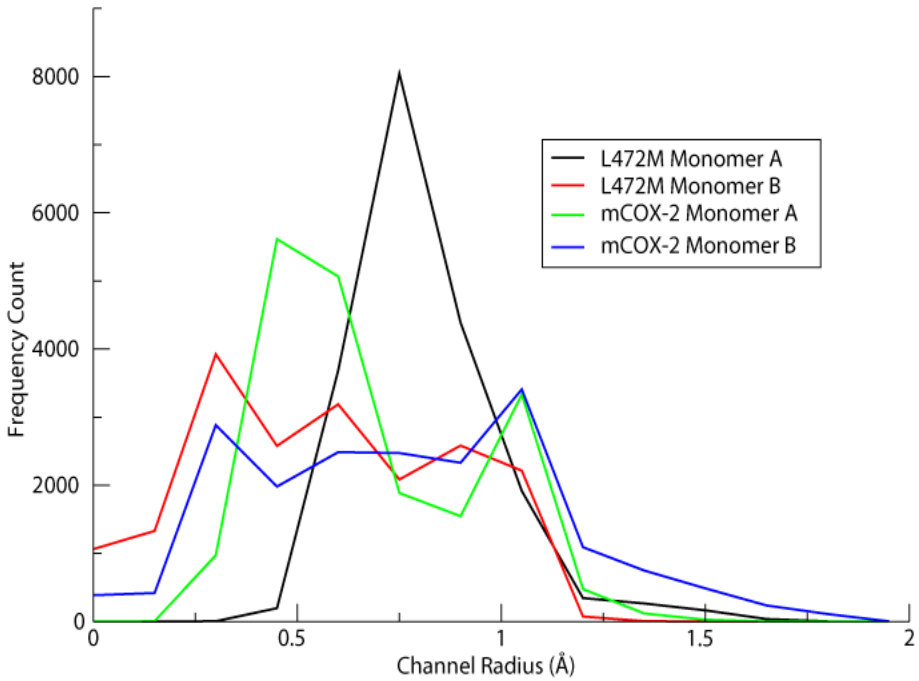

Figure III-3. Main channel radii histograms for the mCOX-2 and L472M mutant MD trajectories. Radii values are computed every picosecond over the final 19 ns of each trajectory. While all radii values are displayed here, the channel is considered closed if the channel radius is smaller than 0.7 Å (the minimum navigable radius for a water molecule).

Thus, these channel width measurements reflect, structurally, the motions observed in the quasi-harmonic analyses. The quasi-harmonic analyses and Channel_Finder results suggest that the L472M substitution alters local dynamics which, in turn, leads to further stabilization of the tightly bound constriction site residues and reduces the frequency of transient constriction site opening.

As noted above, the L472M mutation causes no statistically significant structural displacements in the protein backbone around residue 472 or any nearby residue side chains. Indeed, the local protein geometry, including the residue 472 side chain orientation and packing, is highly conserved throughout both wild-type and mutant simulations, as well as in all published COX-1 and COX-2 crystal structures, and one can therefore easily superimpose all trajectory configurations onto a common backbone reference structure. We then projected the low-frequency vibrational modes computed in the quasi-harmonic analyses onto this common backbone reference structure to examine the structural effects of the altered local dynamics. The L472M substitution decreases the Glu-524 side chain fluctuations anisotropically by 0.2 - 0.3 Å, along an axis that projects from the residue 472 side chain through the Glu-524 side chain to the Arg-120 side chain. The Glu-524 side chain fluctuations in the orthogonal directions are unaltered between mCOX-2 and L472M mutant simulations. This anisotropic reduction in Glu-524 side chain fluctuation effectively reinforces the Glu-524/Arg-120 hydrogen-bonding interaction, by diminishing the normal thermal fluctuation that would lengthen, or even transiently break, the Glu-524/Arg-120 hydrogen bond. The mechanistic explanation for this effect is quite simple: the Met-472 side chain is slightly longer than Leu-472, as seen in Figure III-5, and thus physically reduces the range of motion possible for the Glu-524 side chain along the Met-472/Glu-524/Arg-120 axis described above. The ‘reinforced’ Glu-524/Arg-120 hydrogen bond in turn stabilizes the constriction site network and reduces the constriction site opening frequency and open-state diameter.

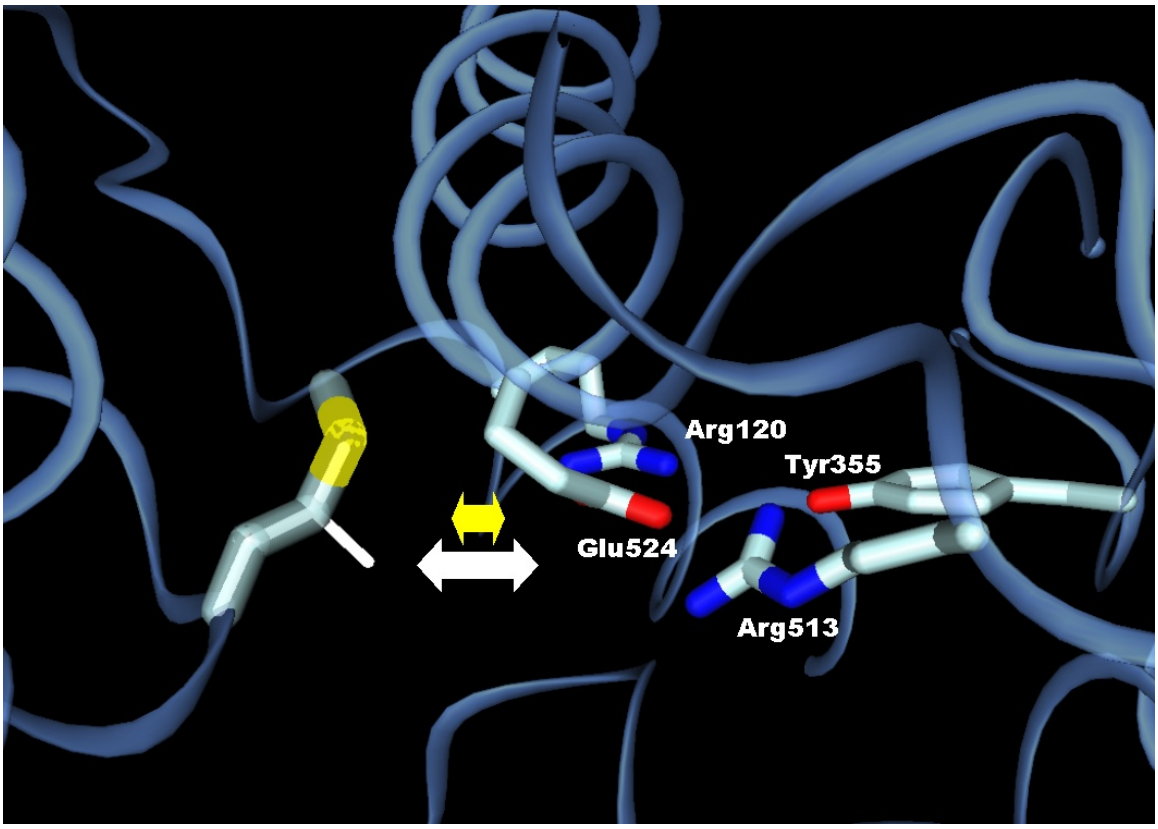

Figure III-4. Leu-472 superimposed on Monomer A from a typical snapshot of the COX-2 Met-472 trajectory. The constriction site residues are labeled. Double-headed arrows display the change in anisotropic fluctuations of Glu-524, relative to the helices flanking position 472. Along this axis, Glu-524 sidechain atoms fluctuate 0.2 to 0.3 Å less (yellow arrow) when adjacent to Met-472 (white), vs. mCOX-2 Leu-472 (white arrow).

Kinetic Analysis of L472M COX-2-Inhibitor Binding and Inhibition

The computational analysis suggests differential constriction site dynamics between wild-type COX-2 and L472M contributes to their differential sensitivity to inhibition by indomethacin amides. To test this hypothesis, the Marnett lab performed steady-state and pre-steady-state kinetic analysis of COX-inhibitor binding. INDO and INDO-esters and amides are slow, tight-binding inhibitors that exhibit a two-step kinetic mechanism for inhibition, as shown in the equation below:

$$E + I \underset{k_{-1}}{\overset{k_1}{\rightleftharpoons}} E - I \underset{k_{-2}}{\overset{k_2}{\rightleftharpoons}} E - I^* \qquad K_I = k_{-1}/k_1$$

Concentration-dependent binding experiments were performed using N-(4-bromobenzyl)-2-(1-(4-chlorophenylcarbonyl)-5-methoxy-2-methyl-1H-indol-3-yl)ethanamide (3) to compare the kinetics of inhibition for mCOX-2 and L472M more closely. The k_{obs} values for L472M were dramatically reduced compared to those from mCOX-2 enzyme, which is consistent with reduced dynamics of inhibitor binding.

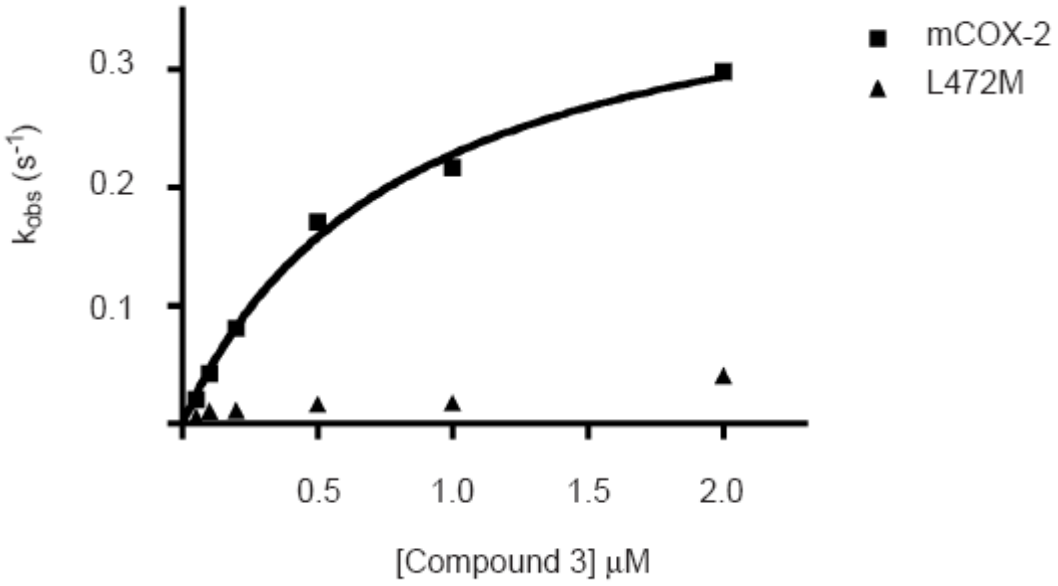

Figure III-5. Concentration dependence of the observed rate of association by Compound 3 with both mCOX-2 and L472M with mCOX-2 (squares); L472M (triangles). Experimental errors are s.e.m. (Figure courtesy Mary Konkle, Marnett Lab)

The K_D values calculated from these data were 0.34 ± 0.04 μM and 1.5 ± 0.09 μM for mCOX-2 and L472M respectively. These values corresponded closely to the K_I's for inhibition by 3 determined by radiochemical analysis (0.32 ± 0.03 μM and 1.8 ± 0.3 μM, respectively).

Mary Konkle conducted pre-steady-state analysis of fluorescence quenching by compound 1 on a stopped-flow instrument to identify the k_1 and k_2 components of k_{obs}. The values of k_1 and k_2 were found to be the same magnitude in the cases of compound 1 binding to both wild-type and mutant enzymes. This is a key difference between 1 and INDO where $k_1 >> k_2$. The plot of k_1 vs. the concentration of compound 1 for each enzyme clearly showed a reduced rate constant for L472M compared to wild-type enzyme (Figure III-6).

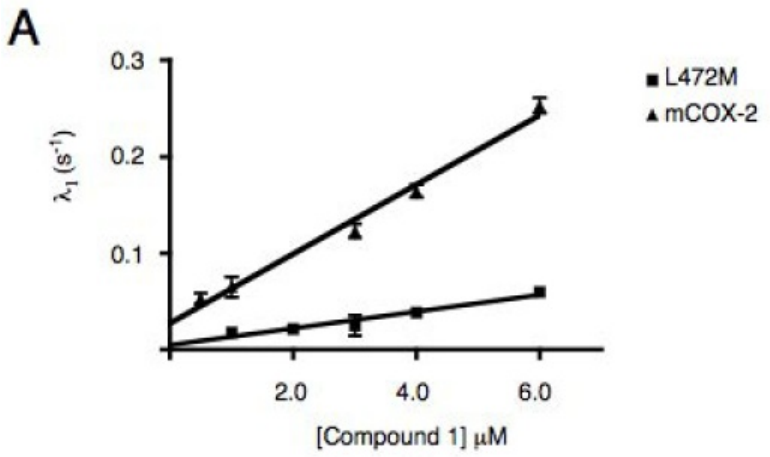

B

	mCOX-2	L472M	mCOX-2/L472M
k_1^*	0.0360 ± 0.002	0.009 ± 0.001	4.00 ± 0.2
$k_{2\pm}$	0.0270 ± 0.008	0.005 ± 0.004	5.40 ± 3.5

Figure III-6. (A) Concentration dependence of k1 for binding of Compound 1 to both mCOX-2 (triangles) and L472M (squares). The slope of the lines are equivalent to k_1. (B) presents the rate constants (k_1 and k_2) for binding of Compound 1 to both mCOX-2 and L472M (* - μM-1s-1); († - s-1). (Figure courtesy Mary Konkle, Marnett Lab)

This is the first report of a COX mutation that slows the initial phase of inhibitor binding as reflected by k_1. Since k_1 is slower than the diffusion-controlled limit, it

reflects both the bimolecular association of inhibitor with enzyme and its movement on the enzyme. In addition to a reduced k_1, k_2 is reduced by approximately the same magnitude as k_1 for L472M.

Discussion

The present study identifies a subtle difference between COX-1 and COX-2 that makes a significant contribution to the sensitivity of COX-2 to inhibition by neutral derivatives of INDO. Conversion of the second-shell Leu residue at position 472 of COX-2 to the Met residue that is present in COX-1 decreases the inhibitory potency of a series of INDO amides relative to wild-type enzyme and decreases their rate of binding to the enzyme. The reverse mutation of Met-472 in COX-1 to Leu increases the sensitivity of COX-1 to inhibition by INDO amide, 2. Although the impact of the L472M mutation in COX-2 is dramatic for some INDO amides, its impact on others is less so, and it is clearly not the sole determinant of the COX-2 selectivity of this class of compounds. Nevertheless, it is the first residue of COX-2 in which a change to a COX-1 residue has any impact on binding and inhibition by INDO amides. This includes a number of conserved first-shell residues that directly contact the inhibitors either in the active site or the lobby beneath it.

Examination of the crystal structures of COX-1 and COX-2 in the region of Leu-472 reveals no detectable differences in backbone configuration or side chain packing. Thus, structural analysis alone is unable to shed light on the mechanism by which this conserved substitution alters inhibitor binding. To probe the origin of this subtle but significant effect, we employed molecular dynamic simulations. Our analyses

suggest that the L472M mutation alters low-frequency dynamical motions in the constriction site region, in a manner that effectively reduces the frequency and magnitude of constriction site opening. We propose that this altered dynamical behavior impedes inhibitor binding to the enzyme.

Kinetic analysis of inhibitor binding to wild-type enzyme and L472M is consistent with the results of the molecular dynamics simulations. The L472M mutation slows the rates of both the first and second steps of inhibitor-COX-2 binding that leads to tight association with the enzyme. This is the first example of a mutation that has an effect on the first step of inhibitor binding, a step believed to represent a combination of the initial binding of the inhibitor to the enzyme and its movement through the constriction that separates the lobby from the active site. This first step is normally much faster than the second step, which yields the final, tightly bound E-I* complex. In the case of INDO, the second step is related to insertion of the 2'-methyl group of the indole ring into the hydrophobic depression in the side of the active site. The fact that the L472M mutant exhibits a significantly reduced initial step of INDO amide binding implies that it has an effect on the movement of the inhibitor into the active site and is consistent with alterations in constriction site dynamics.

Our results are certainly unanticipated in light of the numerous COX crystal structures, which show clearly that either leucine or methionine can be accommodated at position 472 with no effect on equilibrium structure. Substitution of Met for Leu is one of the most conservative observed in protein families, based on Blossum62 and PAM-250 scoring matrices (Gonnet et al. 1992; Henikoff and Henikoff, 1992), and it is rather striking that this conservative substitution could cause a nearly 100-fold decrease in

potency for some of these COX-2 selective inhibitors. However, the possibility that non-local effects, such as a point mutation, can impact ligand binding and/or enzyme function is not unreasonable. Conformational gating due to fluctuating constriction site opening and closing events has been reported previously for enzyme-ligand binding reactions and there are recent reports that point mutations distal to the enzyme active site can have a notable impact on reaction rates, often due to alteration of equilibrium conformational fluctuations that increase the activation free energy barrier (Zhou et al. 1997; Billeter et al. 2001; Rod et al. 2003; Thorpe and Brooks 2004; Wong et al. 2005; Sergi et al. 2006). In light of these previous studies, our computational results and mechanistic hypothesis are quite plausible. The specific details of our mechanistic hypothesis are novel, but it is likely that this type of behavior will be observed in many other gated ligand binding reactions as more enzyme complexes are analyzed.

Previous X-ray studies of COX-inhibitor complexes have not provided full rationalizations for analogous differential binding kinetics. For example, flurbiprofen and methyl-flurbiprofen exhibit drastically different binding kinetics and time-dependence of inhibition. Yet, cocrystals of these inhibitors with COX-1 revealed virtually identical structures (Selinsky et al. 2001). Active-site mutagenesis studies have revealed some functional aspects of COX-2 selective inhibition, but have not previously yielded insights into COX-2 inhibition by INDO-amides. Our work here shows that the synergistic combination of crystallography, functional analysis, and computational techniques is required to tease out critical dynamical details from complicated systems, which currently challenge rational drug design. Other examples of second-shell residues impacting ligand binding are an emerging trend. Our approach should be extensible to

the study of these systems, and should provide a sophisticated strategy with which to address this important, expanding, area of scientific study.

CHAPTER IV

CYCLOOXYGENASE MECHANISTIC INSIGHTS:

Second O_2 Addition and PGG_2 Exit Routes

Introduction

As shown in scheme I-2, the proposed cyclooxygenase reaction mechanism concludes with formation of an allylic radical (at carbons C13, C14, C15), addition of a second molecule of oxygen to the *pro-S* face of C15, reduction of the incipient peroxyl radical, and release of the resulting PGG_2 to the peroxidase site (Rouzer and Marnett 2003). This chapter explores both COX's regio- and stereoselective control of the second O_2 addition, and the PGG_2 exit channels COX may provide so that this unstable molecule can transit to the peroxidase site. Molecular dynamics trajectories, with the allyl radical (PGA) and PGG_2 bound to the active site of both COX isoforms, have been run earlier, and the analyses reported here extend previous computational studies of the first COX oxygenation (Furse, Pratt, Schneider et al. 2006).

Second O_2 Addition

Absent enzymatic (or other) control mechanisms, both faces of C13 and C15 should be equivalently favorable sites for the second oxygenation in PGG_2 synthesis. Yet, the second oxygen molecule is added exclusively to the *pro-S* face of C15. From his X-ray structure of PGG_2 bound in the active site, Kiefer argues that the second oxygen addition is favored at the *pro-S* face of C15 due to steric occlusion of the other three

reaction centers (Kiefer et al. 2000). And, mutagenesis studies by Schneider demonstrate that the COX-2 substitutions V349I, S530T, S530M, and S530V, to varying extents, invert the stereo chemistry of the PGH_2 product from 15*S*- to the bioinactive 15*R*-stereoisomer (Schneider et al. 2002).

To elucidate how COX dynamically controls the first oxygen addition, Furse conducted computational studies and found that cyclooxygenase employs a combination of oxygen channeling and steric shielding to drive the first oxygen addition to the *pro-R* face of C11 (Furse, Pratt, Schneider et al. 2006). In the present work, we are extending Furse's studies to identify dynamic factors that impact the stereochemistry of the second oxygen addition.

PGG_2 Exit Routes

The diffusion of substrates to enzyme active sites, and the release of reaction products are fundamental biochemical processes, necessary for life. While X-ray crystal structures have yielded fascinating insights into the interactions of bound enzyme-substrate and enzyme-inhibitor complexes, these structures have only infrequently revealed the routes by which small molecules transit to active sites. In many cases such as COX, all crystal structures show that the active site is sequestered from the protein exterior. Thus, we *must* conclude that ligand transit is only enabled by thermal fluctuations of the protein. This reasoning was the impetus for early molecular dynamics explorations of oxygen's route to the myoglobin heme, which crystallography reveals to be encased in a well packed, hydrophobic pocket (Case and Karplus 1979). While all-atom simulation of the system was not possible at the time, potential exit routes were

explored using a rigid protein model, and several, low barrier, concerted side chain rotamer combinations were identified as potentially creating paths for O_2 and CO transit. Thus, protein dynamics were implicated in the lowering of energetic barriers to ligand transit.

More recently, an all-atom molecular dynamics simulation of acetylcholinesterase identified a fast, dynamic, molecular gate separating external solvent and the channel that leads to the deeply buried enzyme active site. The gating motion of a valine and glycine residue, in concert with the in-plane sliding motion of a tryptophan side-chain are described as being much like a camera shutter (Gilson et al. 1994). In light of the relatively high turnover of enzymatic hydrolysis, and the catalytic demand for a substrate sequestered from bulk solvent, the "back door" gating model is a compelling picture for quick release of acetate and choline.

Direct comparisons between the dynamics of cyclooxygenase vs. acetylcholinesterase (or myoglobin) are potentially dangerous. COX substrates and products are much larger molecules than acetylcholine. And, the turnover number for COX (~60 molecules per COX dimer per second) (Smith et al. 2000) is at least ~100x slower than that of acetylcholinesterase. However, mounting evidence from combined NMR/MD studies suggests that the ps-ns timescale fluctuations observed in MD simulations are connected to, and required for, the slower, larger scale motions that enable enzyme function (Henzler-Wildman et al. 2007). Thus, while we might not see a dramatic channel opening in a 10 ns COX simulation, we should expect simulations to reveal transient local fluctuations which hint at larger-scale, kinetically relevant, channel fluctuations.

It is reasonably certain that arachidonic acid, following its release from the membrane, arrives at the cyclooxygenase active site by first traveling through the cyclooxygenase lobby, and then passing through the constriction site hydrogen bonding network. However, the departure path of PGG_2 and its route to the peroxidase site is a deeper mystery. Early experiments show that membrane-associated (microsomal) COX-1 preferentially reduces endogenous PGG_2 vs. exogenous radio-labeled PGG_2, whereas purified COX-1 enzyme reduces exogenous PGG_2 just as efficiently (Eling et. al 1991). Eling's observations suggest a role for the membrane in the shuttling of PGG_2 to the peroxidase site and they have provided much fuel for the musings of crystallographers.

Daniel Picot outlines three proposals for the transit of PGG_2 (Picot 1998). First, he postulates that PGG_2 could directly diffuse through the enzyme. But, he discounts this idea as X-ray structures reveal no suitably wide channels in the enzyme. Next, he speculates that the increased hydrophilicity of PGG_2 (vs. arachidonate) would make it unlikely for PGG_2 to return to the membrane for passive release into the luminal space and diffusion to the peroxidase site. Third, he gently promotes the idea that PGG_2 could return to the lobby, and escape through a "small window" from there into the luminal space. Picot also notes that elucidation of the structural determinants of PGG_2 transport could potentially lead to development of a dual cyclooxygenase/peroxidase inhibitor. Thus, our computational research in this area may stimulate more than just academical interest.

Regio- and Stereospecificity of the Second Oxygen Addition

Results

As with Furse's studies of the first oxygen addition, spin localization has the potential to play a role in the specificity of the second oxygen addition. If COX were to twist the allylic radical out of plane, that would localize unpaired spin density at a specific face of C13 or C15, making it a favorable site for oxygenation. Thus, we have reconsidered the possibility of spin localization in the context of the allylic radical. Across both COX-1 and COX-2 PGA trajectories, the allyl radical is planar on average, and the standard deviation from this planarity is less than 9°. This planarity is not surprising, as the quantum mechanical calculations which Furse employed to parameterize the allyl radical exhibited a rotation barrier of at least 16 kcal/mol (Figure IV-1 below).

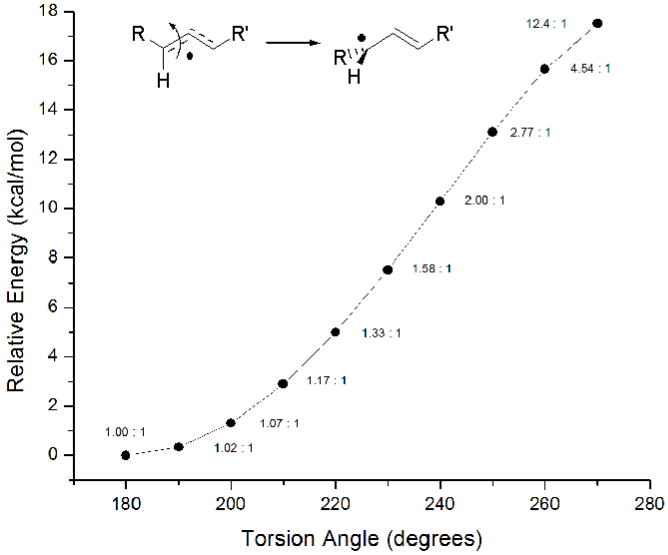

Figure IV-1. 16+ kcal/mol allyl radical rotation barrier calculated with density functional theory at the B3LYP/6-31G* level of theory. Mulliken spin density analysis for the C13-C15 allyl radical intermediate in PGG_2 synthesis is shown at 10° intervals. Figure courtesy Kristina Furse and Derek Pratt.

To explore steric shielding as a possible mechanism, Furse's protocols for measuring the accessibility of the top and bottom faces of C13 and C15 have been extended to consider not only enzyme atoms, but also PGG_2 ligand atoms, as visual inspection of trajectory snapshots suggests that these atoms occlude oxygen access to spin density at C13. The resulting computed accessibility estimates are shown below in Figure IV-2.

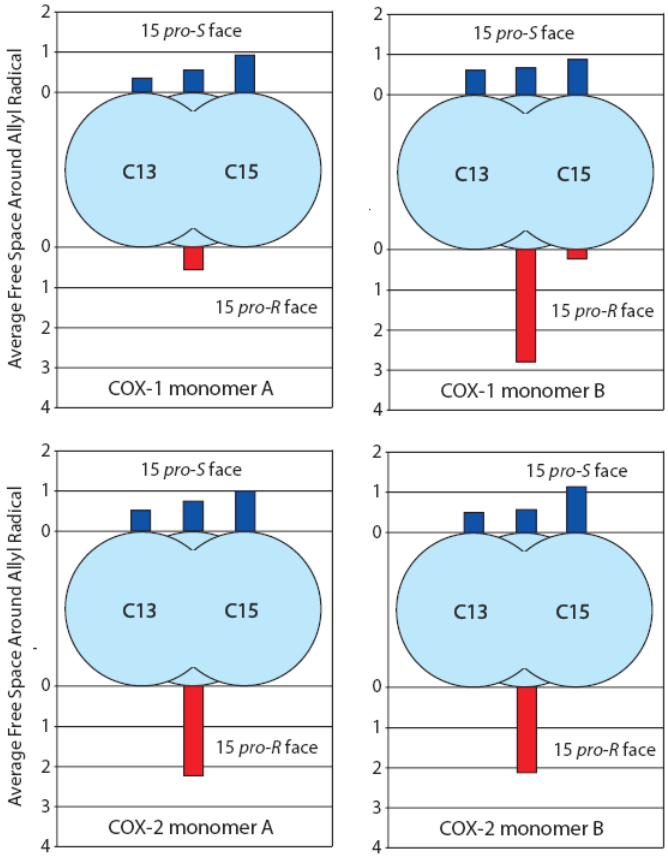

Figure IV-2. Average free space estimates. The amount of empty space along the "top" and "bottom" of the allyl radical carbons (C13-C15) in the COX-1/PGA and COX-2/PGA trajectories is indicated by the height of the bars. The top face (blue bars) is defined as the face exposed to Tyr-385 (*pro-S* face of C15); the bottom face (red bars) is defined as the face exposed to Ser-530 (*pro-R* of C15). The carbon atoms are represented by cyan spheres. The calculations revealed no free space around the bottom face of C13 and C15 (with the neglible exception of COX-1 monomer B). This results from frequent close intermolecular contacts of other PGA atoms with the bottom face of the allyl radical.

The average accessibilities shown in Figure IV-2 directly reflect Kiefer's observations of the static crystal structure – that the *pro*-S face of C15 is the least occluded reaction center of the allyl radical. However, it is noteworthy that the nearest neighbor atoms are somewhat variable in these dynamic trajectories. The bottom of C13 is most often self-occluded by other atoms of the PGA intermediate itself. This self-occlusion is seen in ~65% of all trajectory snapshots. The remaining trajectory frames are primarily occluded by Ser-530. The top face of C13 is more accessible, but Tyr-385 occludes C13 in at least ~65% of each monomer trajectory. An exception to this is COX-1 Monomer B, where Tyr-385 and Trp-387 atoms are closest atom to C13 in ~80% of the snapshots. The bottom of C15 is also primarily occluded by other PGA atoms – in about 50% of the snapshots for each monomer. Ser-530 occludes the bottom face in approximately 25% of the snapshots. In some trajectories, Leu-530 and Leu-534 interact in this area. In others, residues 202-206 play a role in occlusion of the bottom face.

Val-349 has been identified as a critical determinant of C15 oxygenation stereochemistry (Schneider et al. 2002), though it is not packed adjacent to C15 in any crystal structures. This has prompted speculation that the PGA reaction intermediate must be quite unlike arachidonic acid, foreshortening to bring C15 into contact with Val-349 (Schneider et al. 2007). To test this hypothesis, and reveal details of the registration of intermediates in the active site, we measured key inter-atom distances across all our trajectories (between Gly-533 Cα at the top of the channel and C20; Val-349 Cβ and C15; Ser-530 Cβ and C15) and the results of these measurements are in Tables IV-1 – IV-3 below. As can be seen in Table IV-1, there is no indication in our

simulations that the PGA intermediate shifts laterally in the COX binding pocket, suggesting that the "foreshortening" hypothesis is unlikely.

Table IV-1. Distances between Gly-533 Cα at the top of the COX archidonate binding site and C-20.

Bound Species	COX-1 Monomer A	COX-1 Monomer B	COX-2 Monomer A	COX-2 Monomer B
ACD	4.1 (0.3)	4.9 (0.5)	3.9 (0.3)	3.9 (0.3)
RAD	4.1 (0.3)	4.0 (0.3)	4.1 (0.4)	4.0 (0.3)
PGA	4.0 (0.3)	4.0 (0.3)	3.9 (0.3)	4.0 (0.3)
PGG	4.0 (0.3)	4.4 (0.5)	4.0 (0.3)	3.8 (0.3)

Table IV-2. Distances between Ser-530 Cβ and C-15.

Bound Species	COX-1 Monomer A	COX-1 Monomer B	COX-2 Monomer A	COX-2 Monomer B
ACD	4.3 (0.4)	5.2 (0.2)	4.9 (0.4)	5.8 (0.4)
RAD	4.8 (0.3)	5.0 (0.3)	4.3 (0.3)	5.3 (0.4)
PGA	4.3 (0.3)	5.3 (0.3)	4.2 (0.3)	5.2 (0.3)
PGG	4.1 (0.2)	5.1 (0.6)	4.2 (0.4)	5.5 (0.9)

Table IV-3. Distances between Val-349 Cβ and C-15.

Bound Species	COX-1 Monomer A	COX-1 Monomer B	COX-2 Monomer A	COX-2 Monomer B
ACD	7.1 (0.7)	9.5 (0.6)	6.6 (0.6)	6.7 (0.7)
RAD	7.9 (0.6)	7.6 (0.4)	7.2 (0.5)	8.3 (0.7)
PGA	6.1 (0.3)	6.8 (0.4)	6.5 (0.4)	6.9 (0.4)
PGG	7.5 (0.5)	7.4 (1.4)	7.5 (0.5)	6.8 (1.3)

Discussion

Spin localization is a potential oxygen-guiding mechanism which was considered in detail for the regio- and stereoselective addition of the first oxygen (Furse, Pratt, Schneider et al. 2006). In this mechanism, an induced twist in the planar radical drives unpaired spin density to a specific carbon face, biasing it for oxygen addition. While the 16 kcal/mol barrier Furse calculated for a radical rotation is insurmountable at kT, Furse has proposed that smaller deviations from planarity could bias oxygen addition. For example, Mulliken spin density analysis (Figure IV-1) suggests that a 1.33:1.0 relative spin density localization could be achieved with a 40° out-of-plane twist, at a more modest energetic cost of 5 kcal/mol. However, we observe that the trajectories only exhibit planar radicals (with standard deviation under 9°). Since COX does not induce twist in the radical, spin localization is an extremely unlikely mechanism for COX's control of the second oxygen addition.

The extensive space on the bottom face of unnreactive C14 demonstrates that the product profile is highly dependent on a precise registration of the PGA intermediate in the active site. This has lead us to reconsider the hypothesis that PGA must foreshorten to bring C15 into contact with Val-349, a residue which affects the stereochemistry of the second oxygenation (Schneider et al. 2007). Our molecular dynamics trajectories do not support a foreshortening hypothesis. We find that Gly-533 at the top of the active site remains 4.0 Å (+/- 0.3 Å) distant from the C20 atom of not only bound substrate, but also intermediates and product. Val-349 Cβ does approach C15 when PGA is bound, and this could be part of the explanation for V349I's effect on stereochemistry. Nonetheless, Val-349 Cβ is always more than 6.0 Å away from C15. In the PGA trajectories, on

average, Cβ of Ser-530 is ~1.5 Å closer to C15 than Val-349 Cβ. Thus, where differential steric occlusion of C15 may have a role in the stereochemical inversion by Ser-530 mutants, our steric shielding analysis and simple distance measurements suggest that more subtle effects must be responsible for inversion in the case of V349I.

Steric shielding appears the most likely mechanism to dominate the second oxygenation. This is no surprise in light of Kiefer's crystal structure observations. What may be novel is our observation that the atoms in PGG_2 themselves play a major role in steric occlusion of the allyl radical. This observations is consistent with the fact that C13 oxidation has been only detected as an extremely minor, putative, COX reaction product (Hecker et al. 1987). Only 15-hydroxy PG isomers are found among major autoxidation products, and it was previously proposed that this was due to steric occlusion from the cyclopentane ring (Schneider et al. 2007). Our calculations of the free space afforded by nearest neighbor atoms directly supports this proposal in the enzymatic context. More specifically, the relatively strong occlusion of the bottom face of C15 by Ser-530 may indirectly explain the increased production of *15-R* prostaglandins when this residue is mutated to Thr, Met, or Val. Perhaps these mutations induce a register shift of PGA in the enzyme, or generally alter side chain packing in this region. It is tempting to speculate that the failure of these mutants to entirely drive products to the *15-R* stereoisomer results from the significant self-occlusion of the bottom face of PGG_2 at the C15 position. The V349I COX-2 mutant drives 60% of the product profile to 15-*R*. This could be a more subtle effect than the Ser mutations as we find that Val-349 rarely contacts C15 as a nearest neighbor. It would be interesting to test these mutations to see if the MD trajectories suggest interesting mechanisms for the altered oxygenation patterns.

Earlier work by Furse convincingly argues that, in the COX system, the most likely route for oxygen is simply the main channel, which directly links the oxygen-favorable membrane environment to the active site. Short simulations, started with O_2 molecules placed near the *pro-R* face of the arachidonyl radical C11 atom (the site of the first oxygenation) usually resulted in (multiple) quick returns of O_2 to the membrane, via the main channel. However, in one simulation, O_2 stabilized in a position near C15, consistent with the observation of 15*R*-HETE as a minor COX reaction product (Furse, Pratt, Schneider et al. 2006). Though our sample size is to still too small to impart statistical significance, further simulations have shown that ~5% of the time O_2 will migrate to the top face near C15, an intriguing correlation to the ~5% 15*R*-HETE found in the reaction product mix. As we have observed no shift of intermediates during different simulations, this apparently favorable binding site for O_2 could well play a role in guiding the second oxygenation. A comprehensive treatment of this possibility may require additional simulations to monitor oxygen starting from the top, *pro-S*, face of C15. The idea of specific oxygen channeling has also been explored in 12/15-lipoxygenase, where analysis of molecular dynamics trajectories has revealed oxygen channels leading to high-affinity oxygen binding sites (Saam et al. 2007). Perhaps these ideas will have a specific analogue in the form of a COX binding site for O_2 above the C15 atom of bound substrate or intermediates.

PGG_2 Exit Routes in COX

Picot identifies a "long narrow channel that begins at the top of the cyclooxygenase channel and goes toward the dimer interface, running in the vicinity of the peroxidase active site." He does not argue that this channel exists for product transport. Instead, he suggests that, as substrate binds, water might exit through this channel. While early COX structures are devoid of water placement, the first high resolution (2.0 Å) structure of COX-1 (Gupta et al. 2004) sheds additional light on this channel, as a line of well-resolved waters were observed in this area. Moreover, the X-ray density corresponds to a wide range of potential solvent positions, and thus suggests the possibility of water flow through this region.

Naming this channel "D1" in her molecular dynamics studies, Furse further characterized the channel as emanating from the space between Gly-533 and Gly-227. Her simulations found that the width of this channel is quite constant, and narrow (Furse, Pratt, Porter and Lybrand 2006). These observations discount the idea that channel D1 functions in the release of PGG_2, but they are not inconsistent with D1's proposed function in the release of waters. Her paper also introduces channel "D2" and reported that it could interconvert between open and closed states on a nanosecond time scale – with the more open state roughly equivalent to the D1 channel width. Channels D1 and D2 are shown in Furse's graphic cutaway Figure IV-3 below:

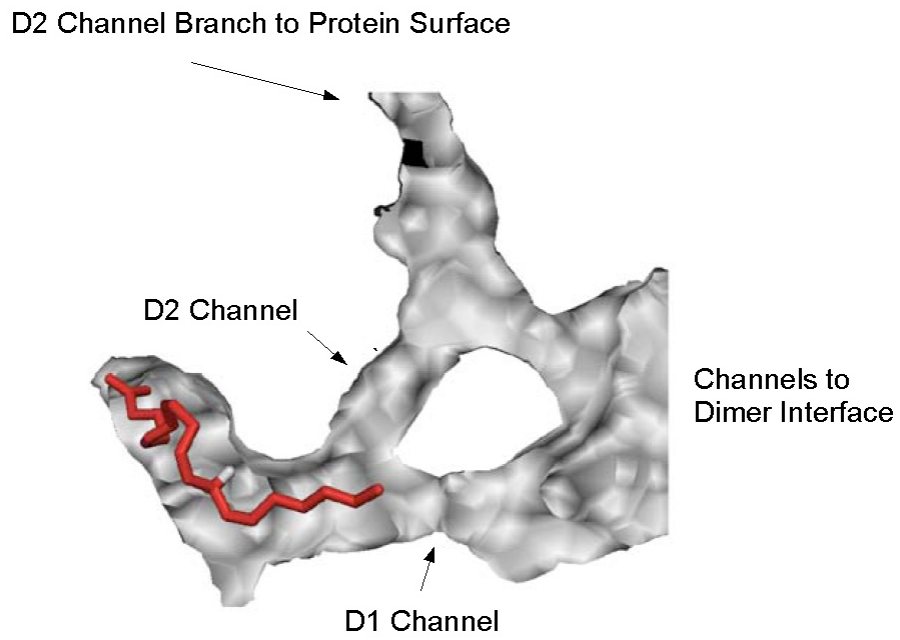

Figure IV-3. Channels D1 and D2 are shown from average structures from equilibrium trajectories of COX-2 monomer A with arachidonate bound. (Courtesy Kristina Furse.)

Another crystallographer's proposal is that PGG_2 might exit through the main channel constriction site, between the dimer membrane binding domains, and then transit through the solvent rich dimer interface (Kiefer et al. 2000). Furse added that the dimer interface is rich with basic residues, and the positive electrostatic potential of the region could facilitate transit of PGG_2.

To further explore enzyme dynamics and channel openings as the cyclooxygenase reaction progresses, Furse and Lybrand conducted additional simulations of COX-1 and COX-2 with both PGG_2 and its precursor allyl radical species (PGA). I have employed the channel_finder utility (methods described in previous chapter) to compare these systems with Furse's earlier COX simulations with bound arachidonate and arachidonyl pentadienyl radical.

Channel_finder Results

A profiling of the D1 channel widths across all trajectories is shown below in Figure IV-4. The histograms in these figures show counts of snapshots exhibiting various D1 channel widths. As a general trend, the D1 channel opens widest when the arachidonyl pentadienyl radical is bound. Though, in COX-1 monomer A, these opening events are more common when the allyl radical species is bound. With PGG_2 bound, the D1 channel radius seen in the trajectory snapshots never exceeds 1.5 Å in COX-1 – whereas the channel radius is routinely 0.25 Å greater for bound PGA/RAD trajectories (monomer A panel) and RAD/PGA trajectories (monomer B panel). In the COX-2 trajectories, channel D1's relative constriction with PGG_2 bound is not as marked as in COX-1. However, larger channel widths are sampled more frequently in the COX-2 RAD trajectories than in the PGA or PGG_2 trajectories.

In short, these channel_finder measurements do not suggest that the D1 channel may be opening wider in response to bound PGG_2 product, and our working interpretation of these data is that the D1 channels are all consistently narrow with bound PGG_2.

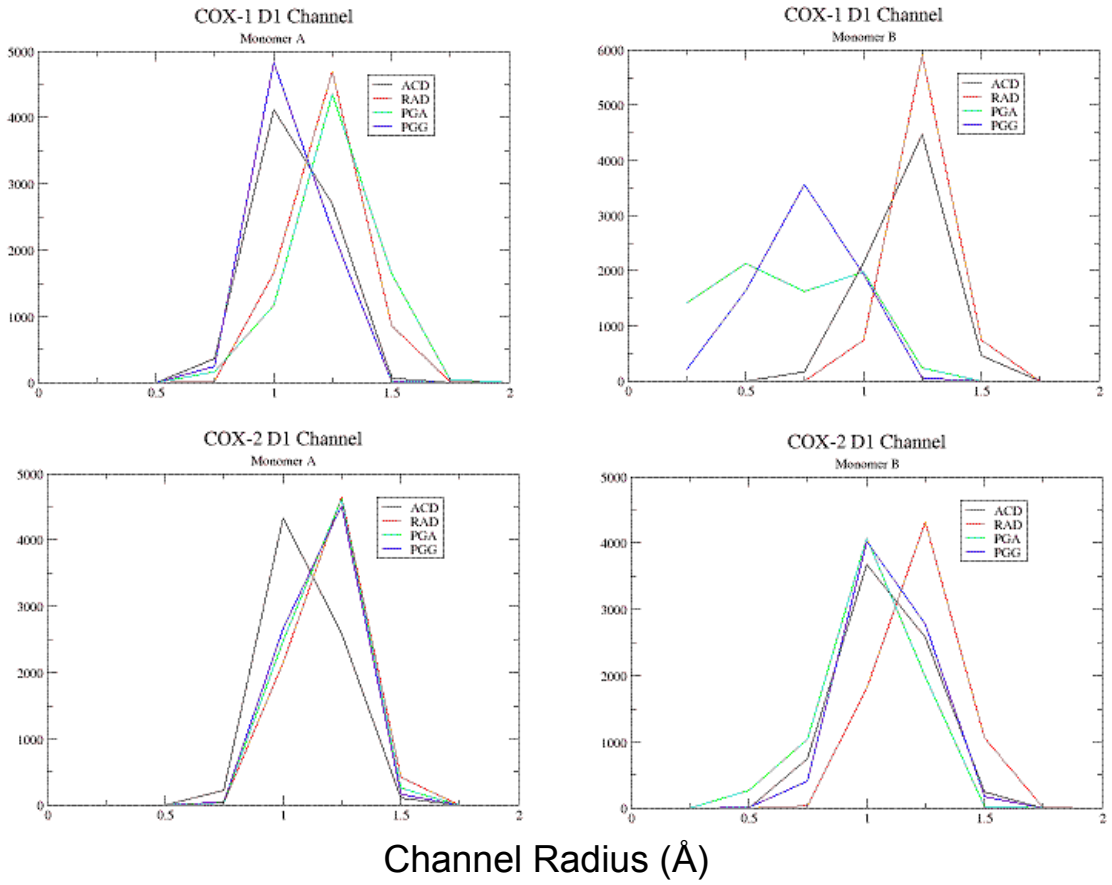

Figure IV-4. Channel radii histograms for the D1 Channel. Measurements were made on each monomer from the equilibrium trajectories of each COX isoform with bound arachidonic acid (ACD), pentadienyl radical (RAD), allyl radical (PGA) and prostaglandin G_2 (PGG).

Channel_finder measurements on channel D2 (Figure IV-5 below) may suggest that D2 could function as a PGG_2 exit route. Monomer A of COX-1 shows a marked opening of the D2 channel when PGG_2 is bound. Across both COX-2 monomers, bound PGG_2 can be associated with the largest D2 channel widths, which routinely exceed 1.5 Å in diameter.

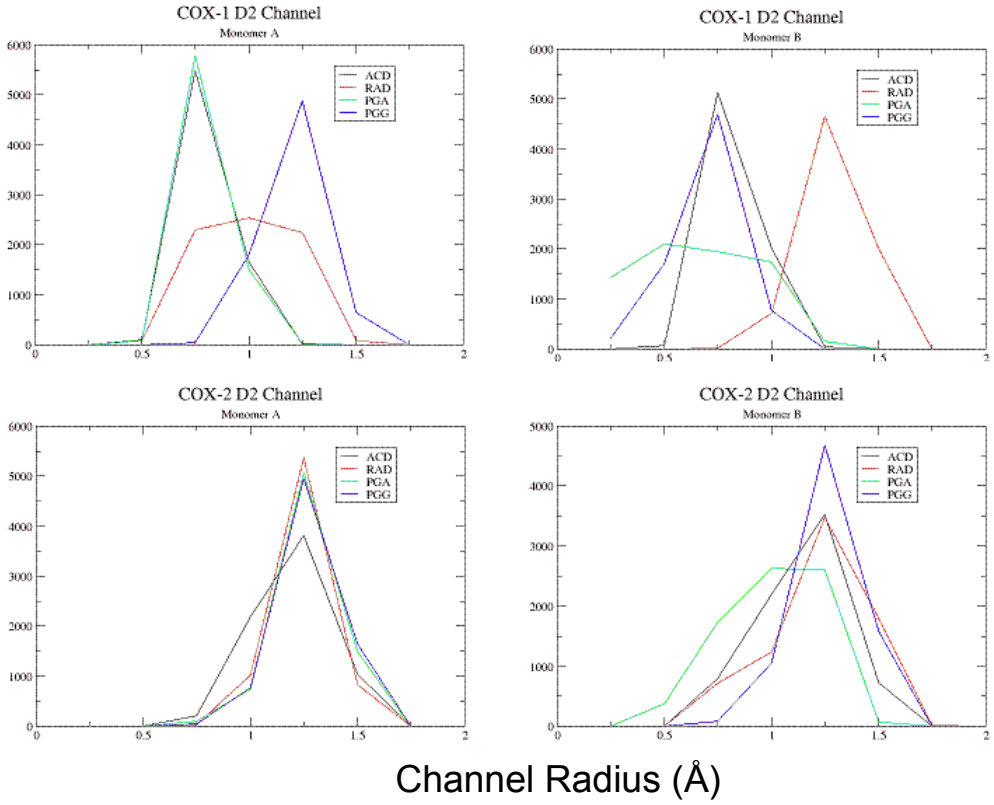

Figure IV-5. Channel radii histograms for the D2 channel. Measurements were made on each monomer from the equilibrium trajectories of each COX isoform with arachidonic acid (ACD), pentadienyl radical (RAD), allyl radical (PGA) and prostaglandin G_2 (PGG) bound.

Discussion

The relative instability of PGG_2 suggests that its transit to the peroxidase site for specific reduction to PGH_2 cannot be random diffusion. Moreover, since dioxygenated PGG_2 is somewhat bulkier and less lipophilic than arachidonic acid, we would be surprised if PGG_2 would transit through the polar constriction site to return to the membrane, diffuse through the membrane to the lumen, and from there diffuse to the peroxidase site without chemical modification. Though increasing catalytic efficiency may be a key goal for protein evolution (Albery and Knowles 1976), and "back door" product release mechanisms have been proposed for other systems (Gilson et al. 1994; Yount et al. 1995), the slow turnover of the COX reaction does not require such a "back door" to realize its kinetics. However, it is arguable that nature has evolved COX with two reaction sites specifically because that is the most efficient structural control for the reaction. And, in this case, the instability of PGG_2 might require a shielded route to the peroxidase site as part of the system. Perhaps a "back door" release mechanism could be nature's most efficient solution to this requirement, allowing PGG_2 from one COX monomer to shuttle to the peroxidase site of the other.

The D1 channel appears relatively closed throughout these simulations, suggesting that it is not a likely PGG_2 exit route. This may echo an important earlier experimental result, where mutagenesis of Gly-533 to bulkier residues reduces COX-2's catalytic efficiency against arachidonate, but shorter C18 fatty acids are oxidized just as well by mutant enzymes (Rowlinson et al. 1999). However, we suspect that extensive conformational shifts are required to release PGG_2, and thus the Gly-533 mutagenesis effect could result entirely from unfavored registration of the arachidonate substrate. If

our suspicion is correct, inference of product release routes from Gly-533 mutations would be an over-interpretation of these experimental results.

Furse identified the D2 channel as emanating from the top of the active site, and splitting into two arms. One arm reaches to the dimer interface. The other reaches to solvent, through the "top" side of the monomer. Our channel_finder results suggest that D2 is a stronger candidate for product release than D1. In our simulations, the D2 channel opens differentially in each monomer. But, this is not inconsistent with our emerging view of cyclooxygenase function, as it was recently shown that likely only one COX monomer is active at a time (Yuan et al. 2006).

More detailed analysis of our simulation data is still required to identify the structural nature of the D2 channel opening (for example whether specific protein side-chain rotamers are implicated in the opening). Once key residues are identified, mutagenesis could be suggested to attempt to alter the dynamics of the channels, and impact catalytic turnover. Visual inspection suggests that side chain reorientation around the C15 hydroperoxide is a possible starting point for the conformational shift that creates the larger D2 channel – but this cannot be supported without additional work, such as correlation matrix analysis for the PGA vs PGG_2 trajectories. Intriguingly, the C540S and C313S mutations are quite distant from the COX-1 active site, but they dramatically reduce the activity of COX-1 (Kennedy et al. 1994). Though these mutations have much less negative impact on COX-2 activity (MirAfzali et al. 2006), it is plausible that the serines might introduce new hydrogen bonds between secondary structural elements, and in doing so restrain the dynamics of channel opening. Perhaps these deleterious mutations could be characterized dynamically in future simulation work.

Many enzymes function as dimers. It has been proposed that dimerization allows enzymes to be both be efficient, and allow complex kinetic responses to changes in substrate concentrations (Maurel and Ricard 2006). Perhaps the symmetry of the COX dimer is simply nature's way of achieving these goals in the most direct manner possible. It is our hope that ongoing research into the mystery of COX product exit might reveal clues into nature's protein design strategies, and shed more light on these evolutionary pressures for dimerization. Though the mystery of PGG_2 exit in COX is veiled from the experimental techniques of structural biology, refinement of computational techniques for rationalizing product exit could, as Picot suggested, unveil novel strategies for inhibitor action or even drug design..

APPENDIX A

NEW AMBER PARAMETERS

α-(*R*) and α-(*S*) methyl indomethacin ethanolamide

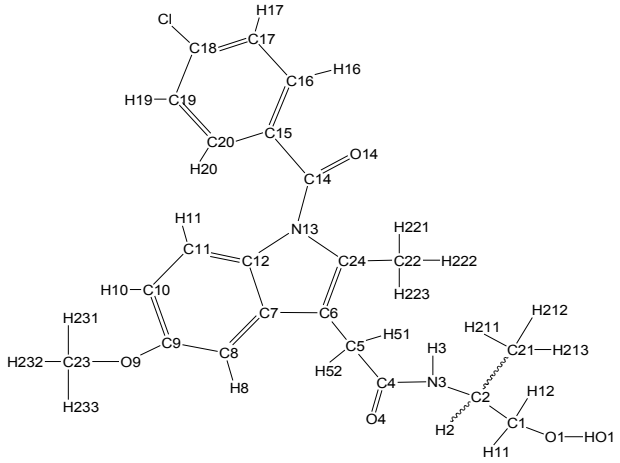

Atom	Atom Type	Charge	Atom	Atom Type	Charge
HO1	HO	0.412	C14	C	0.538
O1	OH	-0.643	O14	O	-0.503
C1	CT	0.127	C15	CA	-0.022
H11	H1	0.058	C16	CA	-0.147
H12	H1	0.058	H16	HA	0.154
C2	CT	0.018	C17	CA	-0.049
H2	H1	0.104	H17	HA	0.132
N3	N	-0.356	C18	CA	-0.026
H3	H	0.282	Cl	Cl	-0.099
C4	C	0.532	C19	CA	-0.049
O4	O	-0.535	H19	HA	0.133
C5	CT	-0.211	C20	CA	-0.147
H51	HC	0.098	H20	HA	0.124
H52	HC	0.098	C21	CT	-0.235
C6	C*	-0.029	H211	HC	0.073
C7	CB	-0.065	H212	HC	0.073
C8	CA	-0.144	H213	HC	0.073
H8	HA	0.155	C22	CT	-0.110
C9	CA	0.126	H221	HC	0.070
O9	OS	-0.357	H222	HC	0.070
C10	CA	-0.158	H223	HC	0.070
H10	HA	0.158	C23	CT	0.013
C11	CA	-0.215	H231	H1	0.072
H111	HA	0.157	H232	H1	0.072
C12	CN	0.038	H233	H1	0.072
N13	NA	-0.011	C24	CW	-0.045

α-(*R*) and α-(*S*) isopropyl indomethacin ethanolamide

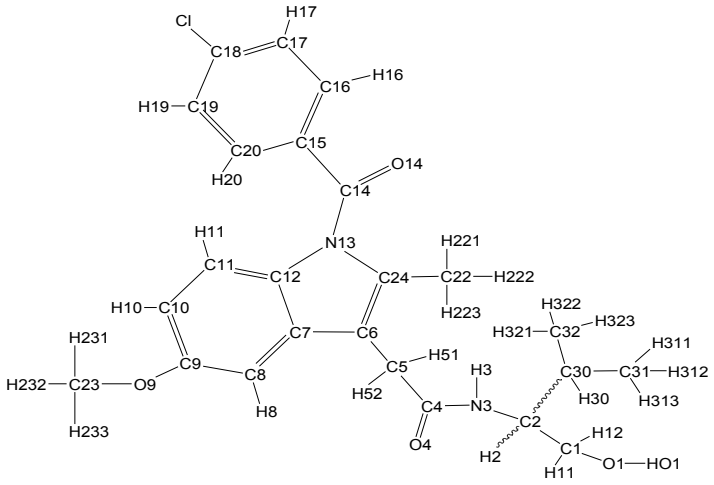

Atom	Atom Type	Charge	Atom	Atom Type	Charge
HO1	HO	0.430	C16	CA	-0.148
O1	OH	-0.635	H16	HA	0.143
C1	CT	0.152	C17	CA	-0.043
H11	H1	0.046	H17	HA	0.132
H12	H1	0.046	C18	CA	-0.029
C2	CT	-0.110	Cl	Cl	-0.096
H2	H1	0.082	C19	CA	-0.043
N3	N	-0.260	H19	HA	0.132
H3	H	0.228	C20	CA	-0.148
C4	C	0.396	H20	HA	0.143
O4	O	-0.530	C22	CT	-0.004
C5	CT	-0.284	H221	HC	0.031
H51	HC	0.158	H222	HC	0.031
H52	HC	0.158	H223	HC	0.031
C6	C*	-0.051	C23	CT	-0.011
C7	CB	-0.080	H231	H1	0.079
C8	CA	-0.119	H232	H1	0.079
H8	HA	0.138	H233	H1	0.079
C9	CA	0.244	C24	CW	0.007
O9	OS	-0.349	C30	CT	0.292
C10	CA	-0.162	H30	HC	0.013
H10	HA	0.127	C31	CT	-0.230
C11	CA	-0.278	H313	HC	0.046
H111	HA	0.204	H311	HC	0.046
C12	CN	0.022	H312	HC	0.046
N13	NA	-0.099	C32	CT	-0.230
C14	C	0.616	H321	HC	0.046
O14	O	-0.504	H322	HC	0.046
C15	CA	-0.067	H323	HC	0.046

α-dimethyl indomethacin ethanolamide

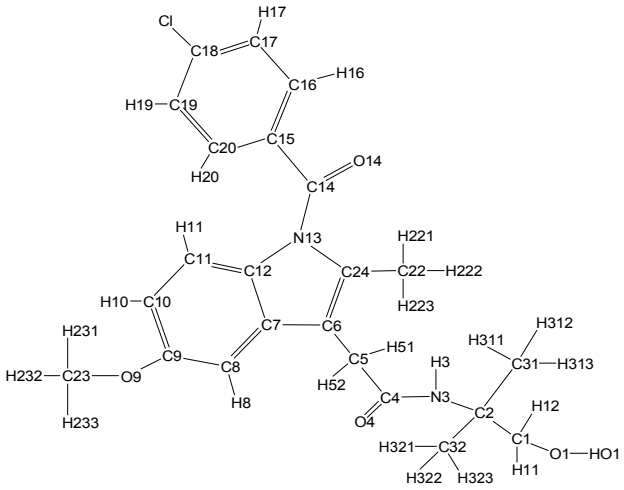

Atom	Atom Type	Charge	Atom	Atom Type	Charge
HO1	HO	0.412	C16	CA	-0.156
O1	OH	-0.628	H16	HA	0.148
C1	CT	0.120	C17	CA	-0.046
H11	H1	0.048	H17	HA	0.134
H12	H1	0.048	C18	CA	-0.032
C2	CT	0.267	Cl	Cl	-0.096
N3	N	-0.439	C19	CA	-0.046
H3	H	0.306	H19	HA	0.134
C4	C	0.522	C20	CA	-0.156
O4	O	-0.571	H20	HA	0.148
C5	CT	-0.074	C22	CT	-0.250
H51	HC	0.065	H221	HC	0.105
H52	HC	0.065	H222	HC	0.105
C6	C*	-0.058	H223	HC	0.105
C7	CB	-0.056	C23	CT	-0.001
C8	CA	-0.169	H231	H1	0.075
H8	HA	0.160	H232	H1	0.075
C9	CA	0.199	H233	H1	0.075
O9	OS	-0.388	C24	CW	-0.019
C10	CA	-0.168	C31	CT	-0.206
H10	HA	0.162	H311	HC	0.056
C11	CA	-0.252	H312	HC	0.056
H111	HA	0.178	H313	HC	0.056
C12	CN	0.026	C32	CT	-0.206
N13	NA	-0.061	H321	HC	0.056
C14	C	0.625	H322	HC	0.056
O14	O	-0.512	H323	HC	0.056
C15	CA	-0.051			

Potential Function Parameters

Section 1. Parameters for Bond Terms

$$E_{bond} = K_r(r - r_0)^2$$

	K_r	r_0
CW-CT	317.8	1.490
CA-OS	431.4	1.380

Section 2. Parameters for Bond Angle Terms

$$E_{angle} = K_\theta(\theta - \theta_0)^2$$

	K_θ	θ_0
C-CT-C*	70.	111.8
C*-CW-CT	70	128.7
CW-CT-HC	50	111.0
CW-NA-C	70	125.8
CT-CW-NA	70	122.8
NA-C –CA	70	124.6
CN-NA-C	70	125.6
CA-CA-OS	70	119.0
CA-OS-CT	60	109.9
O -C –CA	80	118.4

Section 3. Parameters for Torsion Angle Terms

$$E_{tors} = (PK / IDIVF) * (1 + \cos(PN * \varphi - PHASE))$$

	IDIVF	PK	PHASE	PN
C*-CW-CT-HC	1	0.0	0.	3.
NA-CW-CT-HC	1	0.0	0.	3.
X -CA-OS-X	2	1.0	180.	2.

Section 4. Parameters for Improper Torsion Angle Terms

$$E_{tors} = (PK) * (1 + \cos(PN * \varphi - PHASE))$$

	PK	PHASE	PN
NA-CA-CN-CB	1.1	180.	2.
CA-C*-CB-CN	1.1	180.	2.
CW-CN-NA-C	1.1	180.	2.
C -CA-CA-CA	1.1	180.	2.
C*-CT-CW-NA	1.1	180.	2.
CA-OS-CA-CA	1.1	180.	2.
CA-Cl-CA-CA	1.1	180.	2.

REFERENCES

Adams, D.J. (1975) Grand canonical ensemble Monte Carlo for a Lennard-Jones fluid. *Mol. Phys. 29*, 307-311.

Albery, W.J. and Knowles, J.R. (1976) Evolution of Enzyme Function and the Development of Catalytic Efficiency. *Biochemistry 15*, 5631-5460.

Amadei, A., Lissen, A.B.M. and Berendsen, J.C. (1993) Essential dynamics of proteins. *Proteins 17*, 412–425

Andersen, N.H. and Hartzell, C.J. (1984) High Field 1H NMR Studies of Prostaglandin H2 and its Decomposition Pathways. *Biochem. Biophys. Res. Comm. 120*, 512-519.

Bayly, C.I., Cieplak, P., Cornell, W.D. and Kollman P.A. (1993) A well behaved electrostatic potential based method using charge restraints for determining atom-centered charges: The RESP model. *J. Phys. Chem.* 97, 10269-10280.

Berendsen, H.J.C., Grigera, J.R. and Straatsma, T.P. (1987) The Missing Term in Effective Pair Potentials. *J. Phys. Chem. 91*, 6269-6271.

Bhattacharyya, D.K., Lecomte, M., Rieke, C.J., Garavito, R.M. and Smith, W.L. (1996) Involvement of Arginine 120, Glutamate 524 and Tyrosine 355 in the Binding of Arachidonate and 2-Phenylpropionic Acid Inhibitors to the Cyclooxygenase Active Site of Ovine Prostaglandin Endoperoxide H Synthase-1. *J. Biol. Chem. 271*, 2179–2184.

Billeter, S.R., Webb, S.P., Agarwal, P.K., Iordanov, T. and Hammes-Schiffer, S. Hydride Transfer in Liver Alcohol Dehydrogenase: Quantum Dynamics, Kinetic Isotope Effects, and Role of Enzyme Motion. *J. Am. Chem. Soc. 123*, 11262-11272 (2001).

Black, W.C., Bayly, C., Belley, M. Chan, C.-C., Charleson, S., Denis, D., Gauthier, J.Y., Gordon, R. , Guay, D., Kargman, S., Lau, C.K., Leblanc, Y., Mancini, J., Ouellet, M., Percival, D., Roy, P., Skorey, K., Tagari, P., Vickers, P., and Wong, E. (1996) From indomethacin to a selective COX-2 inhibitor: Development of indolalkanoic acids as potent and selective cyclooxygenase-2 inhibitors. *Bioorg. Med. Chem. Lett. 6*, 725-730.

Callahan, T.J., Swanson, E. and Lybrand, T.P. (1996) MD Display: an interactive graphics program for visualization of molecular dynamics trajectories. *J. Mol. Graph. 14*, 39-41.

Case, D.A. and Karplus, M. (1979) Dynamics of ligand binding to heme proteins. *J. Mol. Biol. 132*, 343-368.

Case, D.A., Pearlman, D.A., Caldwell, J.W., Cheatham III T.E., Wang, J., Ross, W.S., Simmerling, C.L., Darden, T.A., Merz, K.M., Stanton, R.V., Cheng, A.L., Vincent, J.J., Crowley, M., Tsui, V., Gohlke, H., Radmer, R.J., Duan, Y., Pitera, J., Massova, I., Seibel, G.L., Singh, U.C., Weiner P.K. and Kollman, P.A. (2002) AMBER 7 University of California, San Francisco.

Case, D.A., Darden, T.A., Cheatham, T.E. , Simmerling, III, C.L., Wang, J., Duke, R.E. Luo, R., Merz, K.M., Pearlman, D.A., Crowley, M., Walker, R.C. Zhang, W., Wang, B., Hayik, S. Roitberg, A., Seabra, G., Wong, K.F., Paesani, F., Wu, X., Brozell, S., Tsui, V., Gohlke, H.,Yang, L., Tan, C.,Mongan, J.,Hornak, V., Cui, G., Beroza, P., Mathews, D.H. Schafmeister, C., Ross, W.S. and P.A. Kollman (2006), AMBER 9, University of California,

Cornell, W.D., Cieplak, P., Bayly, C.I., Gould, I.R., Merz, K.M., Jr., Ferguson, D.M., Spellmeyer, D.C., Fox, T., Caldwell, J.W. and Kollman, P.A. (1995) A second generation force field for the simulation of proteins, nucleic acids and organic molecules. *J. Am. Chem. Soc. 117*, 5179-5197.

Darden, T., York, D. and Pedersen, L. (1993) Particle mesh Ewald: An N-log(N) method for Ewald sums in large systems. *J. Chem. Phys. 98*, 10089-10092.

Dunbrack Jr., R.L. and Karplus, M. (1993) Backbone-dependent Rotamer Library for Proteins: Application to side-chain Prediction. *J. Mol. Biol. 230*, 543-574.

Eling, T.E., Glasgow, W.C., Curtis, J.F., Hubbard, W.C. and Handler, J.A. (1991) Studies on the reduction of endogenously generated prostaglandin G2 by prostaglandin H synthase. *J. Biol. Chem. 266*, 12348-12355.

Feng, L., Sun, W.Q., Xia, Y.Y., Tang, w.W., Chanmugam, P., Soyoola, E., Wilson, C.B. and Hwang, D. (1993) Cloning Two Isoforms of Rat Cyclooxygenase: Differential Regulation of Their Expression. *Arch. Biochem. Biophys. 307*, 361-368.

Ferrari, S., Costi, P.M. and Wade, R.C. (2003) Inhibitor specificity via protein dynamics: Insights from the design of antibacterial agents targeted against thymidylate synthase. *Chem. Biol. 10*, 1183-1193.

FitzGerald, G.A. (2004) Coxibs and Cardiovascular Disease. *N Engl J Med 351*, 1709-1711.

FitzGerald, G.A. (2007) COX-2 in play at the AHA and the FDA. *Trends Pharmacol. Sci. 28*, 303-307.

Fletcher, B.S. , Kujubu, D.A. , Perrin, D.M. and Herschman, H.R. (1992) Structure of the mitogen-inducible TIS10 gene and demonstration that the TIS10-encoded protein is a functional prostaglandin G/H synthase. *J. Biol. Chem. 267*, 4338-4344.

Frisch, M.J., Trucks, G.W., Schlegel, H.B., Scuseria, G.E., Robb, M.A., Cheeseman, J.R., Zakrzewski, V.G., Montgomery, J.A., Jr., Stratmann, R.E., Burant, J.C., Dapprich, S., Millam, J.M., Daniels, A.D., Kudin, K.N., Strain, M.C., Farkas, O., Tomasi, J., Barone, V., Cossi, M., Cammi, R., Mennucci, B., Pomelli, C., Adamo, C., Clifford, S., Ochterski, J., Petersson, G.A., Ayala, P.Y., Cui, Q., Morokuma, K., Malic, D.K., Rabuck, A.D., Raghavachari, K., Foresman, J.B., Cioslowski, J., Ortiz, J.V., Baboul, A.G., Stefanov, B.B., Liu, G., Liashenko, A., Piskorz, P., Komaromi, I., Gomperts, R., Martin, R.L., Fox, D.J., Keith, T., Al-Laham, M.A., Peng, C.Y., Nanayakkara, A., Challacombe, M., Gill, P.M.W., Johnson, B., Chen, W., Wong, M.W., Andres, J.L., Gonzalez, C., Head-Gordon, M., Replogle, E.S. and Pople, J A. (1998) Gaussian98, Gaussian, Inc.: Pittsburgh, PA.

Funk, C.D. (2001) Prostaglandins and Leukotrienes: Advances in Eicosonoid Biology. *Science 294*, 1871-1875.

Furse, K.E., Pratt, D.A., Porter, N.A. and Lybrand, T.P. (2006) Molecular dynamics simulations of arachidonic acid complexes with COX-1 and COX-2: insights into equilibrium behavior. *Biochemistry 45*, 3189-3205.

Furse, K.E., Pratt, D.A., Schneider, C., Brash, A.R., Porter, N.A. and Lybrand, T.P. (2006) Molecular Dynamics Simulations of Arachidonic Acid-Derived Pentadienyl Radical Intermediate Complexes with COX-1 and COX-2: Insights into Oxygenation Regio- and Stereoselectivity. *Biochemistry 45*, 3206-3218.

Gierse, J.K., McDonald, J.J., Hauser, S.D., Rangwala, S.H., Koboldt, C.M. and Seibert, K. (1996) A Single Amino Acid Difference between Cyclooxygenase-1 (COX-1) and -2(COX-2) Reverses the Selectivity of COX-2 Specific Inhibitors. *J. Biol. Chem. 271*, 15810-15814.

Gilson, M.K., Straatsma, T.P., McCammon, J.A., Ripoli, D.R., Faerman, C.H., Axelsen, P.H. Silman, I. and Sussman, J.L. (1994) Open "back door" in a molecular dynamics simulation of acetylcholinesterase. *Science 263*, 1276-1278.

Gonnet, G.H., Cohen, M.A. and Benner, S.A. (1992) Exhaustive matching of the entire protein sequence database. *Science 256*, 1443-1445.

Greig, G.M., Francis, D.A., Falgueyret, J.P., Ouellet, M., Percival, M.D. Roy, P., Bayly, C., Mancini, J.A. and O'Neill, G.P., (1997) The Interaction of Arginine 106 of Human Prostaglandin G/H Synthase-2 with Inhibitors Is Not a Universal Component of Inhibition Mediated by Nonsteroidal Anti-inflammatory Drugs. *Mol. Pharmacol. 52*, 829-838.

Gregoret, L.M. and Cohen, F.E. (1990) Novel method for the rapid evaluation of packing in protein structures. *J. Mol. Biol. 211*, 959-974.

Guo, Q., Wang, L-H., Ruan, K-H. and Kulmacz, R.J. (1996) Role of Val509 in Time-dependent Inhibition of Human Prostaglandin H Synthase-2 Cyclooxygenase Activity by Isoform-selective Agents. *J. Biol. Chem. 271*, 19134-19139.

Gupta, K., Selinsky, B.S., Kaub, C.J., Katz, A.K. and Loll, P.J. (2004) The 2.0 A resolution crystal structure of prostaglandin H2 synthase-1: structural insights into an unusual peroxidase. *J. Mol. Biol. 335*, 503-518.

Gupta, K., Selinsky, B.S. and Loll, P.J. (2006) 2.0 angstroms structure of prostaglandin H2 synthase-1 reconstituted with a manganese porphyrin cofactor. *Acta Crystallogr. 62*, 151-156.

Gupta, R.A. and Dubois, R.N. (2001) Colorectal cancer prevention and treatment by inhibition of cyclooxygenase-2. *Nat. Rev. Cancer 1*, 11-21.

Gupta, R.A., Tejada, L.V., Tong, B.J., Das, S.K., Morrow, J.D., Dey, S.K. and DuBois, R.N. (2003) Cyclooxygenase-1 is Overexpressed and Promotes Angiogenic Growth Factor Production in Ovarian Cancer. *Cancer Res. 63*, 906-911.

Hamberg, M., Samuelsson, B. (1973) Detection and Isolation of an Endoperoxide Intermediate in Prostaglandin Biosynthesis. *Proc. Natl. Acad. Sci. U.S.A. 70*, 899-903.

Harman, C.A., Turman, M.V., Kozak, K.R., Marnett, L.J., Smith, W.L. and Garavito, R.M. (2007) Structural Basis of Enantioselective Inhibition of Cyclooxygenase-1 by *S*-α-Substituted Indomethacin Ethanolamides. *J. Biol. Chem. 282*, 28096-28105.

Hecker, M., Ullrich, V., Fischer, C. and Meese, C.O. (1987) Identification of novel arachidonic acid metabolites. *Eur. J. Biochem. 169*, 113–123.

Henikoff, S. and Henikoff, J.G. (1992) Amino acid substitution matrices from protein blocks. *Proc. Natl. Acad. Sci. U S A 89*, 10915-10919.

Henzler-Wildman, K.A., Lei, M., Thai, V., Kerns, S.J., Karplus, M. and Kern, D. (2007) A hierarchy of timescales in protein dynamics is linked to enzyme catalysis. *Nature 450*, 913-916.

Kalgutkar, A.S., Crews, B.C., Rowlinson, S.W., Marnett, A.B., Kozak, K.R., Remmel, R.P. and Marnett, L.J. (2000) Biochemically based design of cyclooxygenase-2 (COX-2) inhibitors: facile conversion of nonsteroidal antiinflammatory drugs to potent and highly selective COX-2 inhibitors. *Proc. Natl. Acad. Sci. U.S.A. 97*, 925-930.

Kalgutkar, A.S., Marnett, A.B., Crews, B.C., Remmel, R.P. and Marnett, L.J. (2000) Ester and Amide Derivatives of the Nonsteroidal Antiinflammatory Drug, Indomethacin, as Selective Cyclooxygenase-2 Inhibitors, *J. Med. Chem. 43,* 2860-2870.

Kennedy, T.A., Smith C.J. and Marnett, L.J. (1994) Investigation of the role of cysteines in catalysis by prostaglandin endoperoxide synthase. *J. Biol. Chem. 269*, 27357-27364.

Kiefer, J.R., Pawlitz, J.L., Moreland, K.T., Stegeman, R.A., Hood, W.F., Gierse, J.K., Stevens, A.M., Goodwin, D.C., Rowlinson, S.W., Marnett, L.J., Stallings, W.C. and Kurumbail, R.G. (2000) Structural insights into the stereochemistry of the cyclooxygenase reaction, *Nature 405*, 97-101.

Kozak, K.R., Prusakiewicz, J.J., Rowlinson, S.W. and Marnett, L.J. (2002) Enantiospecific, Selective Cyclooxygenase-2 Inhibitors, *Bioorg. Med. Chem. Lett. 12*, 1315-1318.

Kurumbail, R.G., Stevens, A.M., Gierse, J.K., McDonald, J.J., Stegeman, R.A., Pak, J.Y., Gildehaus, D., Miyashiro, J.M., Penning, T.D., Seibert, K., Isakson, P.C. and Stallings, W.C. (1996) Structural basis for selective inhibition of cyclooxygenase-2 by anti-inflammatory agents. *Nature 384*, 644-648.

Kurumbail, R.G., Stevens, A.M., Gierse, J.K., McDonald, J.J., Stegeman, R.A., Pak, J.Y., Gildehaus, D., Miyashiro, J.M., Penning, T.D., Seibert, K., Isakson, P.C. and Stallings, W.C. (1997) Correction. *Nature 385*, 555..

Levy, R.M., Srinivasan, A.R., Olson, W.K. and McCammon, J.A. (1984) Quasi-harmonic method for studying very low frequency modes in proteins. *Biopolymers 23*, 1099-1112.

Luong, C., Miller, A., Barnett, J., Chow, J., Ramesha, C. and Browner, M.F. (1996) Flexibility of the NSAID binding site in the structure of human cyclooxygenase-2. *Nat. Struct. Bio. 3*, 927-933.

Malkowski, M.G., Ginell, S.L., Smith, W.L. and Garavito, R.M. (2000) The Productive Conformation of Arachidonic Acid Bound to Prostaglandin Synthase. *Science 289*, 1933-1937.

Marrone, T.J., Resat, H., Hodge, C.N., Chang, C.H. and McCammon, J.A. (1998) Solvation studies of DMP323 and A76928 bound to HIV protease: Analysis of water sites using grand canonical Monte Carlo simulations. *Protein Sci. 7*, 573-579.

Massova, I. and Kollman, P.A. (2000) Combined Molecular Mechanical and Continuum Solvent Approach (MM-PBSA/GBSA) to predict ligand binding. *Persp. Drug Disc. Des. 18*, 113-135.

Marnett, L.J. and Maddipati, K.R. (1991) in *Peroxidases in Chemistry and Biology* (Everse, J., Everse, K.E. and Grisham, M.B., eds , CRC Press, Boca Raton, FL) *1*, 293-334.

Maurel, M.-C. and Ricard, J. (2006) The evolution of catalytic function. *Physics of Life Reviews 3*, 56-64.

Mezei, M. (1987) Grand-canonical ensemble Monte Carlo study of dense liquid (Lennard-Jones, soft spheres and water). Mol. Phys. 61, 565-582.

Mezei, M. (1989) Erratum. Mol. Phys. 67, 1207-1208

Mezei, M. and Beveridge, D.L. (1984) Generic solvent sites in a crystal. *J. Comput. Chem. 5*, 523-527.

MirAfzali, Z., Leipprandt, Jeffrey R., McCracken, J.L. and DeWitt, D.L. (2006) Topography of the Prostaglandin Endoperoxide H2 Synthase-2 in Membranes. *J. Biol. Chem. 281*, 28354-28364.

Miyamoto, S. and Kollman, P.A. (1993) What determines the strength of noncovalent association of ligands to proteins in aqueous solution? *Proc. Natl. Acad. Sci. USA 90*, 8402-8406.

Mukherjee, D., Nissen, S.E. and Topol, E.J. Risk of Cardiovascular Events Associated With Selective COX-2 Inhibitors (2001) *JAMA. 286*, 954-959.

Moth, C.W., Prusakiewicz, J.J., Marnett, L.J. and Lybrand, T.P. (2005) Stereoselective binding of indomethacin ethanolamide derivatives to cyclooxygenase-1 *J. Med. Chem. 48*, 3613-3620.

Ota, N.Y. and Agard, D.A. (2001) Enzyme specificity under dynamic control II: Principal component analysis of α-lytic protease using global and local solvent boundary conditions. *Protein Sci. 10*, 1403-1414.

Park, H., Lee, S. (2005) Free energy perturbation approach to the critical assessment of selective cyclooxygenase-2 inhibitors. *J. Comput. Aided Mol. Des. 19*, 17-31.

Philippsen, A. (2003) DINO: Visualizing Structural Biology (http://www.dino3d.org).

Picot, D., Loll, P.J. and Garavito, R.M. (1994) The X-ray crystal structure of the membrane protein prostaglandin H2 synthase-1. *Nature 367*, 243–249.

Picot, D. (1998) The Three-Dimensional Structure of Cyclooxygenases. *Lung Biol. Health Dis. 114* (Eicosanoids, Aspirin and Asthma),161-186.

Plount Price, M.L. and Jorgensen, W.L. (2000) Analysis of Binding Affinities for Celecoxib Analogues with COX-1 and COX-2 from Combined Docking and Monte Carlo Simulations and Insight into the COX-2/COX-1 Selectivity. *J. Am. Chem. Soc. 122*, 9455-9466.

Porter, N.A.(1986) Mechanisms for the autoxidation of polyunsaturated lipids. *Acc. Chem. Res. 19*, 262-268.

Porter, N.A, Weber, B.A., Weenen, H. and Khan, J.A. (1980) Autoxidation of Polyunsaturated Lipids. Factors Controlling the Stereochemistry of Product Hydroperoxides. *J. Am. Chem. Soc. 102*, 5597-5601.

Raz, A., Wyche, A., Siegel, N. and Needleman, P. (1988) Regulation of fibroblast cyclooxygenase synthesis by interleukin-1. *J. Biol. Chem. 263*, 3022-3028.

Rieke, C.J., Mulichak, A.M., Garavito, R.M. and Smith, W.L. (1999) The Role of Arginine 120 of Human Prostaglandin Endoperoxide H Synthase-2 in the Interaction with Fatty Acid Substrates and Inhibitors. *J. Biol. Chem. 274*, 17109-17114.

Rod, T.H., Radkiewicz, J.L. and Brooks, C.L., III. (2003) Correlated motion and the effect of distal mutations in dihydrofolate reductase. *Proc. Natl. Acad. Sci. U S A 100*, 6980-6985.

Rouzer, C.A. and Marnett, L.J. (2003) Mechanism of Free Radical Oxygenation of Polyunsaturated Fatty Acids by Cyclooxygenases. *Chem. Rev. 103*, 2239-2304.

Rowlinson, S.W., Crews, B.C., Lanzo, C.A. and Marnett, L.J. (1999) The binding of arachidonic acid in the cyclooxygenase active site of mouse prostaglandin endoperoxide synthase-2 (COX-2). A putative L-shaped binding conformation utilizing the top channel region. *J Biol Chem. 274,* 23305-23310.

Rowlinson, S.W., Kiefer, J. R, Prusakiewicz, J.J., Pawlitz, J.L.., Kozak, K.R., Kalgutkar, A.S., Stallings, W.C., Kurumbail, R.G. and Marnett, L.J. (2003) A Novel Mechanism of Cyclooxygenase-2 Inhibition Involving Interactions with Ser-530 and Tyr-385. *J. Biol. Chem 278*, 45763–45769.

Saam, J., Ivanov, I., Walther, M., Holzhütter, H.-G. and Kuhn, H. (2007) Molecular dioxygen enters the active site of 12/15-lipoxygenase via dynamic oxygen access channel. *Proc. Natl. Acad. Sci. U.S.A. 104*, 13319-13324.

Sanner, M.F., Olson, A.J., Spehner, J.C. (1996) Reduced surface: An efficient way to compute molecular surfaces. *Biopolymers 38*, 305-320.

Samuelsson, B. (1965) On the Incorporation of Oxygen in the Conversion of 8,11,14-Eicosatrienoic Acid to Prostaglandin E1. *J. Am. Chem. Soc. 87*, 3011-3013.

Schneider, C., Boeglin, W.E., Prusakiewicz, J.J., Rowlinson, S.W., Marnett, L.J., Samel, N. and Brash, A.R. (2002). Control of prostaglandin stereochemistry at the 15-carbon by cyclooxygenases-1 and 2. A critical role for serine 530 and valine 349. *J. Biol. Chem. 277*, 478–485.

Schneider, C., Boeglin, W.E. and Brash, A.R. (2004) Identification of Two Cyclooxygenase Active Site Residues, Leucine 384 and Glycine 526, That Control Carbon Ring Cyclization in Prostaglandin Biosynthesis. *J. Biol. Chem. 279*, 4404-4414.

Schneider, C., Pratt, D.A., Porter, N.A. and Brash, A.R. (2007) Control of Oxygenation in Lipoxygenase and Cyclooxygenase Catalysis. *Chemistry & Biology 14*, 473-488.

Seibert, K., Zhang, Y., Leahy, K., Hauser, S., Masferrer, J., Perkins, W., Lee, L. and Isakson, P. (1994) Pharmacological and Biochemical Demonstration of the Role of Cyclooxygenase 2 in Inflammation and Pain *Proc. Natl. Acad. Sci. U. S. A. 91*, 12013–12017.

Selinsky, B.S., Gupta, K., Sharkey, C.T. and Loll, P.J. (2001) Structural Analysis of NSAID Binding by Prostaglandin H2 Synthase: Time-Dependent and Time-Independent Inhibitors Elicit Identical Enzyme Conformations. *Biochemistry 40*, 5172 – 5180.

Sergi, A., Watney, J.B., Wong, K.F. & Hammes-Schiffer, S. (2006) Freezing a single distal motion in dihydrofolate reductase. *J. Phys. Chem. 110*, 2435-2441.

Smith, W.L., Garavito, R.M., and DeWitt, D.L. (1996) Minireview: Prostaglandin Endoperoxide H Synthases (Cyclooxygenases)-1 and -2. *JBC 271*, 33157–33160.

Smith, W.L., DeWitt, D.L. and Garavito, M. (2000) Cyclooxygenases: Structural, Cellular and Molecular Biology. *Annu. Rev. Biochem. 69*, 146-182.

Swanson, E. (1995) PSSHOW Version 2.4. *Seattle WA*.

Thorpe, I.F. and Brooks, C.L., 3rd. (2004) The coupling of structural fluctuations to hydride transfer in dihydrofolate reductase. *Proteins 57*, 444-457.

Vane, J.R. (1971) Inhibition of prostaglandin synthesis as a mechanism of action for aspirin-like drugs. *Nature - New Biol. 231,* 232-235.

Wang, J., Cieplak, P. and Kollman, P.A. (2000) How well does a restrained electrostatic potential (RESP) model perform in calculating conformational energies of organic and biological molecules? *J. Comput. Chem. 21*, 1049-1074.

Weber, A., Casini, A., Heine, A., Kuhn, D., Supuran, C.T., Scozzafava, A. and Klebe, G. (2004) Unexpected Nanomolar Inhibition of Carbonic Anhydrase by COX-2-Selective Celecoxib: New Pharmacological Opportunities Due to Related Binding Site Recognition. *J. Med. Chem. 47*, 550-557.

Whiteley, P.J., and Needleman, P. (1984) Mechanism of Enhanced Fibroblast Arachidonic Acid Metabolism by Mononuclear Cell Factor. *J. Clin. Invest. 74*, 2249-2253.

Wong, E., Bayly, C., Waterman, H.L., Riendeau, D. and Mancini, J.A. (1997) Conversion of Prostaglandin G/H Synthase-1 into an Enzyme Sensitive to PGHS-2-selective Inhibitors by a Double His513->Arg and Ile523->Val Mutation. *J. Biol. Chem. 272*, 9280-9286.

Wong, K.F., Selzer, T., Benkovic, S.J. & Hammes-Schiffer, S. (2005) Impact of distal mutations on the network of coupled motions correlated to hydride transfer in dihydrofolate reductase. *Proc. Natl. Acad. Sci. U S A 102*, 6807-6812.

Xie, W., Chipman, J.G., Robertson, D.L., Erikson, R.L. and Simmons, D.L. (1991) Expression of a Mitogen-Responsive Gene Encoding Prostaglandin Synthase is Regulated by mRNA Splicing. *Proc Natl. Acad. Sci. U.S.A. 88*, 2692-2696.

Yount, R.G., Lawson, D. and Rayment, I. (1995) Is Myosin a "Back Door" Enzyme? *Biophys J. 68*, 44s-49s.

Yuan, C., Rieke, C.J., Rimon, G., Wingerd, B.A. and Smith, W.L. (2006) Partnering between monomers of cyclooxygenase-2 homodimers. *Proc Natl Acad Sci U.S.A. 103*, 6142-6147.

Zhou, H.-X., Wong, K.-Y. & Vijayakumar, M. (1997) Design of fast enzymes by optimizing interaction potential in active site. *Proc. Natl. Acad. Sci. U S A 94*, 12372-12377.